THE INELASTIC SCATTERING OF ELECTRONS FROM CARBON-12

A

THESIS

Submitted to

THE FACULTY OF GRADUATE STUDIES

in Partial Fulfilment of the Requirements

for the Degree of

DOCTOR OF PHILOSOPHY

in

THE DEPARTMENT OF PHYSICS

UNIVERSITY OF SASKATCHEWAN

by

George Atherley Beer

Saskatoon, Saskatchewan

November 1966

THE INELASTIC SCATTERING OF ELECTRONS FROM CARBON - 12

George Atherley Beer

In this thesis we present measured values of the nuclear matrix element for the 19.4 MeV level in ^{12}C and describe the experimental equipment which was used for this investigation of nuclear structure by the technique of electron scattering.

Previous electron scattering measurements on this level have been made at momentum transfers less than 120 MeV/c and greater than 270 MeV/c. We have measured the matrix element for this level in the previously uninvestigated region of momentum transfers between 120 MeV/c and 220 MeV/c. All present measurements were made at the largest attainable scattering angle to enhance the transverse terms in the cross section.

The experimental matrix elements have been compared with theoretical results both for a 1^- and for a 2^- level predicted to lie in this energy region. These theoretical particle-hole calculations show that in the region of intermediate momentum transfers which we have investigated, the magnitude of the matrix element is most sensative to the spin-parity assignment. The 1^- matrix element has a minimum in this region whereas the 2^- matrix element has a maximum.

The measured matrix elements are in satisfactory agreement with the particle-hole calculations for a 2^- level in ^{12}C and the present values favourably compare with other measurements in the region of overlap.

ACKNOWLEDGMENTS

The ^{12}C measurements have been co-ordinated and supervised by Dr. Henry Caplan. His encouragement and enthusiasm during this phase of the work are sincerely acknowledged as is his invaluable assistance in the preparation of the final draft of this thesis.

Work culminating in the beam handling system was carried on under the direction of Dr. L. Katz and in close collaboration with many other staff and students at the Accelerator Laboratory. Their contribution to both the design and construction are greatly appreciated.

Helpful discussions on diverse phases of this work were held with Drs. L. Katz and H. Caplan and D. Lobb, and D. McArthur, T. Drake and R. Hutcheon.

For the help and encouragement so willingly offered by Prof. J. Goldemberg, the author is deeply grateful.

The experimental measurements reported in this thesis were made with the assistance of Dr. H. Caplan, T. Drake, R. Hutcheon, D. McArthur, D. Morrison, R. Singhal and V. Stobie.

The illustrations in this thesis all were prepared by Mr. A. Hudak.

Financial assistance in the form of a National Research Council Studentship and a University of Saskatchewan Scholarship are gratefully acknowledged.

For her patience and encouragement during periods of frustration and set-back, and for her careful typing of the thesis draft, the author thanks his wife.

TABLE OF CONTENTS

TABLE OF CONTENTS (cont'd)

TABLE OF CONTENTS (cont'd)

LIST OF TABLES

LIST OF FIGURES

LIST OF FIGURES (cont'd)

CHAPTER 1

INTRODUCTION

Nuclear structure investigation by the technique of electron scattering has two fundamental advantages. First, unlike the case for nuclear projectiles, the interaction between an electron and a nucleus is entirely electromagnetic, hence in principle can be calculated exactly. Second, for a fixed energy transfer to the nucleus, the 3-momentum transferred to the nucleus, q, is not fixed as it is for photons, but may be varied within limits. These advantages have been pointed out by many authors, for example, Schiff (1954), Willey (1963) and deForest and Walecka (1966).

The electron scattering cross section may be related to the nuclear transition matrix elements using the techniques of quantum electrodynamics. This analysis is simplified by the fact that, for the incident energies used in electron scattering experiments, the electron mass may be neglected. Also plane wave (or first Born) analysis may be used to treat the incident and scattered electrons, since the electron wave-functions are not significantly distorted by the Coulomb field of the nucleus when target nuclei are light. Because the electron-nucleus interaction is relatively weak, the structure of the target nucleus is not greatly disturbed by the interaction.

When high energy electron pass through matter the following reactions with target nuclei occur*:

i) Elastic scattering by the nucleus.

---

*Meson production is ignored in this thesis because the maximum energy of electrons obtainable from the Saskatchewan accelerator is at present below meson threshold.

ii) Inelastic scattering by the nucleus.

iii) Scattering by the nucleus with emission of photons.

iv) Scattering with ionization of the matter.

From the experimentally measured electron spectra one can unfold individual contributions and thus obtain information relevant to the understanding of nuclear structure.* For example, the elastic form factor, a quantity directly related to the spatial distribution of nuclear charge, may be deduced from the elastic differential cross section. The inelastic differential cross section is related to nuclear transition matrix elements which also may be calculated on the basis of an assumed model of the nucleus. It is these transition matrix elements which are the meeting point of theory with experiment. Their experimental determination provides a stringent test for nuclear theories — much more stringent than measurements made at a fixed momentum transfer using photons, since the matrix element, measured over the whole spectrum of momentum transfers, may be compared with theory.

Electron scattering techniques have been used to investigate the behaviour with changing momentum transfer of excitation to bound nuclear levels and also to unbound levels such as those which constitute the giant dipole resonance in nuclei. The results of investigations of the dipole resonance in closed-shell nuclei have favoured the calculations by Brown and his co-workers (Brown et al 1961), based on the shell model of the nucleus, over those based

---

*The unfolding techniques used by the author are outlined in Chapter 5.

on the Goldhaber-Teller model of collective nuclear excitation (Goldhaber and Teller (1948)). In the Brown model, collectivity of the nuclear excitation results from interactions between nucleons promoted to higher shells and the holes which they leave behind in otherwise closed shells, whereas in the Goldhaber-Teller model all protons in the nucleus were thought to oscillate against all neutrons.

For several years criticism has been levelled at this simple treatment of the Goldhaber-Teller model. A recent collective model calculation by Überall (1966) which takes into account the spin dependence of nuclear forces has shown that in fact a number of giant resonances occur in nuclear matter in addition to the simple Goldhaber-Teller mode. For these resonances one may think of neutrons with spin up oscillating against protons with spin down, while neutrons with spin down are oscillating against protons with spin up (spin-isospin mode) or all nucleons with spin up oscillating against all nucleons with spin down (spin wave mode). In particular, the spin-isospin mode gives rise to a strong 2^- resonance in both ^{12}C and ^{16}O. Unfortunately, unlike the particle-hole calculations, the Goldhaber-Teller type nuclear collective calculations do not predict the excitation energy.

Vinh Mau and Brown (1962), using particle-hole techniques, predicted a level in ^{12}C at 19.2 MeV carrying over 70% of the magnetic quadrupole strength. Sanderson (1961) has shown that the level observed at 19 MeV by inelastic proton scattering is not inconsistent with the assignment 2^-, but he does point out that the experimental data do not preclude the assignment 0^-. However,

observation of the level by inelastic electron scattering does preclude it. Both Vinh Mau and Brown (1962) and Sanderson (1961) remark that the assignment of 2^- for the level in this region is consistent with the fact that no strong resonance was observed in photon work or in the inverse (p, γ_0) reaction. More recent particle-hole calculations by Vinh Mau as reported by Gillet and Vinh Mau (1964) show fair agreement between experimental proton angular distributions and the theoretical ones computed with the wave functions of a predicted 2^- T = 1 state at 19.4 MeV. Recently a particle-hole calculation which considers both 1^- T = 1 and 2^- T = 1 levels in ^{12}C and ^{16}O has been made by deForest (1965)*. The results of his calculation, which has as an underlying feature a spin dependent nuclear force, show three 2^- T = 1 levels in ^{12}C; one a strong state at 20.76 MeV, the other two, found at 19 MeV and 24 MeV in the calculation, are much weaker. deForest expects the calculated energy levels to be about 1 or 2 MeV too high, thus he has compared his calculated transverse matrix element $\langle 2^- \| T_2^{mag} \| 0^+ \rangle$ with the experimentally determined values for a level found at $\sim$19.5 MeV in inelastic electron scattering measurements.

Apart from an earlier inelastic spectrum of ^{12}C measured by Leiss and Taylor (1960), three sets of measurements have been made of the matrix element for inelastic electron scattering from the

---

*deForest's calculation along with that of Überall is discussed more thoroughly in Chapter 3.

level at 19.5 MeV in ^{12}C*. Two were made at 180° employing a system with a resolution of ~1 MeV (deForest et al (1965), deForest and Walecka (1966), and Goldemberg and Barber (1964)). The third was made at Darmstadt at scattering angles of 152° and 128° with a resolution of about 400 keV. These measurements, which are summarized in Fig. 6.3.1, span a range of inelastic momentum transfer from 60 MeV/c to 120 MeV/c. They show clearly that over this limited range of momentum transfers, the strength of the level increases rapidly with q, and that the data are not inconsistent with the calculated 2^- T = 1 matrix element of deForest (1965).

The Darmstadt measurements show that the level at 19.5 MeV is dominantly transverse in character at 152°.

Some confusion on the spin-parity assignment of this level has in the past existed in the literature (Goldemberg and Barber (1964)†). It was clear that an experimental measurement of the inelastic electron scattering cross section at higher momentum transfers would provide a sensitive test of the particle-hole calculations as well as providing further information on the spin-parity assignment of the level if the agreement with theory should be satisfactory. Such higher momentum measurements would clearly distinguish between

---

*A preprint by Crannell et al (1966) containing measurements made over a range of momentum transfers from 267 MeV/c to 643 MeV/c was received after preparation of the text in this thesis. The measurements, made at a scattering angle of 40°, were compared with the particle-hole calculations of Lewis and Walecka (1964) which predict a 1^- T = 1 level at 19 MeV in ^{12}C. Their data, discussed in Appendix C, are in satisfactory agreement with our results.

†See also Appendix C.

the predictions of particle-hole theory for an assumed 2^- T = 1 level and for the lowest 1^- T = 1 level as calculated by Lewis and Walecka (1964) and by deForest (1965). The reader is referred to Fig. 6.3.1 which shows results for both calculations.*

The present experimental knowledge of the nuclear matrix element for the 19.4 MeV level in ^{12}C would be improved significantly by two or three experimental points in the region between q = 150 MeV/c and 250 MeV/c, each measured to a precision of about $\pm 15\%$†. Because of the expected large number of close-lying levels, the measurement should be made with a resolution of $\sim$300 keV.

A similar strong 2^- T = 1 state in ^{16}O at $\sim$20 MeV is predicted by the calculations of deForest (1965), Überall (1966), and Gillet (1962). Inelastic electron scattering measurements by deForest et al (1965) made at 180° show that a level found at 20.2 MeV has the correct q dependence in the region $q < 120$ MeV/c. Previous ^{16}O measurements by Bishop and Isabelle (1962)‡ also indicated that there is a 2^- level in the vicinity of 19.2 MeV.

The author has for some years been interested in resolving the experimental uncertainty in this broad level in ^{16}O at 19.2 MeV.

---

*See also Appendix C.

†These measurements, combined with those of Crannell et al (1966) would span the diffraction minimum of the 1^- T = 1 level predicted by the calculation of Lewis and Walecka (1964).

‡In a paper by Bernheim and Bishop (1963) it is reported that the 2^+ level found at 19.2 MeV in this work has been resolved into two levels with assignments 2^+ and 2^-. Level energies are not given.

Electron scattering measurements made at 180^{o} (Vanpraet and Barber (1966)) show two peaks in this region, one at 19.5 MeV and the other, apparently the 2^{-} level, at 20.2 MeV. No analysis was made of the 19.5 MeV level data. However, the work of Bishop and Isabelle (1962) indicates that the level has a high multipolarity. Carter et al (1964), using the technique of elastic alpha scattering from ^{12}C, give evidence for a 2^{+} level in ^{16}O at an excitation energy of 19.1 MeV. Inelastic proton scattering data were compared with theoretical calculations by Erikson (1964) to make the assignment 2^{-} for an experimental level in ^{16}O found at 19 MeV. Clearly, the experimental measurements indicate an uncertainty as to which of the levels in ^{16}O in the range of excitation energies from 19 - 20 MeV has the assignment 2^{-}. Clarification of this uncertainty is essential to the understanding of the 2^{-}, or magnetic quadrupole resonance states in light closed-shell nuclei.

Further impetus to make detailed measurements of the properties of strong levels in the energy region below the giant resonance comes from the fact that the radiation tails from these levels make a significant contribution to the experimental background at higher excitation energy. In principle one needs an exact knowledge of all levels which contribute to the underlying structure before the background may be calculated for a specific level.

The calculations cited predict that some of the 2^{-} strength lies in the energy region of the giant dipole resonance both in ^{12}C and ^{16}O. The effect of these levels must be removed before comparing giant dipole resonance measurements with theory, or

conversely the theoretical calculation of the giant resonance should include the higher multipoles. Because the levels in the dipole resonance region are broad, it is not possible experimentally to separate closely spaced levels. Thus the second approach must be adopted. An experimental measurement of the excitation energy and the q dependence of the form factor for the one strong separated 2^- level in ^{12}C and ^{16}O would provide greater confidence in the calculated results for other levels. In particular, particle-hole calculations are not expected to predict the correct nuclear energy levels, but the level spacings are accurate.

To determine whether a strong 2^- resonance is a general feature of nuclear collective behaviour as predicted by the fact that only general properties of nuclei appear in the calculation by Überall (1966), the measurement, at q values up to $\sim$ 200 MeV/c, should then be extended to other light closed-shell nuclei.

The ^{12}C measurements reported in this thesis are thus the first of a series of electron scattering measurements which will study higher multipole resonances which occur in light closed-shell nuclei in the energy region of the giant dipole resonance. It is expected that the experimental data will add significantly to our knowledge of a quadrupole resonance in light nuclei. At present, theoretical calculations exist only for the nuclei ^{12}C and ^{16}O.

For the following reasons (primarily technical) we have chosen to begin the series with ^{12}C.

i) The carbon elastic form factor is well known. In fact, carbon is used as a secondary standard in

several laboratories.

ii) A larger number of measurements of the level has been made at momentum transfers below 100 MeV/c, thus comparison with previous work is more meaningful.*

iii) An isotopically pure ($>99\%$) self-supporting graphite target of the required thickness is readily available.

iv) The graphite target, being refractory, is not easily damaged by an intense electron beam.

The electron scatter facility at the Saskatchewan Accelerator Laboratory, described in detail in Chapter 4 of this thesis, may be used to achieve the following experimental conditions:

i) Maximum scattering angle: 155°.

ii) Maximum inelastic momentum transfer (excitation energy 20 MeV; $\theta = 155^{\circ}$): 250 MeV/c.

iii) Resolution (with thin target): $\sim 0.3\%$.

Clearly, these conditions are satisfactory for the proposed measurements of 2^- levels in ^{12}C, ^{16}O and other target nuclei.

In concluding this chapter it is instructive to compare the electron scatter facility at the Saskatchewan Accelerator Laboratory with those at several other Linac laboratories. This very general comparison (Table 1.1) is made on the basis of peak electron energy and overall resolution and stability, as quoted in research papers.

---

*Recent high momentum transfer measurements have been made by Crannell et al (1966).

Table 1.1

A comparison of several electron scattering facilities

Linac	$\mathcal{E}$ max (MeV)	Resolution (%)
Saskatchewan	140	0.3
Stanford: MKII(180^{o})	70	1.4
MKIII	820	0.5
Yale	65	0.15
Orsay	250	0.3
	1,300	
Darmstadt	60	0.15

CHAPTER 2

ELECTRON SCATTERING CROSS SECTIONS IN THE FIRST BORN APPROXIMATION

2.1 Introduction

The scattering of electrons by a nucleus is treated in the framework of quantum electrodynamics. The four-current associated with the electron interacts with the nuclear four-current by the exchange of virtual photons. If we calculate the scattering cross section in the first Born approximation, this is equivalent to treating the interaction as resulting from the exchange of a single virtual photon. The criteria for validity of the first Born approximation in calculating electron scattering cross sections may be expressed as $Z\alpha \ll 1$, and momentum transfer not too near a diffraction minimum. For ^{12}C, $Z\alpha = 0.044$ and the first diffraction minimum is at q = 360 MeV/c (Ehrenberg et al (1959)), hence use of the Born approximation is not expected to introduce a significant error over the region of momentum transfers investigated.

A further simplification results from treating the nucleus non-relativistically. This procedure was shown by Willey (1963) to be valid provided $(q/M_N) \ll 1$, where M_N is the mass of the target nucleus (regarded as a collective system), and q is the momentum transferred to it.

To summarize, the assumptions used in calculating the differential cross section are:

i) Both the incident and the scattered electron may be represented by plane waves which are solutions of the Dirac equation.

ii) First order perturbation theory is used to calculate the interaction.

iii) The nucleus is treated non-relativistically, the electron relativistically.

2.2 Theory

When an electron is scattered by a nucleus, its transition charge and current interact with the transition charge density $\rho_N(\vec{x})$, current density $\vec{j}_N(\vec{x})$, and magnetization density $\vec{\mu}_N(\vec{x})$ of the nucleus. The interaction matrix element, as expressed by Alder et al (1956) is

$$\langle f|H'|i\rangle = \int A^e_\mu(x)\, J^\mu_N(x)\, d^4x . \qquad (2.2.1)$$

$A^e_\mu(x)$ is the Møller potential of the electron transition charge and current. In the Lorentz gauge $\partial A^e_\mu/\partial x_\mu = 0$, and

$$A^e_\mu(x) = -\frac{4\pi e}{q_\nu^2}\, exp(-i q_\nu x^\nu)\, \bar{u}_2 \gamma_\mu u_1 , \qquad (2.2.2)$$

with $\bar{u}_2$ the adjoint of the final electron spinor and u_1 the initial electron spinor,

γ_μ a Dirac matrix,

and q_ν the 4-momentum transfer to the nucleus (an equation relating q_ν to experimentally known quantities is given in Section 2.3).

$J^\mu_N(x)$ may be expressed as a function of the nuclear charge, current, and magnetization densities.

$$J^\mu_N(x) = \left(\frac{1}{c}\vec{j}_N(\vec{x}) + \vec{\nabla}\times\vec{\mu}_N(\vec{x}),\ \rho_N(\vec{x})\right). \qquad (2.2.3)$$

The interaction matrix element (Eq. 2.2.1) may be rewritten in the following form:

$$\langle f|H'|i\rangle = -\left(\frac{4\pi e}{q_\nu^2}\right)(\bar{u}_2 \gamma_\mu u_1)\, j^\mu_N(q), \qquad (2.2.4)$$

where $j_N^{\nu}(q)$ is the Fourier transform of $J_N^{\nu}(x)$.

The cross section for the scattering process is obtained from this matrix element following standard procedures; the sum and average over electron spins is performed by converting to traces, the electromagnetic transition currents are decomposed into multipoles, and the density of final states is substituted into the expression for the cross section. The resulting differential cross section in the centre-of-mass system may be written, following the notation of deForest and Walecka (1966)

$$\frac{d\sigma}{d\Omega} = \frac{8\pi\alpha^2}{q_\nu^4}\left(\frac{K_2}{K_1}\right)\cdot\frac{1}{2J_i+1}\left\{V_L(\theta)\sum_{J=0}^{\infty}|\langle J_F\|\hat{M}_J^{coul}(q)\|J_i\rangle|^2 + V_T(\theta)\sum_{J=1}^{\infty}\left[|\langle J_F\|\hat{T}_J^{el}(q)\|J_i\rangle|^2 + |\langle J_F\|\hat{T}_J^{mag}(q)\|J_i\rangle|^2\right]\right\}, \tag{2.2.5a}$$

where

$$V_L(\theta) = \frac{1}{2}\frac{q_\nu^4}{\vec{q}^4}\,2K_1K_2\cos^2(\theta/2), \tag{2.2.5b}$$

and

$$V_T(\theta) = \frac{2K_1K_2}{\vec{q}^2}\sin^2(\theta/2)\left[(K_1+K_2)^2 - 2K_1K_2\cos^2(\theta/2)\right]. \tag{2.2.5c}$$

To obtain $V_L(\theta)$ and $V_T(\theta)$, the rest mass of the electron was set equal to zero. In these equations α is the Sommerfeld fine structure constant,

K_1 and K_2 are the initial and final wave numbers of the electron,

θ is the scattering angle of the outgoing electron relative to the incident electron,

$d\Omega$ is the solid angle into which the electron is scattered,

and $\vec{q}^2$ is the square of the 3-momentum transferred to the nucleus by the electron (see Section 2.3).

We choose a system of units in which $\hbar = c = 1$.

Each term of the form $|\langle J_F \| \hat{O}_J \| J_i \rangle|^2$ is the square of the reduced matrix element of the operator $\hat{O}_J$ between nuclear states labelled by internal angular momentum. It is defined by the relation

$$\langle J_F M_F | \hat{O}_{JM} | J_I M_I \rangle = (-)^{J_F - M_F} \begin{pmatrix} J_F & J & J_I \\ -M_F & M & M_I \end{pmatrix} \langle J_F \| \hat{O}_J \| J_I \rangle , \qquad (2.2.6)$$

with M the projection of the nuclear angular momentum J. The Wigner 3-j symbol which appears in this expression is defined in Edmonds (1960). Explicit expressions for the three operators as functions of the operators for nuclear charge $\hat{\rho}_N(\vec{x})$ nuclear current $\hat{j}_N(\vec{x})$ and nuclear magnetization density $\hat{\mu}_N(\vec{x})$ are given by deForest and Walecka (1966).

$$\hat{M}^{Coul}_{JM}(q) = \int j_J(qx)\, Y_{JM}(\Omega_x)\, \hat{\rho}(\vec{x})\, d\vec{x} \qquad (2.2.7a)$$

$$\hat{T}^{el}_{JM}(q) = \frac{1}{q}\int d\vec{x} \left\{ \vec{\nabla} \times j_J(qx)\, \vec{Y}^M_{JJ1} \cdot \hat{j}_N(\vec{x}) + \vec{q}^{\,2}\, j_J(qx)\, \vec{Y}^M_{JJ1} \cdot \hat{\mu}_N(\vec{x}) \right\} \qquad (2.2.7b)$$

$$\hat{T}^{mag}_{JM}(q) = \int d\vec{x} \left\{ j_J(qx)\, \vec{Y}^M_{JJ1} \cdot \hat{j}_N(\vec{x}) + (\vec{\nabla} \times j_J(qx)\, \vec{Y}^M_{JJ1}) \cdot \hat{\mu}_N(\vec{x}) \right\} . \qquad (2.2.7c)$$

The spherical harmonics Y_{JM}, vector spherical harmonics $\vec{Y}^M_{JJ1}$, and spherical Bessel functions $j_J(qx)$ which appear in these expressions are defined by Edmonds (1960).

To obtain the cross section in the laboratory system, Eq. (2.2.5a) is multiplied by the factor

$$\frac{1}{1 + \frac{2E_i}{M_N} \sin^2(\theta/2)} . \qquad (2.2.8)$$

In this equation $\mathcal{E}_1$ is the incident electron energy, and M_N is the mass of the target nucleus. Two approximations were used to obtain Eq.(2.2.8):

$$K_1 = K_2 ,$$

and $$m = 0 .$$

The scattering angle for the electron θ is essentially the same in the laboratory and centre-of-mass systems due to the great mass of the target nucleus relative to the electron (Willey, 1963).

The first term in Eq.(2.2.5a) comes from the interaction between the nuclear charge and the component of the electron current parallel to the vector $\vec{q}$. This is the Coulomb interaction and the term is called Coulomb or longitudinal.

The second and third terms come from the interaction between the nuclear currents and the component of the electron current perpendicular (transverse) to the vector $\vec{q}$.

The first and second term correspond to electric multipoles of order J; the third term to magnetic multipoles of order J, hence the second term is referred to as transverse electric, and the third as transverse magnetic.

The parity of the Coulomb and transverse electric terms is $(-)^J$ while that of the transverse magnetic term is $(-)^{J+1}$.

The angular momentum and parity selection rules for the nuclear transition were given by Alder et al (1956) and many other authors. In consistent notation they may be written

$$|J_F - J_I| \leqslant J \leqslant J_F + J_I , \qquad (2.2.9)$$

$$\pi_F \times \pi_J \times \pi_I \quad \text{is even.}$$

In this equation π_F and π_I are the parities of the final and initial nuclear state, and π_J is the parity of the electromagnetic multipole.

2.3 Kinematics of electron scattering

To express the differential cross section in terms of experimentally observed quantities, certain kinematic relations have been used. In this section we give the pertinent equations, all of which are based on the scattering process shown diagramatically in Fig. 2.3.1. A relativistic electron of rest mass m, energy ε_1

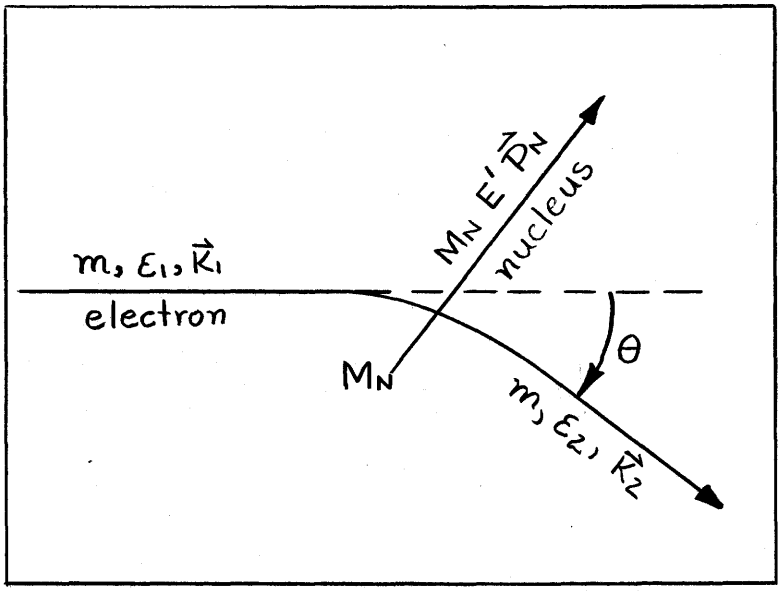

Fig. 2.3.1 Diagram of electron scattering kinematics.

and wave number $\vec{K}_1$ (momentum $\hbar\vec{K}_1$) is scattered through an angle θ by a nucleus of mass M_N, initially at rest in the laboratory system. The scattered electron has energy ε_2, wave number $\vec{K}_2$; the nucleus has final energy E' and momentum $\vec{P}_N$. In the

scattering process both momentum and energy are transferred to the nucleus, and the nucleus may be left in an excited state of energy $\mathcal{E}$ above its ground state energy.

The following kinematic relations were derived with the assumption

$$mc^2 \ll \mathcal{E}_1 \text{ and } \mathcal{E}_2 . \tag{2.3.1}$$

$$\mathcal{E}_1 = \frac{\mathcal{E}_2 + \mathcal{E} + \mathcal{E}^2/2M_N}{1 - \frac{2\mathcal{E}_2}{M_N}\sin^2(\theta/2)} , \tag{2.3.2a}$$

$$\text{and } \mathcal{E}_2 = \frac{\mathcal{E}_1 - \mathcal{E} - \mathcal{E}^2/2M_N}{1 + \frac{2\mathcal{E}_1}{M_N}\sin^2(\theta/2)} . \tag{2.3.2b}$$

deForest and Walecka (1966) give the following expression for the 4-momentum transferred to the nucleus

$$q_\nu^2 = \vec{q}^2 - \mathcal{E}^2 = 4\mathcal{E}_1\mathcal{E}_2 \sin^2(\theta/2), \tag{2.3.3}$$

where $\mathcal{E} = \mathcal{E}_1 - \mathcal{E}_2 \geq 0$,

and $\vec{q}^2 = \mathcal{E}_1^2 + \mathcal{E}_2^2 - 2\mathcal{E}_1\mathcal{E}_2 \cos\theta$.

Combining Eq. (2.3.2b) and Eq. (2.3.3),

$$q_\nu^2 = \frac{4\mathcal{E}_1(\mathcal{E}_1 - \mathcal{E} - \mathcal{E}^2/2M_N)\sin^2(\theta/2)}{1 + (2\mathcal{E}_1/M_N)\sin^2(\theta/2)} . \tag{2.3.4}$$

For an actual experimental measurement, the above expressions must be modified slightly to account for ionization energy loss resulting from the finite thickness of the target. In this case

$$\mathcal{E}_1 = \frac{\mathcal{E}_{E1} + \Delta\mathcal{E}_{ION}}{1 - (2\mathcal{E}_{E1}/M_N)\sin^2(\theta/2)} , \tag{2.3.5}$$

where $\mathcal{E}_{E1}$ was substituted for $\mathcal{E}_2$ to indicate that this is the most probable electron energy in the elastic peak. The term $\Delta\mathcal{E}_{ION}$ is the average ionization energy loss of electrons traversing the effective target thickness. A similar equation may be written for

$\mathcal{E}_{In}$, the energy of an inelastically scattered electron.

With the assumption that the ionization energy loss remains constant over the range of energies $\mathcal{E}_{In}$ measured during a scattering experiment, Eq. (2.3.2b) (with the added term accounting for ionization energy loss within the target) and Eq. (2.3.5) may be combined to yield an equation giving $\mathcal{E}$ as a function of experimentally measured quantities.

$$\mathcal{E} = \frac{(\mathcal{E}_{E1} - \mathcal{E}_{In})\left(1 + \frac{2\mathcal{E}_{E1}}{M_N}\sin^2(\theta/2)\right)}{1 + \mathcal{E}/2M_N} \qquad (2.3.6)$$

For the analysis used in this thesis the denominator was approximated by setting $\mathcal{E} = \mathcal{E}_{E1} - \mathcal{E}_{In}$.

2.4 Inelastic scattering of electrons

The electron scattering is termed inelastic if $\mathcal{E} > 0$. The nucleus, following excitation, may de-excite either by the emission of γ-rays or if the excitation energy is sufficiently high by nuclear disintegration.

To aid in the inelastic analysis, a convenient simplification of Eq. (2.2.5) may be obtained by making two approximations,

$$m = 0,$$

and $$\frac{q_\nu^2}{\vec{q}^2} = 1.$$

$$\frac{d\sigma}{d\Omega} = \frac{4\pi\sigma_M}{\left(1+\frac{2\mathcal{E}_1}{M_N}\sin^2(\theta/2)\right)(2J_I+1)}\left\{\sum_{J=0}^{\infty}|\langle J_F\|\hat{M}_J^{Coul}(q)\|J_I\rangle|^2 + \right. \qquad (2.4.1a)$$

$$\left.\left(\frac{1}{2}+\tan^2\left(\frac{\theta}{2}\right)\right)\sum_{J=1}^{\infty}\left(|\langle J_F\|\hat{T}_J^{el}(q)\|J_I\rangle|^2+|\langle J_F\|\hat{T}_J^{mag}(q)\|J_I\rangle|^2\right)\right\},$$

$$\text{where } \sigma_M = \frac{\alpha^2\cos^2(\theta/2)}{4\mathcal{E}_1^2\sin^4(\theta/2)}, \qquad (2.4.1b)$$

sometimes termed the Mott cross section.

For the specific case of target nuclei with spin zero,

$$\frac{d\sigma}{d\Omega} = \frac{Z^2 \sigma_M}{1+(2\varepsilon_1/M_N)\sin^2(\theta/2)} \left\{ \frac{4\pi}{Z^2} \left[\sum_{J=0}^{\infty} |\langle J_F \| \hat{M}_J^{coul}(q) \| 0 \rangle|^2 + \left(\frac{1}{2} + \tan^2\left(\frac{\theta}{2}\right)\right) \sum_{J=1}^{\infty} \left(|\langle J_F \| \hat{T}_J^{el}(q) \| 0 \rangle|^2 + |\langle J_F \| \hat{T}_J^{mag}(q) \| 0 \rangle|^2 \right) \right] \right\} \quad (2.4.2)$$

Eq. (2.4.2) also may be written in the form (Bishop, 1965)

$$\frac{d\sigma}{d\Omega} = \frac{Z^2 \sigma_M}{1 + \frac{2\varepsilon_1}{M_N}\sin^2(\theta/2)} \left[F_L^2(q) + \left(\frac{1}{2} + \tan^2\left(\frac{\theta}{2}\right)\right) F_T^2(q) \right]. \quad (2.4.3)$$

The terms $F_L(q)$ and $F_T(q)$ are called the longitudinal and transverse inelastic form factors respectively.

It is clear from Eq. (2.4.2) that when the scattering angle is large, the transverse terms contribute strongly to the measured differential cross section. In the limit of 180° scattering, only the transverse terms contribute. The differential cross section simplifies to

$$\frac{d\sigma}{d\Omega} = \frac{\pi\alpha^2}{\varepsilon_1 \varepsilon_2} \left\{ \frac{1}{2J_i+1} \sum_{J=1}^{\infty} \left(|\langle J_F \| \hat{T}_J^{el}(q) \| J_i \rangle|^2 + |\langle J_F \| \hat{T}_J^{mag}(q) \| J_i \rangle|^2 \right) \right\}. \quad (2.4.4)$$

Eq. (2.4.2) is further simplified if we consider only transverse terms.

$$\frac{d\sigma}{d\Omega} = \frac{Z^2 \sigma_M}{1 + \frac{2\varepsilon_1}{M_N}\sin^2\left(\frac{\theta}{2}\right)} \left\{ \frac{4\pi}{Z^2} \left(\frac{1}{2} + \tan^2\left(\frac{\theta}{2}\right)\right) \sum_{J=1}^{\infty} \left(|\langle J_F \| \hat{T}_J^{el}(q) \| 0 \rangle|^2 + |\langle J_F \| \hat{T}_J^{mag}(q) \| 0 \rangle|^2 \right) \right\} \quad (2.4.5)$$

$$= \frac{Z^2 \sigma_M}{1 + \frac{2\varepsilon_1}{M_N}\sin^2(\theta/2)} \left(\frac{1}{2} + \tan^2(\theta/2)\right) F_T^2(q).$$

The reduced matrix elements in the preceding expressions contain all the nuclear information obtainable from the scattering of high energy electrons. Experimental measurements of these matrix elements for specific nuclear levels are compared with values for these matrix elements calculated on the basis of assumed nuclear models. When a specific nuclear level of given spin and parity is considered, the number of terms in the sum over multipoles is greatly reduced as a result of the selection rules (Eq. 2.2.9).

2.5 Elastic scattering of electrons

For the case of elastic electron scattering the final state of the nucleus is identical to the initial state, hence $J_F = J_I$. For the specific case of spin 0 nuclei, selection rules eliminate all but the J = 0, or monopole term. The differential cross section for elastic scattering from spin zero nuclei is thus

$$\frac{d\sigma}{d\Omega} = \frac{Z^2 \sigma_M}{1 + \frac{2\epsilon_1}{M_N} \sin^2(\theta/2)} \left\{ \frac{4\pi}{Z^2} |\langle 0 \| \hat{M}_0^{Coul}(q) \| 0 \rangle|^2 \right\}, \qquad (2.5.1)$$

where $$\sigma_M = \frac{\alpha^2 \sin^2(\theta/2)}{4 \epsilon_1^2 \cos^4(\theta/2)} .$$

Eq. (2.5.1) may be rewritten

$$\frac{d\sigma}{d\Omega} = \left[\frac{Z^2 \sigma_M}{1 + \frac{2\epsilon_1}{M_N} \sin^2(\theta/2)} \right] |F_{E1}(q)|^2 . \qquad (2.5.2)$$

The term in square brackets in Eq. (2.5.2) is the differential cross section for elastic scattering by a point nucleus of charge Z in the laboratory system, and the factor $F_{E1}(q)$ is the elastic form factor of the target nucleus. This form factor results from

the fact that the nuclear charge is distributed throughout a finite volume.

The elastic scattering technique has been used to measure the radial nuclear charge distribution of many nuclei. For nuclei in the 1p shell, satisfactory agreement has been obtained between experimental results and the form factor derived from a charge distribution based on harmonic oscillator wave-functions.

The radial dependence of the harmonic oscillator wave-functions as given by Talmi (1952) and quoted by Bishop (1965) is

$$\text{s-shell:}\quad R_0(r) = 2\left(\frac{\nu^3}{\pi}\right)^{1/4} \exp\left(-\nu r^2/2\right), \tag{2.5.3a}$$

$$\text{p-shell:}\quad R_1(r) = \sqrt{\frac{8}{3}}\left(\frac{\nu^5}{\pi}\right)^{1/4} r \exp\left(-\nu r^2/2\right). \tag{2.5.3b}$$

For 2 protons in the s-shell and $(Z-2)$ protons in the p-shell, and a spherically symmetric charge distribution, the charge density is

$$\rho(r) = \frac{1}{4\pi Z}\left[\, 2 R_0^2(r) + (Z-2) R_1^2(r) \right]. \tag{2.5.4}$$

This expression has been normalized to a total nuclear charge of unity. Combining Eq. (2.5.4) and Eq. (2.5.3), the equation for $\rho(r)$ may be written in the form

$$\rho(r) = \frac{8K^3}{4\pi^{3/2} a^3 (2+3\alpha)}\left\{1 + \alpha \frac{K^2 r^2}{a^2}\right\} \exp\left(-\frac{K^2 r^2}{a^2}\right). \tag{2.5.5a}$$

The notation used in this equation is equivalent to that of Hofstadter (1957) and Herman and Hofstadter (1960). The root-mean-square radius of the charge distribution, a, is related to other shell model parameters by the equations

$$a = K a_0 = K\left(\frac{\hbar^2}{ME}\right)^{1/2}, \qquad (2.5.5b)$$

and

$$\nu^{-1} = a_0, \qquad (2.5.5c)$$

where E is the energy interval between the successive levels of the harmonic oscillator,

M is the proton mass,

$$K = \sqrt{\frac{3(2+5\alpha)}{2(2+3\alpha)}}$$

and $\alpha = \frac{1}{3}(Z-2)$.

The analytic expression for $F_{E1}(q)$ obtained for the charge distribution of Eq. (2.5.5) is (Herman and Hofstadter, 1960)

$$F_{E1}(q) = \left[1 - \frac{\alpha q^2 a^2}{2K^2(2+3\alpha)}\right] \exp\left(-\frac{q^2 a^2}{4K^2}\right). \qquad (2.5.6)$$

CHAPTER 3

OUTLINE OF NUCLEAR MODEL CALCULATIONS FOR ^{12}C

3.1 Particle-hole calculations for 2^- levels

The experimentally measured form factors for the 19.4 MeV level in ^{12}C are in satisfactory agreement with theoretical calculations by deForest (1965) which predict a 2^- level in ^{12}C at 20.76 MeV. We give in this section only the underlying assumptions of his calculation; details may be obtained in papers by deForest (1965), deForest et al (1965), and deForest and Walecka (1966).

The excited states of ^{12}C in the particle-hole model are obtained by diagonalizing the nuclear Hamiltonian between shell model states in which one nucleon is in an excited state leaving a hole in the otherwise filled shell. The three shell model configurations considered in the calculation of 2^- excitations were $2s_{1/2}(1p_{3/2})^{-1}$, $1d_{5/2}(1p_{3/2})^{-1}$ and $1d_{3/2}(1p_{3/2})^{-1}$. The matrix element of the Hamiltonian was divided into two parts, one, which may be identified as the energy of the hole and particle without an interaction between them, is determined from the energy levels of neighbouring $(A\pm1)$ nuclei. The remaining part, the particle-hole interaction, may be determined from the internucleon potential, which for this calculation was chosen to be Yukawa potential with a Serber exchange mixture. The potential is written $v(r_{12}) = (V_0/\mu r)e^{-\mu r}$,

with $^1V_o = -46.87$ MeV $\quad$ $^1\mu = 0.8547\ F^{-1}$

$^3V_o = -52.13$ MeV $\quad$ $^3\mu = 0.7261\ F^{-1}$.

Thus the elements of spin dependence included in the calculation were the spin-orbit splittings in the configuration energies, and

the correct low energy singlet-triplet difference in the nuclear force.

The single-particle shell model states were taken to be harmonic oscillator wave functions with the oscillator parameter ($1.6/\sqrt{2}$) determined by fitting Coulomb energy differences in mirror nuclei.

The matrix element $\langle 2^- \| T_2^{mag}(q) \| 0^+ \rangle$ for the 20.76 MeV T = 1 state in ^{12}C was calculated using the above nuclear wave functions and the transverse operator

$$\hat{T}^{mag}_{2M}(q) = \int d\vec{x} \left\{ j_2(qx) \vec{Y}^M_{221} \cdot \hat{j}_N(\vec{x}) + \left(\vec{\nabla} \times j_2(qx) \vec{Y}^M_{221} \right) \cdot \hat{\mu}_N(\vec{x}) \right\}, \quad (3.1.1)$$

expressed in terms of single particle operators.

deForest et al (1965) give justification, based on sum-rule considerations, for using one-half of the calculated matrix element to compare with experimental values. It is this result which is plotted in Fig. 6.3.1.

deForest et al (1965) also give the long wavelength form of the isovector part of the magnetic quadrupole operator written in terms of 1 body operators.

$$\hat{T}^{mag}_{2M}(q) \underset{q \to 0}{\to} \frac{1}{4\sqrt{5\pi}} \frac{i q^2}{2 M_N C} \sum_{i=1}^{A} \tau_3(i) \left\{ \left[(\lambda_p - \lambda_N) \vec{\sigma}_i + \frac{2}{3} \vec{\ell}(i) \right] \odot \vec{x}(i) \right\}_{2M}. \quad (3.1.2)$$

Since we are concerned only with the q dependence of this expression we note that this operator is proportional to q^2, hence the squared matrix element is expected to grow as q^4 in the low momentum transfer region. This behaviour has been experimentally verified as reported in Chapter 6.

3.2 The generalized Goldhaber-Teller calculation of giant collective multipole states

The giant electric dipole resonance was described by Goldhaber and Teller (1948) as a collective oscillation of all protons in the nucleus against all neutrons in the nucleus. Goldemberg et al (1963) described the Goldhaber-Teller mode by a quantized oscillator model. Überall (1966) points out that theories of nuclear matter show that as well as this mode of vibration, there exist others. He has generalized the treatment by Goldemberg et al (1963) to include vibrational modes in which protons with spin up and neutrons with spin down move against protons with spin down and neutrons with spin up (spin -isospin mode), and in which nucleons with spin up move against nucleons with spin down (spin-wave mode).

This more general treatment gives the following simple expression for the 2^- differential cross section for inelastic electron scattering based on the spin-isospin mode.

$$\left(\frac{d\sigma}{d\Omega}\right)^{2^-}_{S\text{-}iS} = \frac{K_2 \alpha^2 \; F'^2(q_{E1})}{K_1 \, q_\nu^4 \; AM\epsilon}\left(\frac{\mu_P - \mu_N}{2}\right)^2 \frac{q_{In}^4}{M^2} V_T(\theta), \qquad (3.2.1)$$

with μ_P and μ_N the total magnetic moments of the proton and neutron,

M the nucleon mass,

and other notation the same as in Chapter 2, except that the elastic form factor F' is not normalized to unit charge, thus $F' = Z\,F$.

We may rewrite Eq. (3.2.1) in the form

$$\left(\frac{d\sigma}{d\Omega}\right)^{2^-}_{S\text{-}iS} = \frac{8\pi\alpha^2}{q_\nu^4}\left(\frac{K_2}{K_1}\right)\left\{V_T(\theta)\left[\frac{1}{8\pi}\frac{F'^2(q_{E1})}{MA\epsilon}\left(\frac{\mu_P - \mu_N}{2}\right)^2 \frac{q_{In}^4}{M^2}\right]\right\}. \qquad (3.2.2)$$

A comparison with Eq. (2.2.5a) shows that we may write the nuclear matrix element in the form

$$|\langle 2^- \| \hat{T}_2^{mag}(q) \| 0^+ \rangle|^2 = \frac{1}{8\pi} \frac{E_{E1}^2(q) Z^2}{MA\varepsilon} \left(\frac{\mu_P - \mu_N}{2}\right)^2 \frac{q_{In}^4}{M^2} . \qquad (3.2.3)$$

Überall has used Eq. (3.2.1) with a simple ground state charge form factor and a calculated level width of 1.8 MeV to predict the shape of the ^{12}C inelastic electron scattering spectrum in the region of 19 MeV. The results compare favourably with the spectrum of deForest et al (1965).

We have chosen instead to evaluate Eq. (3.2.3) for the transverse matrix element, and in this way to get a more direct comparison with experimental results. In this calculation we have substituted the more realistic harmonic well model for the ground state charge form factor of ^{12}C (Section 6.1.4). The values $\mu_P = 2.79$ and $\mu_N = -1.91$ were used. Three values of the matrix element for inelastic momentum transfers of 103.0-, 163.8-, and 225.9-MeV/c are given in Table 3.2.1.

Table 3.2.1

Calculated values of $|\langle 2^- \| T_2^{mag}(q) \| 0^+ \rangle|^2$

E_i MeV	q_{in} MeV/c	$\lvert\langle 2^- \| T_2^{mag}(q) \| 0^+ \rangle\rvert^2$
63.7	103.0	0.00216
94.9	163.8	0.00512
127.2	225.9	0.00384

These values are not directly comparable with the experimental matrix element of a single level since they represent the total 2^-, T = 1 strength. In fact, the particle-hole calculations of

Vinh Mau and Brown (1962) and deForest (1965) show that $\sim$30% of the M2 strength lies in levels other than at 19.4 MeV.

By reducing the calculated results of Table 3.2.1 by 30% we get values which show the same trend with q and are at most 20% higher than the values of deForest (1965).

CHAPTER 4

EQUIPMENT USED FOR ELECTRON SCATTERING EXPERIMENTS

4.1 Introduction

Before giving a detailed description of the components in the system, we give a brief outline indicating the equipment involved. To simplify the treatment we group the equipment into four categories.

i) The linear accelerator (supplied by Varian Associates).

ii) The magnetic components of the electron beam analyzing and transport system (supplied by Spectromagnetic Industries).

iii) The mechanical components of the highly evacuated beam transport system.

iv) The electron scattering facility.

Fig. 4.1.1 gives the relationship between the components, all of which are located in the basement of the Accelerator Laboratory.

The linear accelerator produces a beam of electrons with well defined but variable energy and variable current.

The beam, after leaving the accelerator, drifts in the evacuated transport system through the magnetic components of the analyzing system.

The analyzing system focuses the beam achromatically on the electron scatter target. The magnetic elements are used to determine precisely the transmitted electron beam energy while at the same time dispersing it for momentum analysis by adjustable slits. The energy spread within the beam may be adjusted by the slits S1 which intercept the dispersed beam. The system also stabilizes the beam

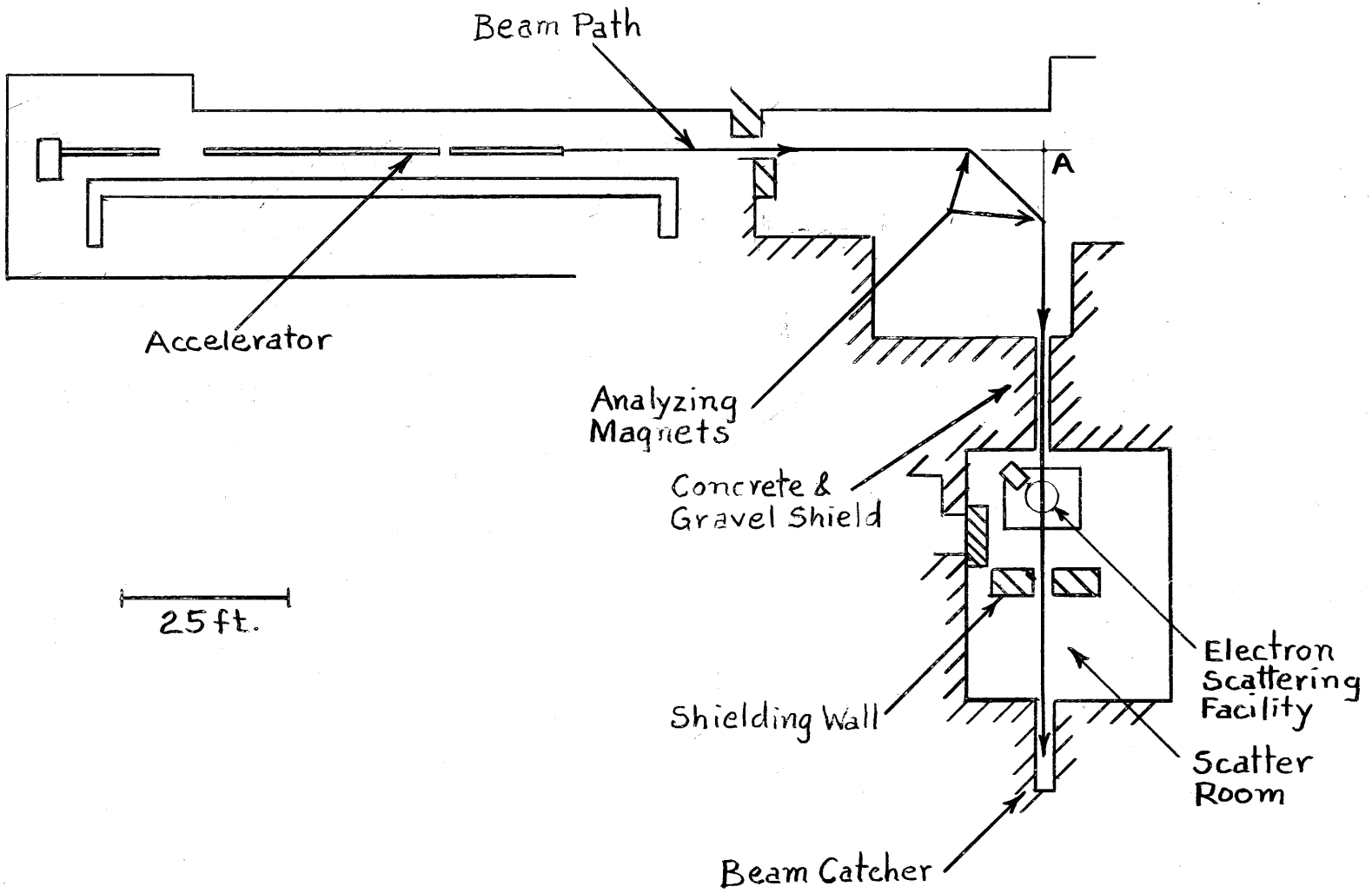

Fig. 4.1.1 Plan view of accelerator, beam transport system and electron scatter facility.

position at the scatter target. To achieve this stability, an adjustable entrance collimator (C1) is imaged horizontally on the energy defining slits S1, and vertically on the scatter target. Quadrupole pair Q1 focusses the accelerator beam onto this collimator to maintain an overall transmission as high as 90%.

Magnet M2 sweeps out all of the unwanted electrons coming from slits S1 and bends the primary energy - analyzed beam through 45^{o} to rid it of the copious quantity of γ-rays and neutrons which were produced in the slits. Quadrupole pair Q3 focusses the energy-analyzed beam on the scatter target. The target beam spot, which is imaged on the spectrometer detector , is kept small vertically to maintain an overall high resolution.

This analyzed electron beam is used to perform elastic and inelastic electron scattering experiments. Electrons, scattered at a known angle through a vertically-mounted double-focussing spectrometer, are detected by a counter telescope set to accept a small band of momenta. The energy of the detected electrons is determined precisely by a continuous measurement of the spectrometer magnetic field.

The overall stability of the magnetic systems coupled with the small vertical spot size on the scatter target permit a precise measurement of the excitation energy ε .

The precise determination of both incident energy and excitation energy are essential to the study of nuclear structure by the technique of electron scattering. Both the incident energy ε_1 and the momentum transfer (a function of ε_1 and θ) were shown in Chapter 2 to be fundamental quantities in the theory.

Scattered electron spectra are obtained in the following way. At a fixed incident energy and scattering angle, counts of the number of scattered electrons per unit incident charge are obtained for various spectrometer field settings. The incident charge is determined from a continuous beam current measurement made with a secondary emission monitor. A quantity proportional to $d^2\sigma/d\Omega d\varepsilon_f$ is obtained from the normalized count by applying a dispersion correction. This correction accounts for a variation in energy width of the detector with spectrometer field. The spectrum so obtained may be related to the nuclear differential cross section derived in Chapter 2 by using the analysis techniques outlined in Chapter 5.

The system used in making the inelastic electron scattering measurements reported in this thesis is not the ultimate scattering facility which can be installed at Saskatchewan. Both the beam energy and the power of the linac can be increased and the power handling capabilities of the beam handling system can be raised. Also, there are several advantages in replacing some of the components in the spectrometer assembly. We limit the following detailed description to components which were used for the present measurements.

Typical electron spectra obtained with the system are presented in Section 4.7.7. They show clearly that the following experimental parameters have been achieved.

i) Resolution: 90 keV FWHM.

ii) Stability and Reproducibility: equivalent to an energy shift of $< \pm 15$ keV.

The reader may omit the remainder of this chapter without loss of continuity. It contains a more detailed description of the accelerator, the beam analyzing and transport system, and the electron scatter facility.

4.2 The Saskatchewan electron linear accelerator

The Varian Associates model V-7713 electron Linac is a 4-section 2-Klystron S-band travelling wave machine, operating in the TM_{010} mode. Table 4.2 lists manufacturers specifications, most of which are pertinent to the use of the machine for electron scattering experiments.

Table 4.2

Manufacturers specifications for model V7713 Linac

	Guaranteed	Design
Beam energy, loaded:	98	103 MeV
Beam energy, unloaded:	130	136 MeV
Beam current, peak (at 98 MeV):	158	166 mA
Beam pulse length:	.005 to 1.0	.001 to 1.0 μsec
Energy spread (at 50% integrated current):	5	2 MeV
At 624 pulses per second		
Beam pulse length:	1.0	1.0 μsec
RF flat-top:	1.78	1.78 μsec
Average beam current:	98	103 μA
Average beam power:	9.6	10.6 kW

Table 4.2 (cont'd)

	Guaranteed	Design
Length of first accelerator section	-	3.3 meters
Length of second, third and fourth sections	-	4.83 meters
Number of klystrons TV TH2011B:	-	2
Average RF power per klystron		20 kW
Angular divergence, above 15 MeV	-	1 milliradian
Beam diameter, 90% current		
Above 15 MeV:		1 cm
Below 15 MeV:		1.5 cm

The four accelerator sections are located in a basement room in the Accelerator Laboratory (see Fig. 4.1.1). Power is fed to them from two klystrons located above ground. Each accelerator section is a disc-loaded waveguide mounted on adjustable support stands which place the centreline ~4 feet above floor level. The four accelerator sections were aligned with reference to an optical line, referred to as the accelerator axis. This axis was established using a transit placed 4 feet above the floor at position "A" shown on Fig. 4.1.1 to sight on the centre of the accelerator injection system. The positions of all components of the experimental system described in this chapter were measured with respect to the accelerator axis and the accelerator output flange.

During operation, the internal pressure in the disc-loaded waveguides is maintained between 10^{-6} and 10^{-7} Torr by five 40 litre

per second VacIon* pumps.

A water-cooled aluminum collimator at the outlet of the fourth section confines the beam to be within a 5/8 inch diameter. Beam steering coils on all four accelerator sections are used to achieve maximum beam transmission through the accelerating structure and output collimator, and to steer the beam so that it is coaxial with the accelerator axis.

An energy analysis of the beam can be made at a point just beyond the output collimator. This is accomplished by a pulsed magnetic spectrometer which samples a small fraction of the electron beam pulses (typically 1 in 120) and provides information on beam energy and energy spread. This system is used to set output energy and to minimize energy spread.

4.3 Analyzing magnets and quadrupoles

The design specifications for the beam analyzing system, consisting of magnets and quadrupoles built by Spectromagnetic Industries, Hayward California, are given in Table 4.3.1.

Table 4.3.1

Performance specifications for Spectromagnetic Industries achromatic beam analysis system

Resolution:	1 part in 2000 measured between half intensity points over energy range 10 MeV to 250 MeV.
Dispersion at S1:	0.635 inches per percent.

*Registered Trademark, Varian Associates, Palo Alto, California.

Table 4.3.1 (cont'd)

Transmission:	Better than 90% of the incident beam entering Magnet M1 for a momentum band within that corresponding to the aperture of the energy defining slits (S1).
At electron scatter target:	
Beam spot size:	For a 0.25% slit setting, 90% of the beam will fall within a horizontal dimension of 5 mm and a vertical dimension of 2.5 mm provided the Linac emittance angle is $\leqslant 1$ m radian.
Beam spot stability:	Centroid shift of $\pm$10% of guaranteed spot size over an 8 hour period.
Energy stability:	Design: 1 part in 5000 over a 1 hour period. Guarantee: 1 part in 2000 over 1 hour period.
Degaussing:	Residual field in magnets M1 and M2: 0.4 Gauss after degauss cycle.
Energy calibration of horizontal entrance slits C1:	2.57 inches per percent.

The first of the two 45° magnets M1 has a 30 inch radius of curvature and a $2\frac{1}{4}$ inch gap between the poles. The input effective field boundary is rotated through an angle $\beta = 19^{\circ}$ (see Fig. 4.3.1) to achieve double focussing. The radial waist was chosen to be in front of the quadrupole doublet Q2, whereas the vertical waist was displaced somewhat in order to enlarge the beam vertically at the energy defining slits S1. By placing the horizontal waist in front of the quadrupole pair Q2, the dispersion of the system is made independent of the properties of the quadrupoles. However, the quadrupoles Q2 are susceptible to radiation damage from the electrons scattered by slits S1, and protective shielding is required.

The second 45° magnet M2 is a mirror image of M1. Care was taken during its construction to insure that the magnetic properties were almost identical to those of magnet M1.

Power supply controls for all of the magnetic elements of the analyzing and transport system are located in the Linac control room. Magnets M1 and M2 and quadrupole pair Q2 are series connected and powered by a 27.5 kilowatt supply with current regulation of 1 part in 10,000 for $\pm$5% input line voltage changes. Quadrupoles Q1 and Q3 are separately powered.

Each of the magnetic elements of the system was optically aligned with respect to the accelerator axis or secondary axes (M2 to scatter target, and M1 to M2) following procedures outlined in Section 4.2. The alignment, made with respect to scribe marks placed on the components by the manufacturer, placed the components on the axes within $\pm$1/32 inch; distances between components were set to

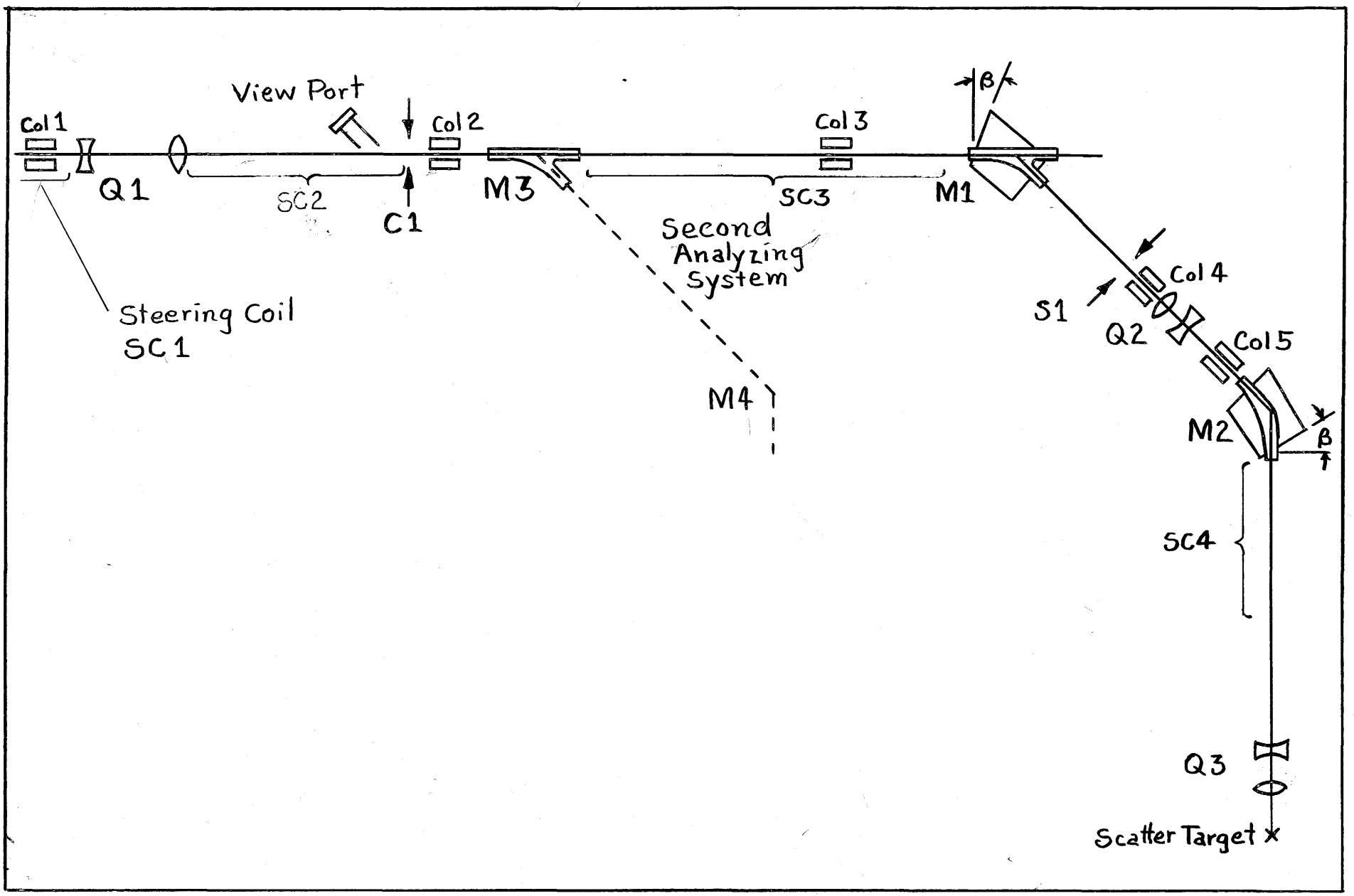

Fig. 4.3.1 Essential components of the beam analyzing and transport system.

within ±1/32 inch.*

The experimentally determined operating characteristics of this system are given in Section 4.7.1.

4.4 Beam transport system

4.4.1 Introduction

The beam transport system is a highly evacuated path along which the electrons drift from the accelerator, through the magnetic components described in the preceding section, to the scatter target chamber. The initial adjustment of the accelerator is made with the magnets off, hence the transport system also extends straight through magnet M1 and is terminated by an air-cooled 0.009-inch-thick aluminum vacuum window.

The transport system, shown in outline in Fig. 4.3.1, meets the following basic requirements:

i) It does not restrict the passage of the electron beam significantly. To insure this, both the size and position of mechanical components were chosen on the basis of first-order beam optics calculations (Beer (1965b)) using TRANSPORT, a computer program described by Lobb (1966).

ii) It operates at a pressure of $\sim 10^{-7}$ Torr to permit coupling to the accelerator vacuum, and to prevent air scatter and excessive bremsstrahlung production.†

*Measured values are given by Beer (1965a).

†Bremsstrahlung production, which gives rise to a contamination of the electron beam by γ-rays, is calculated in Appendix A.

iii) It contains only materials which operate reliably in a high radiation field. An all-metal vacuum system pumped by sputter-ion pumps was used.

iv) The two sets of remotely-operated slits (C1 and S1) discussed in Section 4.4.3 are built into the vacuum system.

v) The system contains water-cooled collimators discussed in Section 4.4.2 to prevent a high-power electron beam from striking and damaging the magnets and quadrupoles.

vi) Components in the transport system itself are protected against damage by the high-power electron beam by water cooling the magnet boxes, collimators and slits.

vii) The system is flexible. Individual components, made with ConFlat* all-metal vacuum joints, are removable and additions and alterations to the structure may be made easily.

viii) It contains beam steering components discussed in Section 4.4.4 and beam viewers discussed in Section 4.4.5.

4.4.2 Vacuum components

The vacuum design of the transport system is discussed in an unpublished design note by the author (Beer (1964b)). A realistic

*Registered Trademark, Varian Associates, Palo Alto, California.

surface outgassing rate for stainless steel is 5×10^{-10} Torr-litres/cm^2-sec . For this rate, 50-litre/sec vacuum pumps must be spaced at ~40 foot intervals along 2½-inch-diameter leak-free tube to maintain it at 10^{-7} Torr. In the note it is shown that if components have a leak rate of 10^{-8} Torr litres/sec-ft there will be no significant increase in the base pressure of 10^{-7} Torr. All components installed in the transport system had leak rates of $< 5 \times 10^{-10}$ Torr-litres/sec.

The vacuum system layout shown in Fig. 4.4.1 is based on the above considerations but account was taken of the surface area of the components. With the six fifty-litre/sec Ultek sputter-ion type pumps (marked P2-P7) a pressure of 10^{-7} Torr is easily achieved. Since the pumps must be started at a pressure $< 10^{-3}$ Torr, a portable turbo-molecular pump may be coupled to one of several pump ports (pp) to lower individual sections of the transport system to a starting pressure of 10^{-4} Torr.

During adjustment of the analyzing system, or as a result of a malfunction, the electron beam may strike the wall of the transport system. Damage is prevented by strategically located collimators which protect uncooled sections of stainless steel beam pipe. Side walls of the magnet boxes, which cannot be protected in this way, are also water cooled. Design of these components is based on equations given in a Saskatchewan Accelerator Laboratory Internal Report (Beer (undated)).

The basic design philosophy of the collimator shown in cross

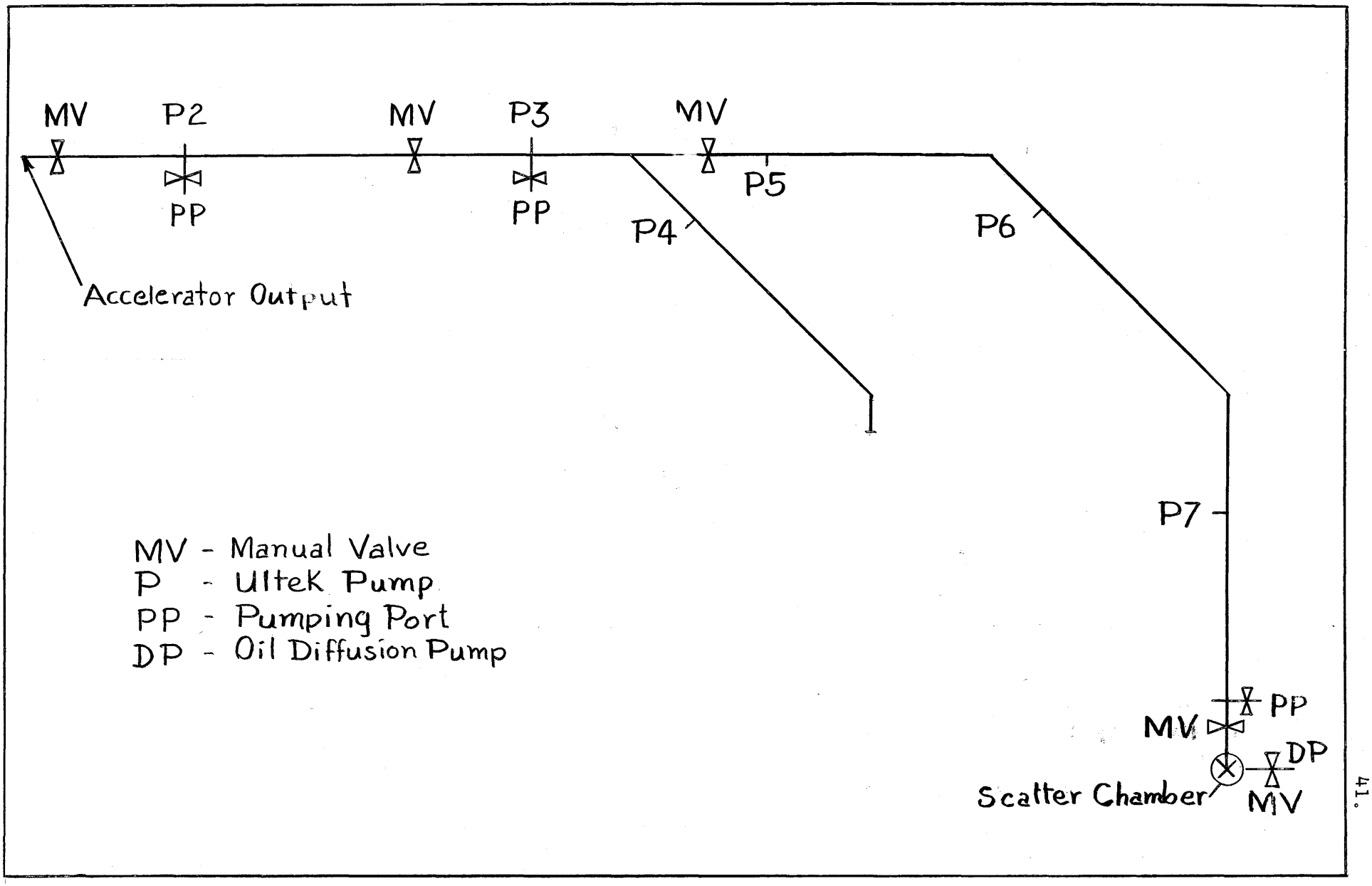

Fig. 4.4.1 Schematic diagram of vacuum system.

section in Fig. 4.4.2 is to provide a vacuum seal with a thin layer of high-strength material cooled by a rapid flow of water over the outer surface. The water is confined to flow in a narrow annulus so that surface velocity of the coolant is kept high with a minimum flow rate. With this design, damage from local heating caused by a high-current small-diameter beam is minimized. The electron beam, following impingement on the vacuum wall, is broadened in passing through the 10-inch-thick water chamber. When it strikes the water-cooled copper absorbing block, the beam diameter is sufficiently large that local heating is not serious for a beam power as great as 30 kW, provided a flow of 5 gallons/minute is maintained.

The vertical side walls of the magnet boxes in magnets M1-M4 also are cooled by water flowing at a high velocity in a one-inch-high 3/32-inch-thick channel. As a result of misadjustment, the beam can strike these walls without causing damage. However, it is not totally absorbed, hence can cause damage in other components if corrective measures are not taken.

4.4.3 Adjustable slits

Three sets of adjustable slits are required for operation of the energy analyzing system; vertical and horizontal slits C1, and horizontal slits S1. The jaws of each pair of slits are situated within the transport system, the vacuum joint between the jaw and the housing being made with a stainless steel bellows. The jaws are moved by two remotely controlled motor driven screws. The position of the jaws is measured by a 10-turn precision resistor mechanically

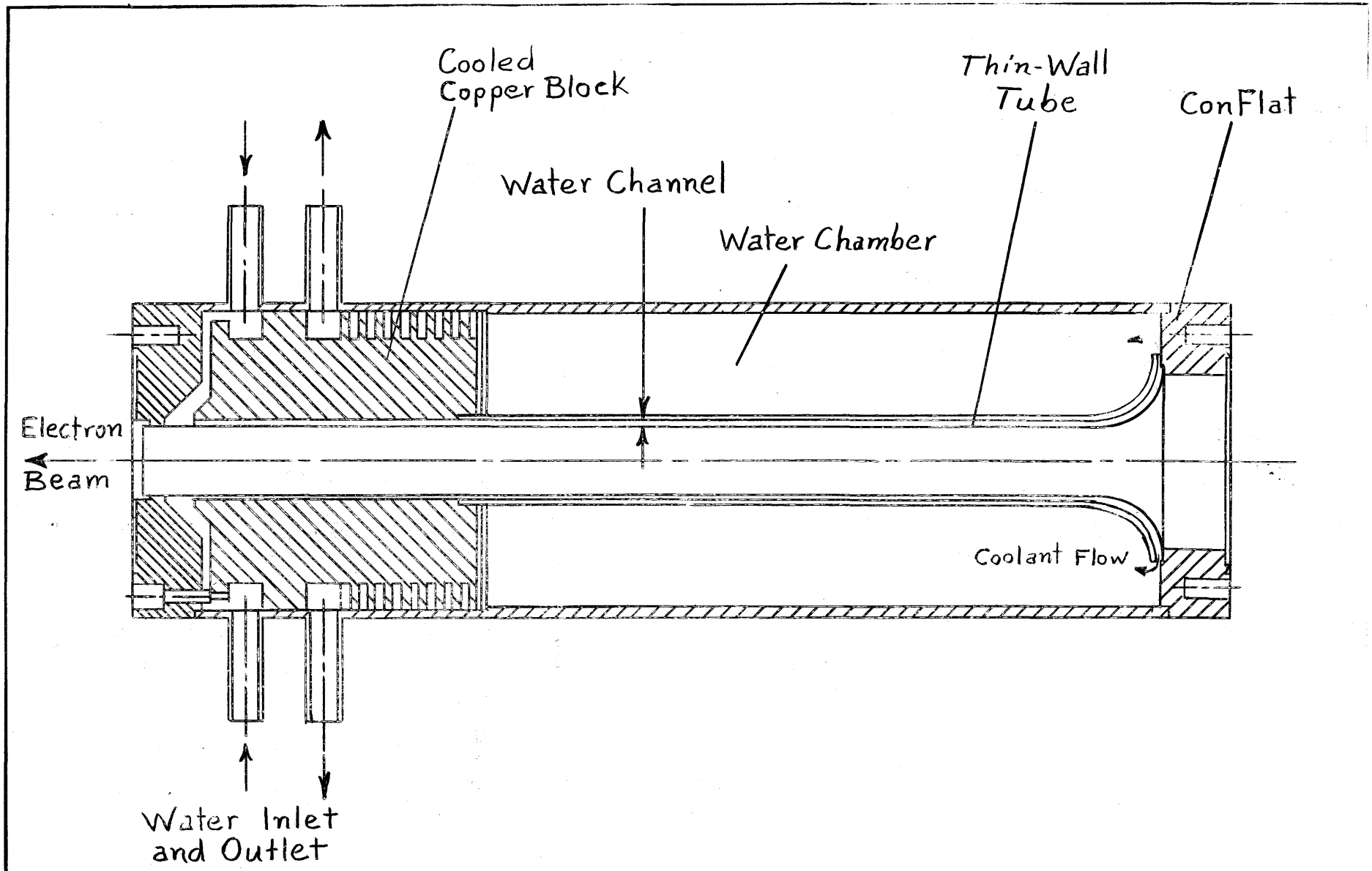

Fig. 4.4.2 Cross section of a water-cooled collimator.

connected to the drive screws and electrically connected to a bridge circuit located in the Linac control room.*

The slit jaws are fabricated from copper, chosen because it has high thermal conductivity, and to reduce corrosion problems.

Each copper jaw, shown in cross section in Fig. 4.4.3, is thick enough to scatter almost all electrons incident on it into the absorbing collimator. The remainder, in passing through the jaw, lose

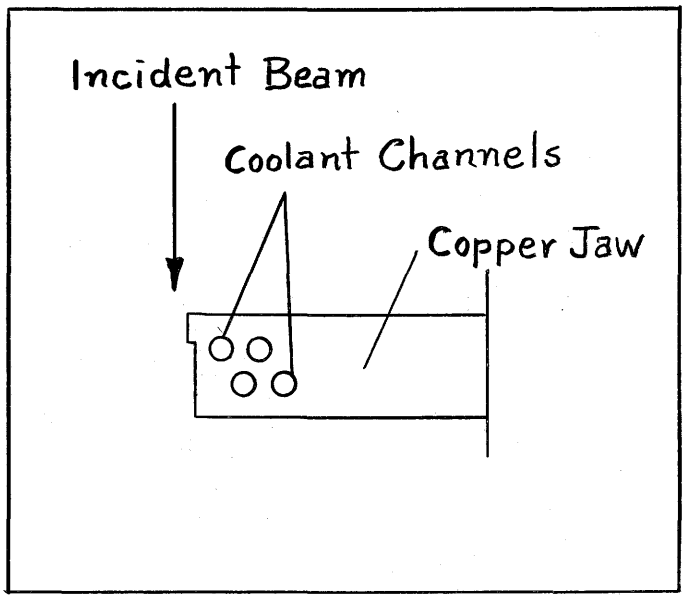

Fig. 4.4.3 Cross section of water-cooled slit jaw.

more than 2 MeV ($>$1.3% of the incident energy). It has been shown by a TRANSPORT calculation that electrons whose momenta differ from the primary momentum by $>$1% are lost to the walls in passing through the 45^{o} analyzing magnet, hence no electrons which pass

*Calibration results are given in Section 4.7.3.

through a slit jaw can reach the scatter target.

The four cooling channels, which extend from top to bottom of the slit jaw, are shown in the cross-sectional view. A water flow of two gallons/minute through these channels is adequate to remove the heat generated in the slit jaws by the highest attainable linac current. The maximum allowable current is, however, a strong function of the size of the electron beam which strikes the jaw.* To date, a conservative limit of 30 mA peak current for 1 μsec pulses has resulted in faultless operation of the slits.

4.4.4 Steering and earth-field cancelling coils

The electron beam, as it drifts between the magnetic components of the beam handling system, is deflected by the magnetic field of the earth. In addition, it may be mis-steered in passing through the magnetic components of the transport system or in passing through localized magnetic fields from pumps, metal stands, etc. Two corrective measures for these effects have been proposed:

i) To place magnetic shielding over the drift tube and to compensate for mis-steering with small electromagnets.

ii) To place current-carrying coils over long sections of the drift tube which produce both a horizontal and a vertical transverse field of up to several Gauss.

The second method has been used. In Fig. 4.4.4 we show how the coils are placed with respect to the $2\frac{1}{2}$ inch diameter transport tube.

*Details of the thermal calculations on which this design is based are given by Beer (undated).

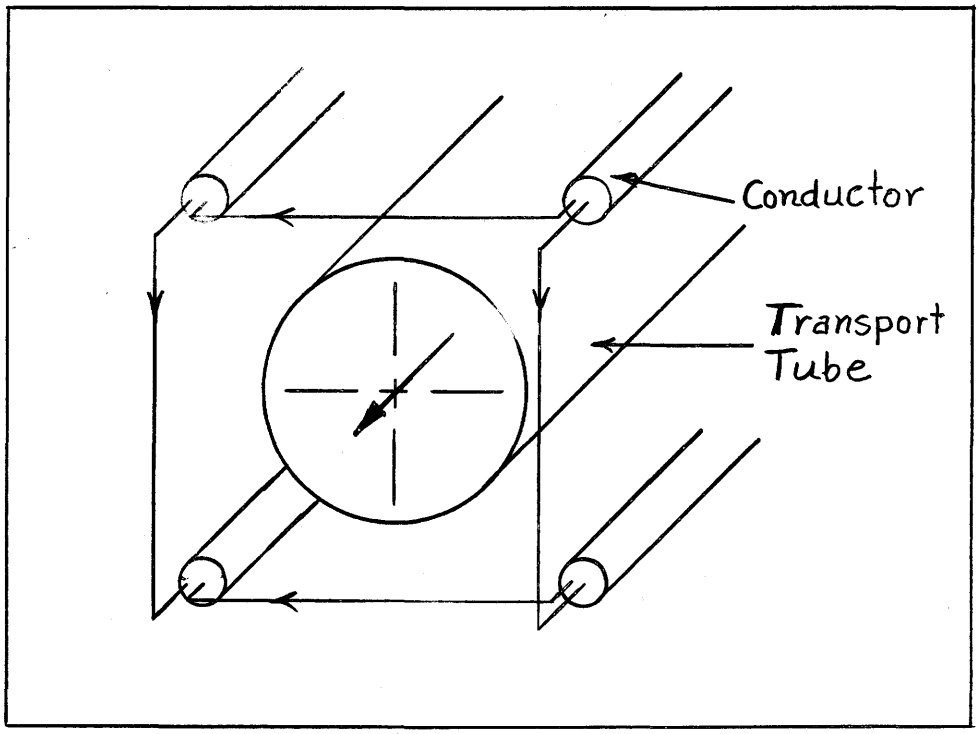

Fig. 4.4.4 Geometry of earth-field-cancelling and steering coils.

Each of the four conductors contains seven wires which are interconnected on the coil ends to form loop paths for the current. A calculation of the magnetic field distribution within coils of this geometry (Beer, 1965c) showed that the field varies less than 10% over the central 30% of the wire spacing. To achieve a uniform field region of 1 inch diameter - the size of the largest collimator - the conductors are spaced $3\frac{1}{4}$ inches apart.

4.4.5 Beam viewers and monitors

Quadrupole pair Q1 must focus the beam at the position C1.

To aid in achieving this focus, a thin one-inch-diameter disc of quartz may be moved into the beam path just in front of C1. The disc, supported by a rotatable vacuum feedthrough, is viewed by a closed-circuit television camera through a $2\frac{1}{2}$-inch-diameter quartz window.

Beam parameters also may be measured at the exit of magnet M1. A scintillation screen placed at the exit window of the magnet box is viewed by a television camera. Beyond this screen, the electron beam is stopped in an aluminum block and the current flowing to ground is monitored in the linac control room to measure both peak beam current and pulse shape.

4.5 Electron spectrometer and scatter chamber

4.5.1 General considerations

A 16-inch-radius double-focussing spectrometer* is used to momentum-analyze the electrons scattered from target nuclei. The spectrometer is a 180° magnet with the focal plane at 45° to the exit poleface. The first order focal properties of magnets such as this have been calculated by several authors. Penner (1961) gives references to these calculations, and expresses his results in a matrix formalism which was used by the author (Beer, 1965d) to make a first-order calculation of the properties of the spectrometer. The fringe fields were treated using the sharp cut-off method with the additional magnetic field path at each boundary δ given by the expression

$$\delta = 0.65d, \qquad (4.5.1)$$

*This spectrometer is on loan from the High Energy Physics Laboratory, Stanford. The magnet has been described by Sykes (undated).

where d is the average poleface gap.

The scatter target to magnet distance was optimized on the basis of:

i) The maximum scattering angle θ (see Fig. 4.5.1), kept as large as possible to enhance the transverse terms in the electron scattering cross section (Eq. 2.4.1).

ii) The position of the electron detector in relation to the magnet, kept large to avoid mechanical constrictions.

The physical size of the spectrometer places a limitation on the maximum scattering angle. Since the input beam tube diameter is fixed at $2\frac{1}{2}$ inches, the maximum angle may be related to the target-to-magnet distance T. This distance also is related to the distance D of the detector from the other magnet face. Beer (1965d) gives the expression

$$D = - 0.70\ T + 18, \qquad (4.5.2)$$

where both T and D are expressed in inches. The detector must be at least 4 inches from the face to avoid interference with magnet current coils, hence the target-to-magnet distance must not exceed 20 inches. We find that

$$\text{for } T = 20 \text{ inches}, \quad \theta_{max} = 148^{o}.$$

The scattering angle can be increased if some iron is cut off the magnet. In this case

$$\text{for } T = 20 \text{ inches}, \quad \theta_{max} = 155.1^{o}$$

$$\text{or, for } T = 18 \text{ inches}, \quad \theta_{max} = 152^{o}.$$

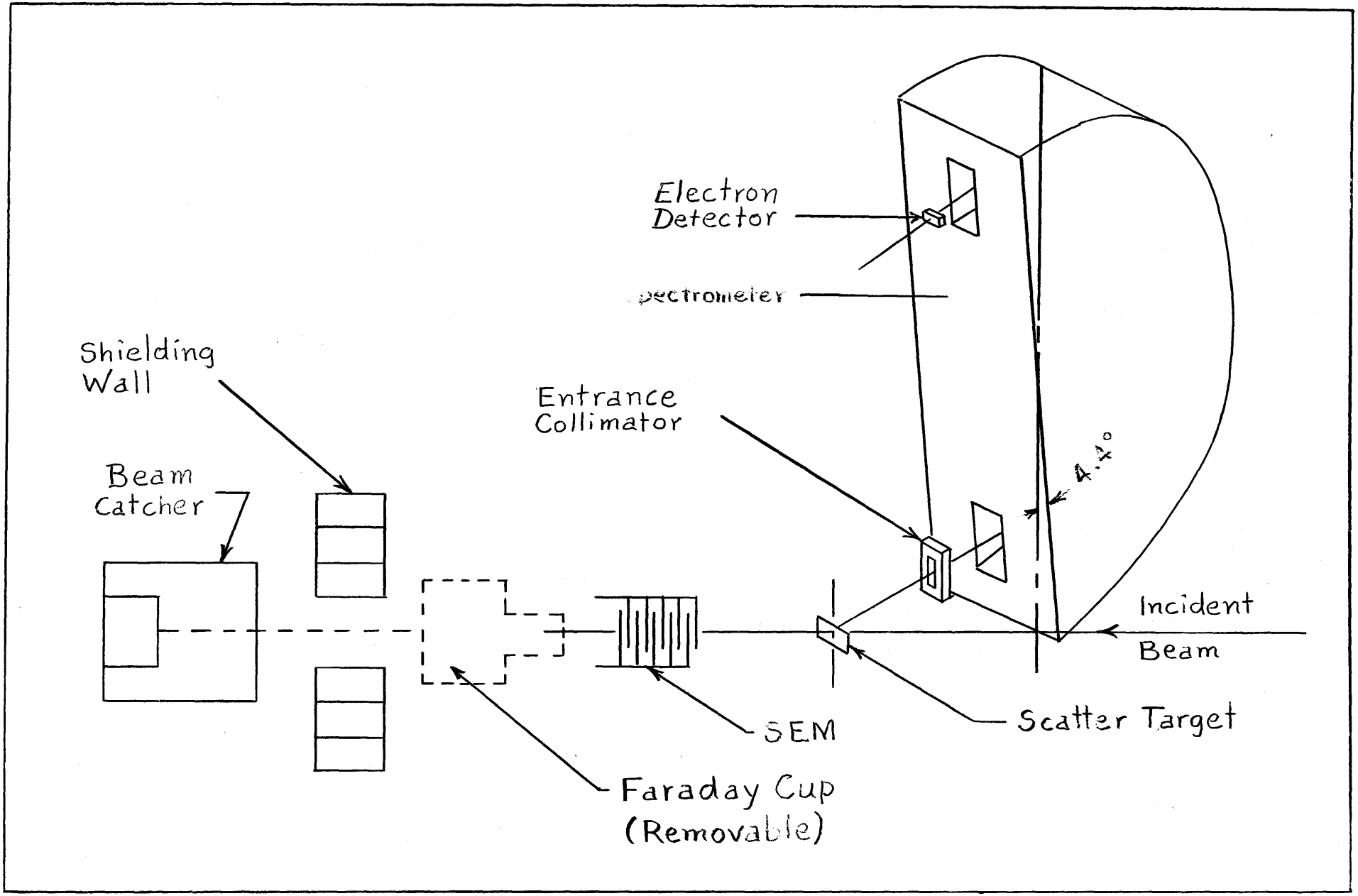

Fig. 4.5.1 Essential components of the electron scatter facility.

We have chosen the second method, with design values

$$T = 19.6 \text{ inches, and } \theta_{max} = 155^{\circ}. \qquad (4.5.3)$$

This places the detector slightly more than 4 inches from the magnet.

In determining T, the solid angle of the spectrometer was not considered. With T = 19.6 inches, the solid angle of acceptance is ~5 millisteradians. This value was reduced to ~3 millisteradians by an entrance collimator.

With T = 19.6 inches Beer (1965d) calculated the magnification and the dispersion of the spectrometer.

$$\text{(Magnification)} = 0.785, \qquad (4.5.4)$$

$$\text{(Dispersion)} = 14.5 \text{ mm/percent}.$$

The first-order calculation of detector position was sufficiently accurate for design of the facility. However, to obtain maximum resolution with the system an experimental measurement of the exact detector position was made. The α-particle technique of Sykes (undated) was used. The measurement is discussed further in Section 4.5.5.

4.5.2 Scatter chamber

The scatter chamber, shown in plan view in Fig. 4.5.2 and side elevation in Fig. 4.5.3, contains a precisely-positioned remotely-controlled scatter target holder. The chamber has nine covered ports at well-defined scattering angles ($\pm$1/6 degree). The spectrometer may be coupled directly to any of these ports with a flexible vacuum coupling, thereby eliminating the need for a vacuum window which would cause a loss in resolution. Thus the

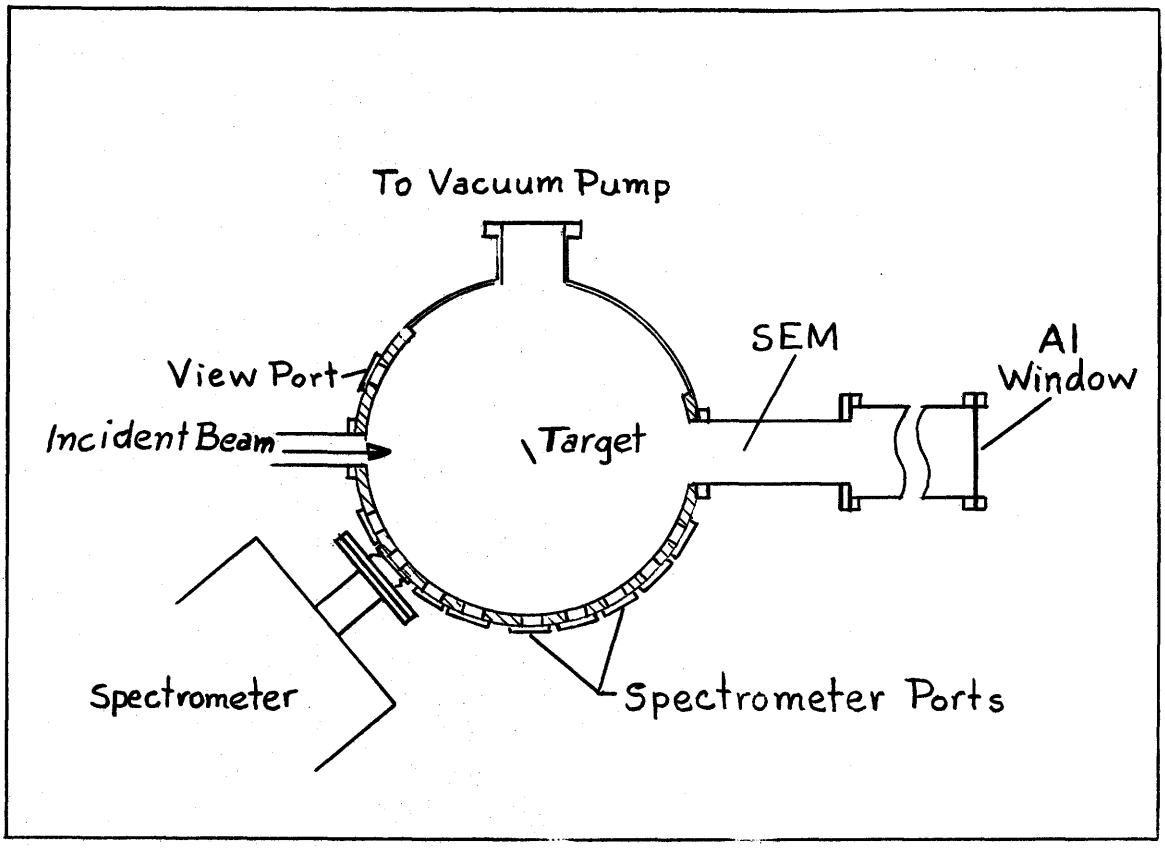

Fig. 4.5.2 Plan view of scatter chamber.

chamber and the magnet box both are pumped by the 360 l/sec. oil diffusion pump connected to the 5 inch diameter side port.*

The diameter of the chamber was made as large as possible within the limits of the target-to-magnet distance. One lucite-covered port is provided through which a closed-circuit television camera views the scatter target. A 4-foot drift tube was put between the chamber and the 0.009 inch aluminum beam exit window to reduce background at the detectors. This tube also contains the secondary emission monitor described in Section 4.6.2.

*Beer (1964a) shows that with a surface outgassing rate of 10^{-7} Torr-litres/sec-cm^2, the chamber and magnet box will pump to $\sim 10^{-5}$ Torr.

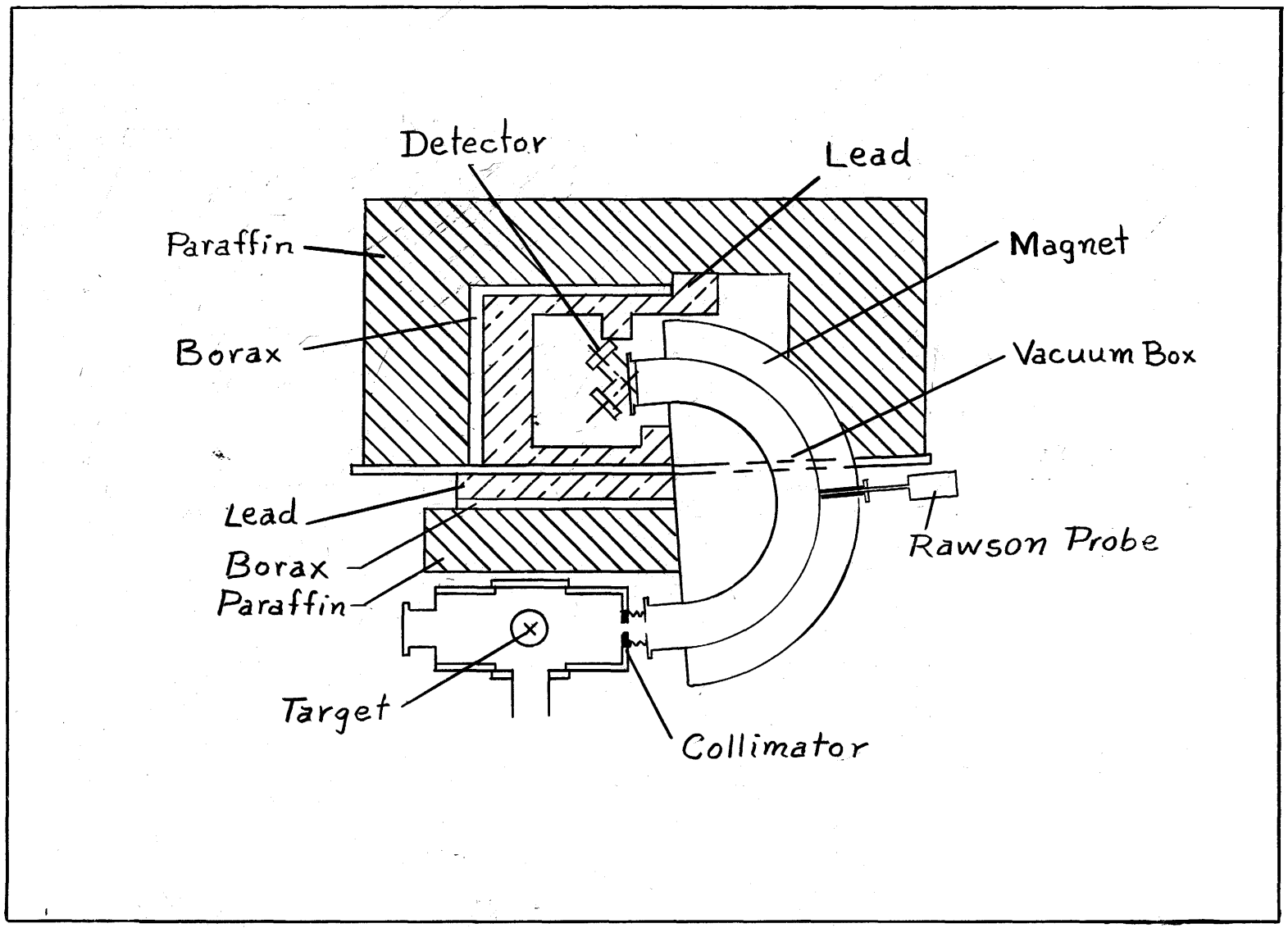

Fig. 4.5.3 Cross section of spectrometer showing target, scatter chamber and detectors.

4.5.3 Spectrometer magnet and power supply

Technical specifications of both the electron spectrometer and its current-regulated power supply were given by Sykes (undated). Since then some changes have been made. The brass vacuum chamber has been replaced by a stainless steel one. Eight hardened steel bolts centrally located on the polefaces of the magnet were replaced by flush soft iron screws. In previous work, the magnet current was used to determine the magnetic field within the spectrometer. For the present work, a Rawson-Lush Model 921 rotating coil Gaussmeter was used to measure continuously the magnetic field, thereby eliminating uncertainty due to bulk temperature effects within the magnet and to hysteresis. In addition to these changes in the magnet, the short- and long-term stability of the magnet power supply were improved radically. Stability figures for the present system are given in Section 4.5.4.

The spectrometer is mounted vertically on the rotating platform of a naval gun mount capable of supporting the weight of the spectrometer and the detector shielding. Its position with respect to the scatter target and chamber is shown in Fig. 4.5.3. To allow for the effect of the lower fringe field the magnet has been tipped 4.4° as shown in the figure.

A precise knowledge of the scattering angle θ is required in analyzing electron scattering experiments. To achieve this, the following alignment procedure was adopted*:

---

*Detailed alignment notes are given by Beer (1964a) and (1965a).

i) The gun mount platform was precisely levelled.

ii) The rotation axis of the gun mount was located to within $\pm$0.010 inch, and this axis was set on the beam axis to within 1/64 inch. During this adjustment, the distance from the axis to magnet M2 was set to the design value within $\pm$1/8 inch.

iii) The scatter chamber was placed at the correct elevation, levelled and centred with respect to the rotation axis of the gun mount to an accuracy of $\pm$0.010 inch.

iv) The centres of the beam inlet and outlet ports of the scatter chamber were positioned on the beam axis within $\pm$1/64 inch.

v) The target holder axis was placed on the rotation axis within $\pm$0.020 inches.

vi) The side faces of the spectrometer were set vertical to within $\pm 0.3^{\circ}$.

vii) The spectrometer was tipped to $4.4^{\circ} \pm 0.05^{\circ}$ and moved to a position in which the perpendicular from the centre of the front face bisected the rotation axis within $\pm$0.020 inches.

viii) The target to magnet distance was set to 19.60 $\pm$ 0.02 inches.

ix) An angle-positioning-and-locking mechanism was calibrated to set the spectrometer to each of the scattering ports on the scatter chamber to an accuracy of $\pm 0.05^{\circ}$.

4.5.4 Magnetic field measurements

The precise determination of excitation energy requires well resolved elastic and inelastic peaks. To achieve good resolution, the magnetic field of the spectrometer must be stable. Operating experience has shown that an instability of ± 0.2 Gauss is rarely exceeded. This corresponds to better than $\pm 0.01\%$ for the ^{12}C measurements.

The Gaussmeter probe is mounted permanently at a point where it does not intercept particles within the spectrometer. The probe location is marked on Fig. 4.5.4 which shows three radial distributions of magnetic field measured at differing magnet currents. It is the centreline field which is used to determine the scattered electron energy. Hence the factor relating centreline field to that measured at the fixed position was measured over a wide range of magnet currents. A small hysteresis effect at low field values ($\pm 0.1\%$) was ignored in plotting Fig. 4.5.5. By treating the factor as an analytic function of the Rawson reading, a least-squares fit of an nth order polynomial to the data gave the following results:

Optimum degree: $n = 7$.

Coefficients:

$n = 0$	:	1.200
1	:	3.177×10^{-5}
2	:	-8.572×10^{-9}
3	:	-5.667×10^{-13}
4	:	$+7.707 \times 10^{-16}$
5	:	-1.572×10^{-19}
6	:	$+1.373 \times 10^{-23}$
7	:	-4.514×10^{-28}.

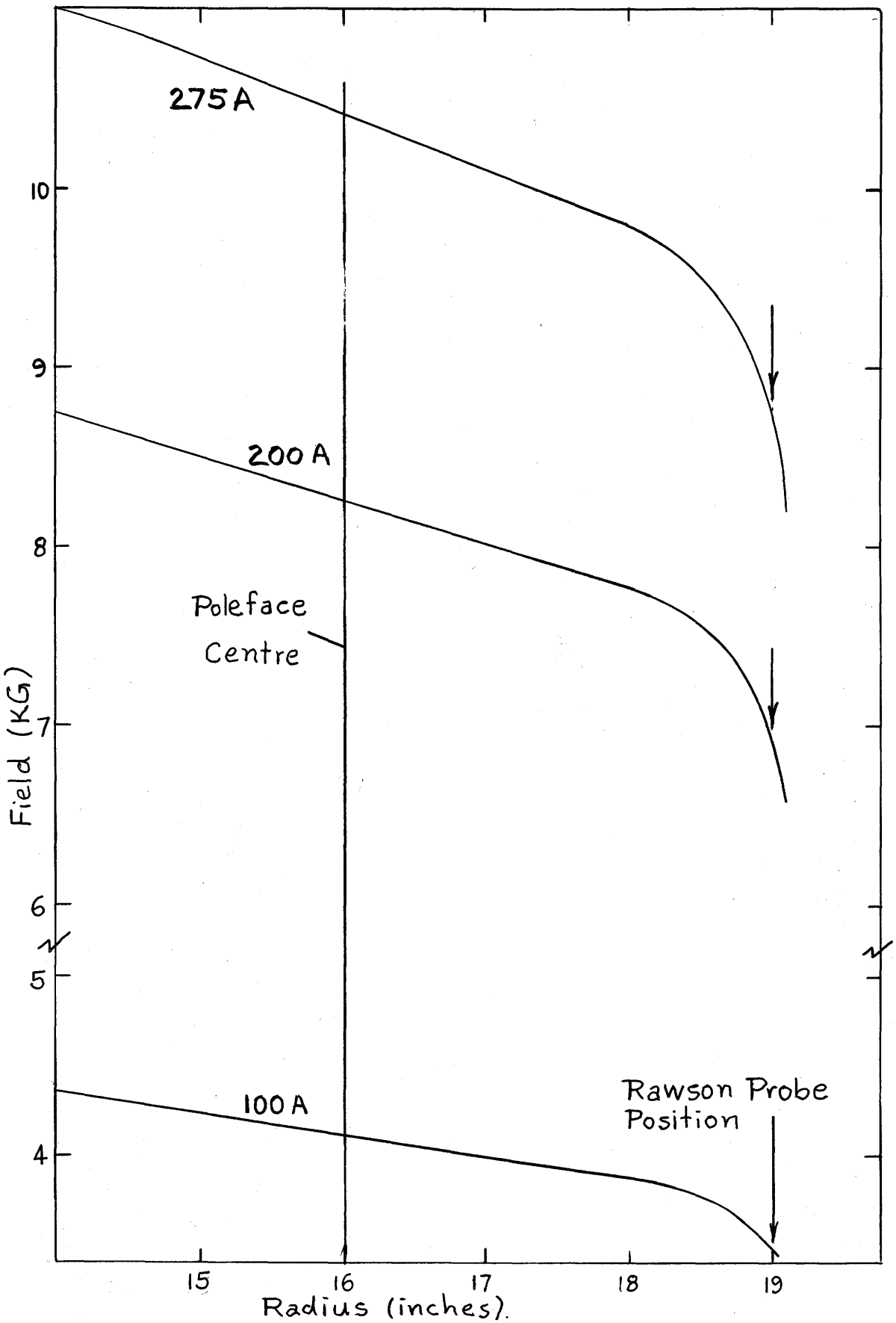

Fig. 4.5.4 Radial distribution of magnetic field in the spectrometer.

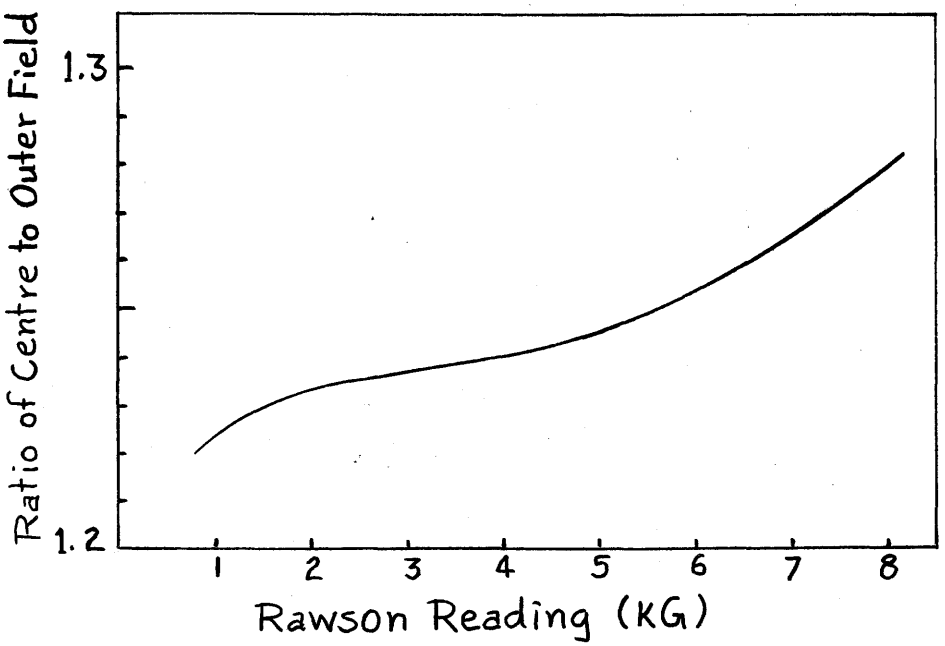

Fig. 4.5.5 Factor relating centreline field to edge field in the spectrometer.

Standard error: 1.2×10^{-4}.

This functional form has been programmed, and during an experiment a computer is used to determine the electron energy corresponding to a particular Rawson reading. Other spectrometer parameters which relate centreline Gauss to energy are given in Appendix B..

4.5.5 Test of spectrometer using α-particles

Prior to using the spectrometer to analyze scattered electrons, the electron scattering facility was checked using an α-source mounted on the scatter target holder. The technique of

this measurement was given by Sykes (undated). Two experimental parameters were obtained:

i) The location of a point on the focal plane.

ii) An upper limit on the resolution of the spectrometer with the detector correctly placed.

Details of the measurements summarized in this section are given by Hütcheon and Beer (1965). The equipment used was essentially that of Sykes (undated) with some modifications made to reduce noise in the electronics. All measurements were made with a 2 μCurie ^{241}Am α-source. Initial measurements were made without an entrance collimator. However, results obtained with the collimator were used to locate the detector and measure the resolution.

For the most satisfactory operation the detector must be located on the optical axis of the spectrometer. Sykes (undated) calculated the axis location for an input angle of 4.8^{o}. The spectrometer is now set at 4.4^{o}, thus a small correction was applied to his result to obtain the position of the optical axis at the detector location.

The measured detector position as given by Hutcheon and Beer (1965) may be expressed as a distance D from the magnet face. They give

$$D = 4.33 \pm 0.15 \text{ inches}, \qquad (4.5.5)$$

with the detector 0.18 ± 0.02 inches below the flange centreline.

The resolution of the system, measured with 0.016 inch slits on both the source and the detector, was 0.065% full-width-at-half-height of the α-distribution. This value is considerably better than that

corresponding to the present electron detector size.

4.5.6 Ne 102 electron detector and electronics

We have shown that the spectrometer has a resolution of ~0.07%. However, the inelastic count rate would be too low if a single detector with this resolution were used. Thus we have mounted a detector on the focal plane which accepts a momentum bite of 0.28%. The detector with associated electronics is described below. Overall performance of the system is given in Section 4.7.5.

Three electron detectors of roughly equivalent design have been constructed for use with the spectrometer. However, experience has resulted in improvements, hence we describe in detail only the most recently constructed detector, MK3, which was used for the carbon measurements reported in this thesis.

The detector is a scintillation counter telescope employing two Ne 102 plastic scintillators coupled by lucite light pipes* to Philips XP1110 photomultiplier tubes. The position of the scintillators is shown with respect to the vacuum flange of the spectrometer magnet box in Fig. 4.5.6. The small front scintillator is 0.200 inches thick, 0.158 inches wide and 0.67 inches long. It is press-fitted into a slot in a 0.25 inch thick polished lucite light pipe which in turn is fastened to the photomultiplier with Sylgard 182 potting resin†. The back scintillator, also 0.200

*The technique of light coupling the front Ne 102 detector to the photomultiplier follows closely that outlined by Gibson (1964).

†Manufactured by Dow Corning Corp., Hemlock, Michigan.

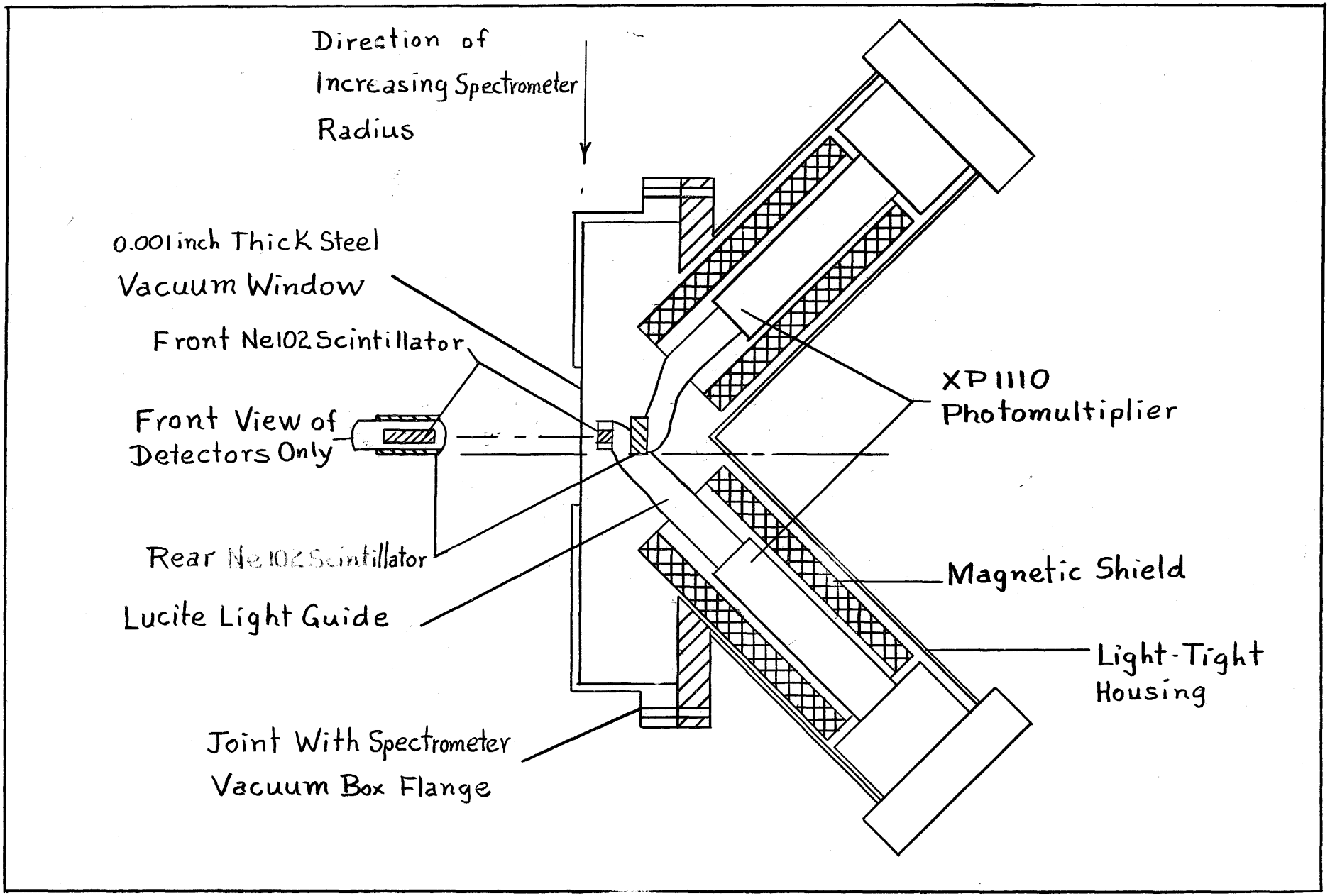

Fig. 4.5.6 Mechanical details of the Ne 102 electron detector.

inches thick, is larger in cross section to allow for multiple scattering of electrons which traverse the front counter. It is fastened with Sylgard to a shaped 3/8 inch diameter lucite rod coupled to the second photomultiplier. The back counter and light pipe are wrapped with 0.00025 inch thick aluminum foil to prevent light from one scintillator affecting the signal from the other. Both photomultiplier tubes are encased in cylindrical Netic and Co-netic* magnetic shields as shown in Fig. 4.5.6.

The scintillators and photomultipliers are located within a light-tight container, the front face of which forms a vacuum seal to the upper flange of the spectrometer magnet chamber. On this front face a $1\frac{1}{2}$-inch-diameter 0.001-inch-thick stainless steel foil provides the vacuum seal without causing a significant loss in resolution due to multiple scattering.

The parameters of two other detectors, MK1 and MK2, used for preliminary measurements, are compared with those of MK3 in Table 4.5.1.

---

*Manufactured by Perfection Mica Co., Chicago, Illinois.

Table 4.5.1

Details of Ne 102 detectors

	MK1	MK2	MK3
Photomultipliers	150 AVP	150 AVP	XP1110
Front Ne 102 detector width	0.08 inch	0.16 inch	0.16 inch
Front and back Ne 102 thickness	0.10 inch	0.10 inch	0.20 inch
Lucite light pipe thickness (Front Det.)	1/8 inch	1/8 inch	1/4 inch
Back detector light pipe	1/8 inch sheet	3/8 inch rod	3/8 inch rod
Photomultiplier magnetic shielding			
Shape	cylinder	cylinder ends crimped	cylinder
Length	4 inches	$4\frac{1}{2}$ inches	$4\frac{1}{2}$ inches
Inside diameter	$1\frac{1}{2}$ inches	$1\frac{1}{2}$ inches	3/4 inches
Outside diameter	1 7/8 inches	1 7/8 inches	1 7/8 inches

A block diagram of the electronic components of the detector is shown in Fig. 4.5.7. Pulse signals from the anode of each photomultiplier are amplified by Hewlett-Packard model 462A Wideband Amplifiers* (marked F1 and F2 on the diagram), while signals from the last dynode are stretched to $\sim 1\ \mu$sec and are amplified by linear amplifiers marked S1 and S2†. The four signals are carried on RG58/U coaxial cable to the data collection console. Here the

*Hewlett-Packard Co., Loveland, Col.

†These amplifiers as well as two marked S3 and S4 were designed and constructed by T. Drake, and will be described at a later date.

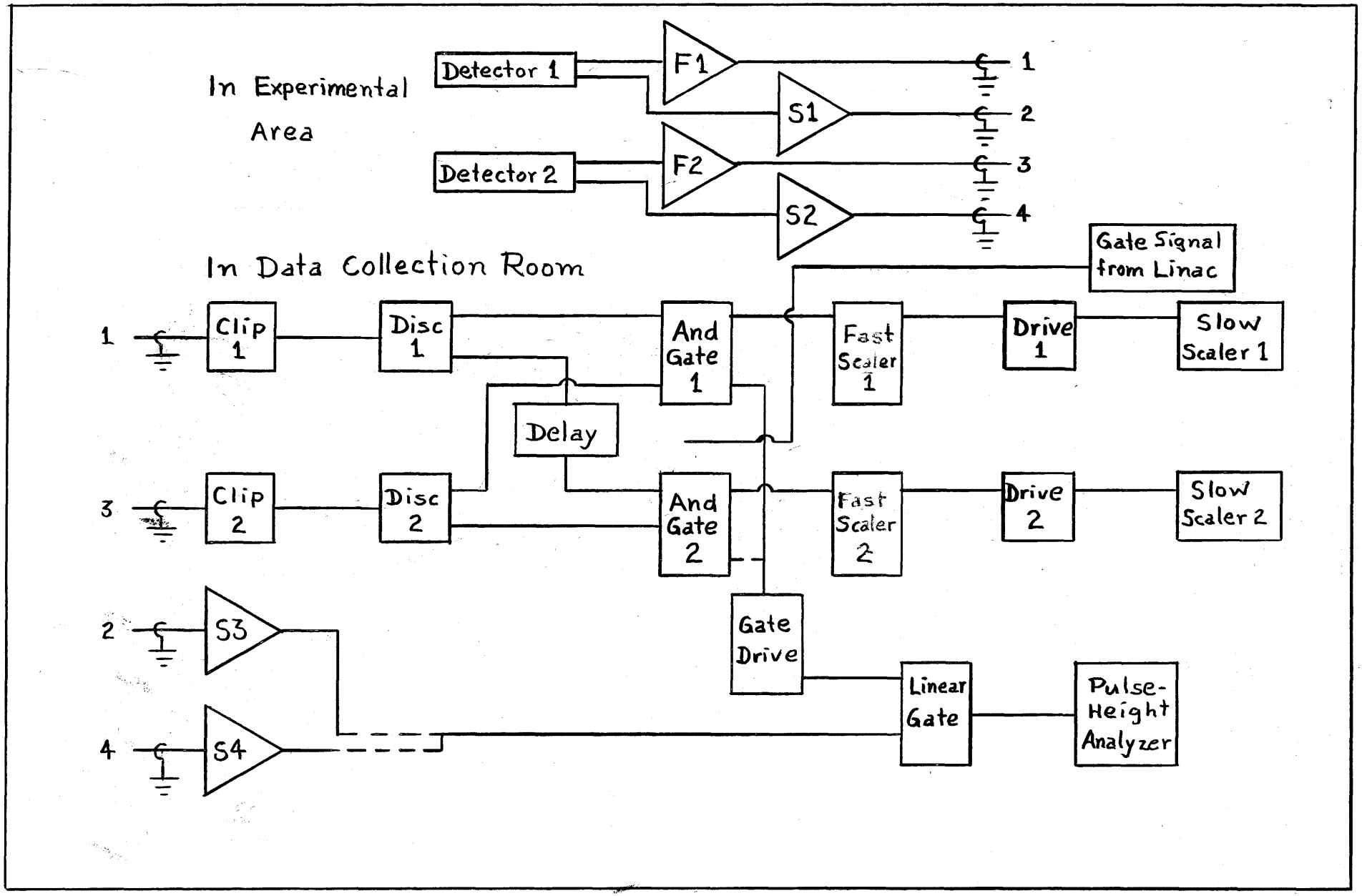

Fig. 4.5.7 Block diagram of the detector electronics.

two slow signals are further amplified by units marked S3 and S4, and one output is fed through an EG and G "Linear Gate"* (Model LG100) to a kicksorter to obtain a pulse height spectrum. The two fast signals are clipped to ~5 nsec and are fed to the inputs of an EG and G "Dual Trigger" (Model TR 1045), labelled Disc 1 and Disc 2. The outputs of these triggers are counted either in coincidence or in delayed coincidence by EG and G Fast Scalers (Model S100) which overflow into slow scalers. The coincidence count includes some random coincidences. The number of random coincidences may be estimated from the delayed coincidence count. One output from the coincidence unit (EG and G Model C102A) opens the gate in the slow circuit. A pulse from the accelerator timing circuit opens both triggers for ~1 μsec at the time of each linac beam burst. The coincidence resolving time of the system is 7.5 nsec; the delay in the delayed coincidence circuit was set at 8 nsec.

4.5.7 Detector shielding

The primary electron beam produces secondary electrons, gammas and heavy particles when it strikes materials in the scatter room. These in turn give rise to spurious output counts from the detector, referred to as background. To reduce the background, the Ne 102 detector and photomultiplier assembly is located inside a shielding box shown in cross section in Fig. 4.5.3. The shield is designed to attenuate gammas, electrons and heavy particles

*Edgerton, Germeshausen and Grier, Inc., Boston, Massachusetts.

(including high energy neutrons). Dodge and Barber (1962) have shown that neutrons are a primary cause of background in hydrogen-containing scintillators such as Ne 102.

The shielding is located on a steel platform bolted to the gun mount which supports the spectrometer. The outer layer of paraffin slows neutrons which are then absorbed by 3/4-inch-thick borax sheets placed on five of the six sides of a cube surrounding the detectors. Inside the borax sheets, an eight inch layer of lead bricks attenuates gammas (some of which result from neutron capture in boron), as well as electrons and heavy particles. (Some deviations from this construction resulted from the presence of magnet coils, cooling lines, etc.)

4.6 Electron beam current monitors

4.6.1 Faraday cup

The laboratory standard for measurement of beam current is a vacuum Faraday cup, shown in cross section in Fig. 4.6.1.

The design of Faraday cups for use as electron beam current monitors has been treated by several authors, e.g. Isabelle (1962), and Brown and Tautfest (1956). These authors discuss the basic processes involved in stopping a high energy electron beam. The author has made detailed design calculations for a multi-purpose Faraday cup capable of stopping a high power ($\sim$30 kW) beam yet suitable for precise measurement of the energy-analyzed beam (Beer (1964c)). We give a summary of the design for the cup and an outline of the factors which affect its performance and accuracy.

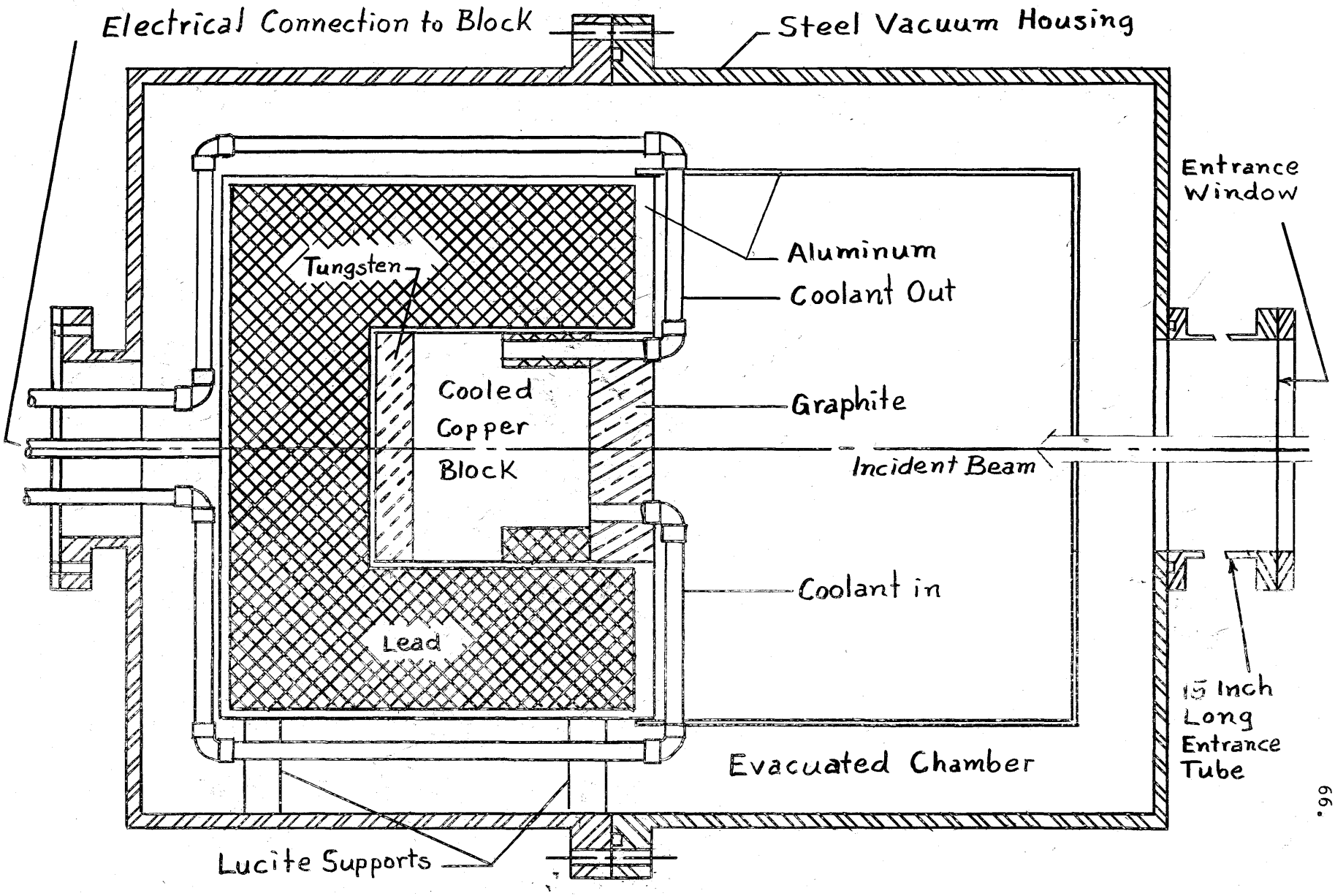

Fig. 4.6.1 Cross section of Faraday cup.

The total thickness of the primary stopping block, ~35 radiation lengths, was based on measurements made by Isabelle (1962) with 500 MeV electrons, and by Kantz and Hofstadter (1954) with 185 MeV electrons. They show that thirty-five radiation lengths of lead will stop 99.9% of the incident charge in a 250 MeV electron beam. We use a block made from a combination of lead, tungsten, and copper since lead alone cannot be cooled adequately. About 95% of the incident beam power is absorbed by a cooled cylinder of copper placed at the front face of the stopping block. Copper was chosen for the following reasons:

i) It is a dense, high Z material.

ii) The high thermal conductivity and melting point of copper permit a reasonable cooling geometry to be used.

iii) Corrosion is reduced.

iv) The power deposit of electrons in copper is known from the measurements of Kantz and Hofstadter (1954).

The cooling channels in the copper block are capable of removing up to 30 kW when 5 gallons per minute of de-ionized water flows in them. A flow of compressed air is sufficient for a beam power of about 1500 W. No cooling was required during the low-beam-power measurements described in this thesis. Almost all the beam power remaining after traversing the copper is deposited in a one-inch-thick tungsten disc, placed in thermal contact with the back face of the copper block.

The diameter of the lead cylinder surrounding the copper and tungsten was optimized using the following empirical relation derived from the measurements of Kantz and Hofstadter (1954)

$$r = 3/4\ d, \qquad (4.6.1)$$

where r is the optimum radius for a stopping cylinder of length d. The optimum cup radius derived from this formula was increased by 0.7 inches to 7.5 inches to allow for the finite size of the electron beam which strikes the front surface.

A 1/8 inch thick outer layer of aluminum was put on the block since measurements by Isabelle (1962) show that it reduces charge loss from a lead block by a factor of four.

Kretschko et al (1962) and Isabelle (1962) have made measurements on back scattered and secondary electrons emitted from the front surface of a stopping block.* Isabelle (1962) found that for a primary electron energy of 450 MeV, between 3 and 4% of the incident current is scattered in the backward direction. Almost all of these electrons were found to have an energy < 500 eV. Pohlit (undated) has measured the backscatter coefficient for electrons incident on lead, antimony, copper, iron, aluminum and carbon. Carbon was found to have the lowest coefficient ($< 0.5\%$ for $E > 20$ MeV), thus the fraction of electrons backscattered from the front surface of the cup is reduced by placing a 2-inch-thick graphite disc in front of

*The author is indebted to Dr. J.S. Pruitt for clarifying the definitions of these two processes when applied to the design of Faraday cups. Back scattered electrons are incident high energy electrons which have undergone large angle scattering. Secondary electrons are the low energy products of ionization.

the cooled copper block. Of the electrons which are backscattered by the graphite, most are stopped in a 1/8 inch thick aluminum chamber electrically connected to the front face of the cup. The beam entrance hole in this chamber subtends only 2% of the backscatter solid angle, thus for an isotropic distribution of backscattered electrons 98% of the low energy ones are collected by the stopping block.

The block was placed in an evacuated chamber to reduce ion production by the incident beam. For the present design it may be shown that the number of ion pairs produced within the chamber per incident electron is reduced to $\sim 10^{-2}$ at a pressure of 10^{-4} Torr. However, very few of these ions are collected on the block.

The thin window through which the beam enters the vacuum chamber gives rise to secondary electrons of low energy which are swept to the walls by a transverse magnetic field.

The current signal from the cup is transmitted through RG9/U cable to an Elcor current integrator.

4.6.2 Secondary emission monitor

A secondary emission monitor (SEM) with 10 emitting surfaces is used to measure incident electron current during an experimental run. The unit, shown in cross section in Fig. 4.6.2, is fabricated from eleven 0.00025 inch thick aluminum foils placed in physical contact with aluminum rings electrically connected as shown on the diagram. Lucite discs are used to insulate each foil from other foils and from the containing tube. The assembly, held together with nylon screws, is located within the vacuum of the

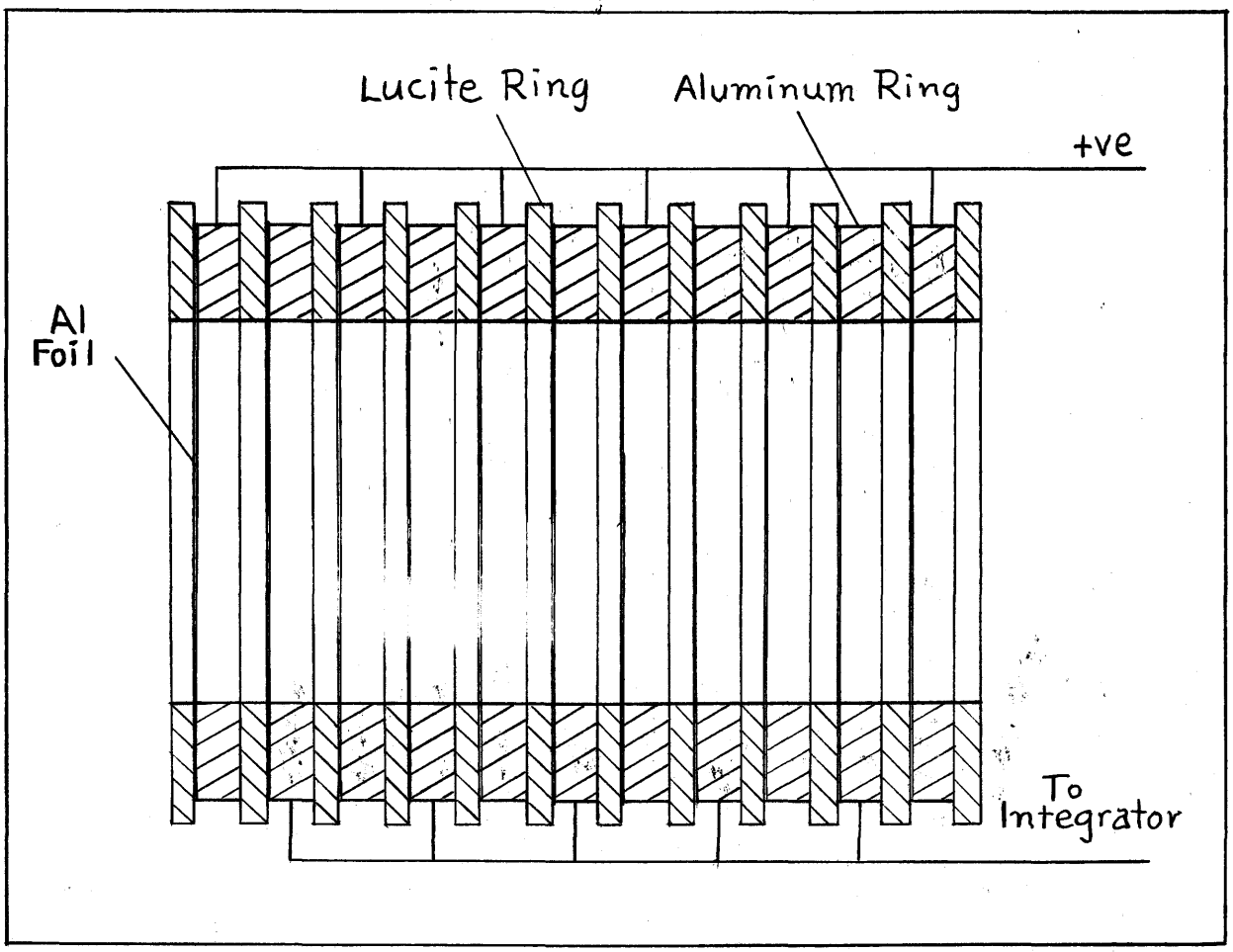

Fig. 4.6.2 Cross section of the secondary emission monitor.

scatter chamber. The collecting foils are attached to a +130 volt bias supply with RG9/U coaxial cable which also connects the unit to a current integrator.

4.6.3 Elcor current integrators

Two Model A309B Elcor integrators* are used to integrate current signals from the Faraday cup and the SEM. They have the following manufacturers specifications:

*Elcor, 1225 W. Broad St., Falls Church, Virginia.

Input current for full-scale meter deflection:	1×10^{-3} to 3×10^{-9} Amp in 12 steps
Accuracy:	1%
Reproducibility:	0.2%
Maximum drift:	0.01% per hour

To obtain these operating parameters, the minimum recommended source impedance is:

$$R_{min} = \frac{1}{\text{(Numerical value of the full-scale current)}} . \qquad (4.6.2)$$

The measured impedance of the Faraday cup is $\sim$500 MΩ, hence there is no restriction on the minimum full-scale current setting which may be used for absolute current measurements.

4.6.4 Lucite Čerenkov counter in the scatter room

To insure that the detector gate is correctly timed with respect to the electron beam pulse, a qualitative measurement of the pulse shape of the beam bursts in the scatter room is derived from a Čerenkov counter. The counter is a 2-inch-diameter, 2-inch-long lucite cylinder viewed by a Philips 150 AVP photomultiplier. The anode signal from the photomultiplier may be compared with the gate signal.

4.7 Performance data on experimental equipment

4.7.1 Beam analyzing magnets

Magnetic field measurements of the analyzing magnets M1 and M2, made by Hutcheon and Ku (1965), are summarized in Table 4.7.1.

Table 4.7.1

Magnetic properties of the analyzing magnets

Field stability (after 10 hr. warmup):	$\pm$0.005%
Temperature coefficient of field (based on magnet poleface temperature):	0.15 Gauss/^{o}C
Field reproducibility (based on the voltage reading across the power supply resistor):	$\pm$ 1 part in 10^3
Residual field after degauss cycle:	4 Gauss
Field difference between M1 and M2:	4 Gauss

The voltage V across a series resistor in the current supply circuit is used to determine the magnetic field B in the magnets. The linear relation between these quantities is

$$B = 4.320\ V + 8 \times 10^{-2}, \qquad (4.7.1)$$

where B is in kilogauss, and V in volts. The manufacturer gives the value 4.38 kG/100 MeV for magnets M1 and M2, hence

$$\mathcal{E}_1 = 98.7\ V + 1.83, \qquad (4.7.2)$$

where $\mathcal{E}_1$ is the energy in MeV of the transmitted electrons.

4.7.2 Vacuum components

Following an initial clean-up period, the vacuum system has operated satisfactorily at a pump pressure of less than 10^{-7} Torr. Component assembly using ConFlat joints has resulted in no detectable leaks.

The induced activity in components within the system rises to give a dose rate of several R/hour on contact following prolonged use at a beam power of $\sim$1 kW. Over a six month operating period no

failures have occurred other than radiation darkening of a quartz window.

4.7.3 Adjustable slits

Four sets of adjustable slits described in Section 4.4.3 have been measured to correlate jaw separation with the reading of the remote position indicator. Each set of data, least-squares-fitted by a polynomial of arbitrary degree, resulted in a linear best fit with a standard error of <0.006. The jaw separation is reproducible to ± 0.002 inch.

4.7.4 Secondary emission monitor

Both the efficiency of the secondary emission monitor and its stability have been measured with respect to the Faraday cup at two extreme energies. The results are given in Table 4.7.2.

Table 4.7.2

Measured SEM efficiency

Energy (MeV)	Time from start (hours)	Efficiency	Average Efficiency	Deviation from Average (%)
64	0	0.1755		+1.15
	$6\frac{1}{2}$	0.1734		-0.06
	9	0.1729	0.1735	-0.35
	14	0.1731		-0.23
	17	0.1725		-0.58
127	0	0.1795		0
	4	0.1797	0.1795	+0.11
	$10\frac{1}{2}$	0.1792		-0.17

The ratio of the average efficiency at 127 MeV to that at 64 MeV is 1.035. Isabelle (1962) quotes efficiencies for aluminum foil secondary emission monitors. His results for these energies give a ratio of 1.05, in good agreement with our measurement.

4.7.5 Pulse height spectra from the Ne 102 electron detectors

Pulse height spectra obtained with the detectors and the electronic components described in Section 4.5.6 are given in Fig. 4.7.1. These spectra show that the pulse height distribution from

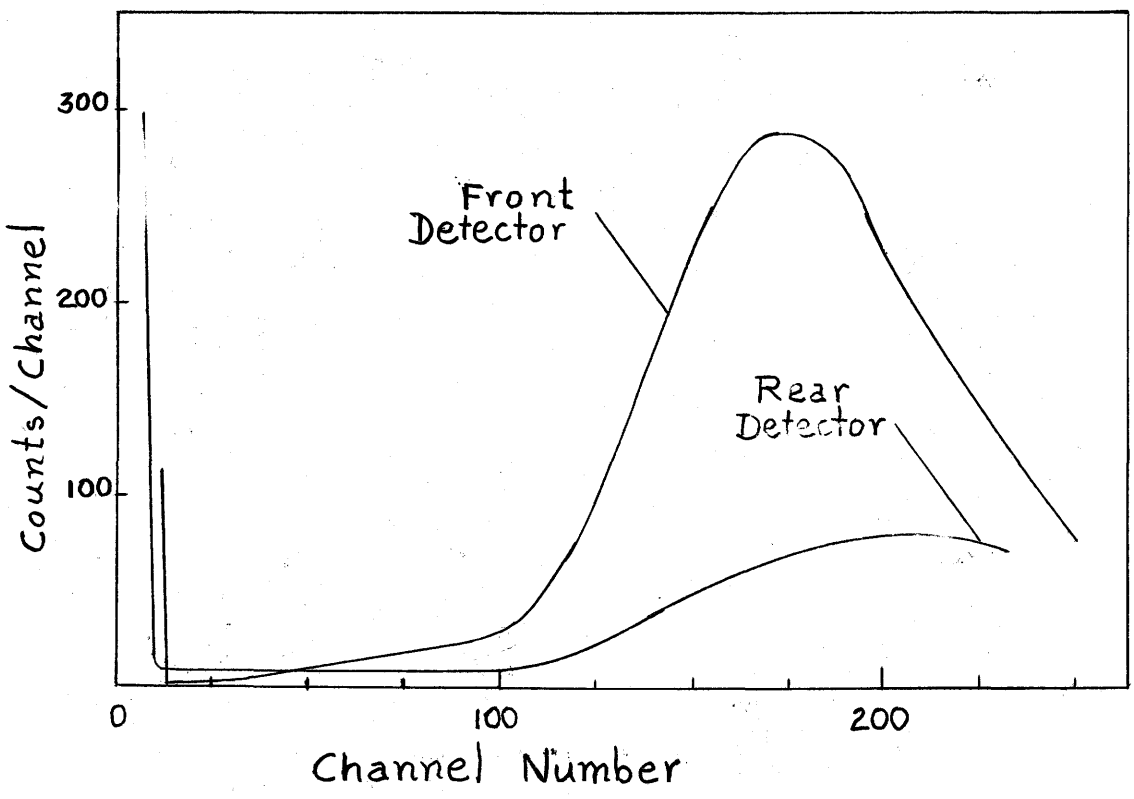

Fig. 4.7.1 Pulse height distributions from front and rear Ne 102 electron detectors.

electrons traversing both the front and the rear scintillator is well above photomultiplier noise.

4.7.6 Overall performance of the energy analyzing system

The energy analyzing system has been operated over a range of electron energies from 49 MeV to 127 MeV. At all energies the beam spot at the scatter target was less than 0.3 cm high and 1.2 cm wide with no detectable penumbra. With quadrupole pair Q3 set to image the entrance slits C1 on the scatter target, a horizontal and vertical spot stability of $\pm$0.1 cm has been achieved.

Varying the current in steering coils 1 and 2 does not change the observed beam spot shape at the exit of magnet M1.

Only one component in the analyzing system required relocation after optical alignment. Magnet M2 was moved laterally 0.19 inches to correct for an observed displacement of the beam at the scatter target of $\sim$ 3 inches.

To investigate further the properties of the electron beam at the scatter target we have used the technique of elastic electron scattering from thin targets. Such measurements give precise information on the energy distribution within the beam. In addition, the elastic and inelastic scattering spectra are sensitive to the target spot size and position. Analysis of a number of scattered electron spectra has shown that the full-width-at-half-maximum of the electron peaks agrees with the value calculated on the basis of incident energy spread and detector energy width. No off-energy electrons were detected when slits S1 were closed to a separation

of 0.03 inches.

The observed overall stability of the analysis system plus spectrometer for measurement periods of 12 hours and greater corresponds to an energy shift of < 30 keV in a scattered electron peak.

4.7.7 Elastic and inelastic spectra obtained with the system

We give in this section two examples of the results obtained using the electron scattering facility. The first (Fig. 4.7.2)

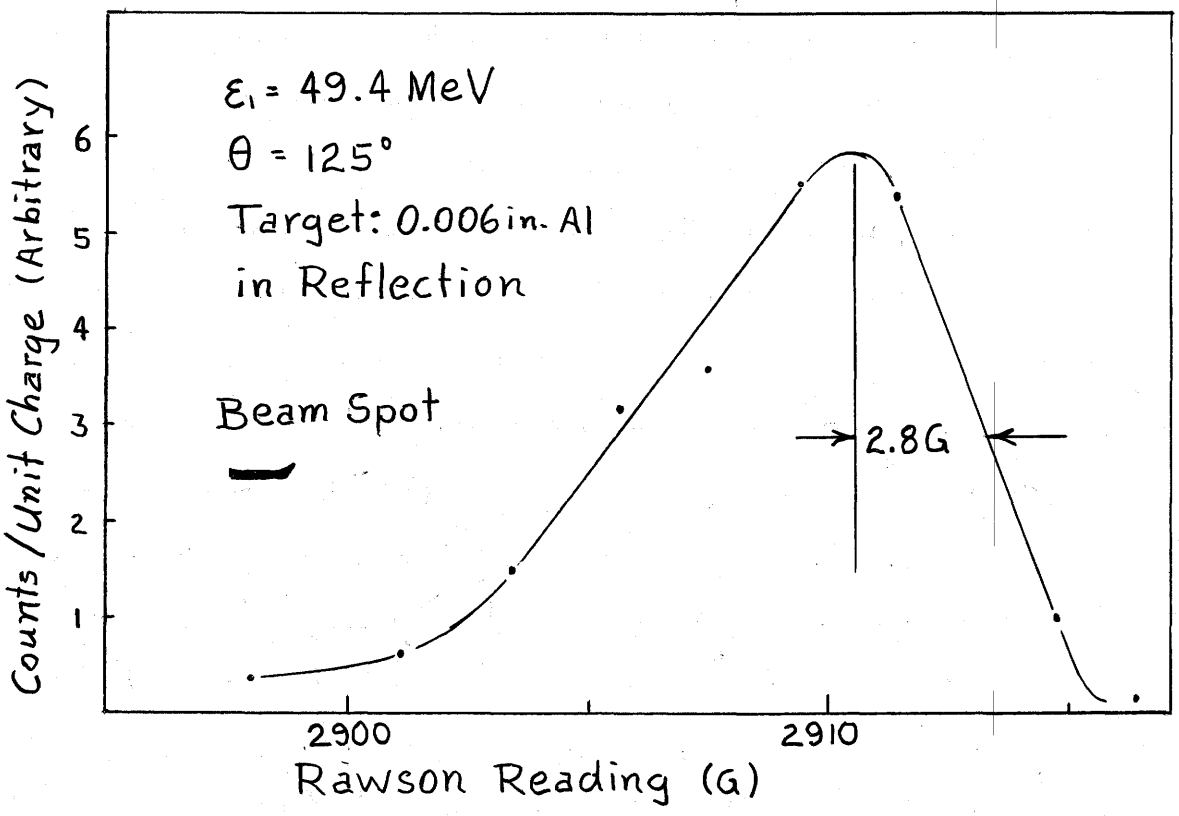

Fig. 4.7.2 Elastic peak obtained using a 2mm wide Ne 102 detector. Full size beam spot on the target is also shown.

shows the distribution of electrons elastically scattered through 125^{o} by a 0.006-inch-thick aluminum target. The data were obtained with the 0.14% detector (MK1) placed on the focal plane of the spectrometer and an incident energy of 49 MeV with a width of 0.1%. The full width-at-half-maximum of the scattered electron distribution determined from the high energy side of the peak is 0.19%, in excellent agreement with a calculated value of 0.18%.

The second example is an uncorrected spectrum of electrons elastically and inelastically scattered from ^{12}C. This spectrum (Fig. 4.7.3) is intended merely to illustrate the capability of the electron scattering facility when used to measure properties of excited levels of target nuclei. The full-width-at-half-maximum of the elastic peak in this case results from the use of the MK2 detector and a 0.2% energy spread in the incident beam. The abcissa is proportional to the energy of the electron detected by the spectrometer and the ordinate to the number of electrons per unit incident beam charge in the energy width defined by the detectors*. The error bars are those derived from counting statistics only.

It is of interest to note that excitation of the monopole level in ^{12}C by the Coulomb term in Eq. (2.4.1) is seen in this spectrum.

4.8 Experimental procedures

With the spectrometer set at the desired angle, an electron

*For a fixed detector size, the energy width is a function of spectrometer field, hence a dispersion correction must be applied to the data to obtain a number proportional to $(d^2\sigma/d\Omega d\epsilon_F)$.

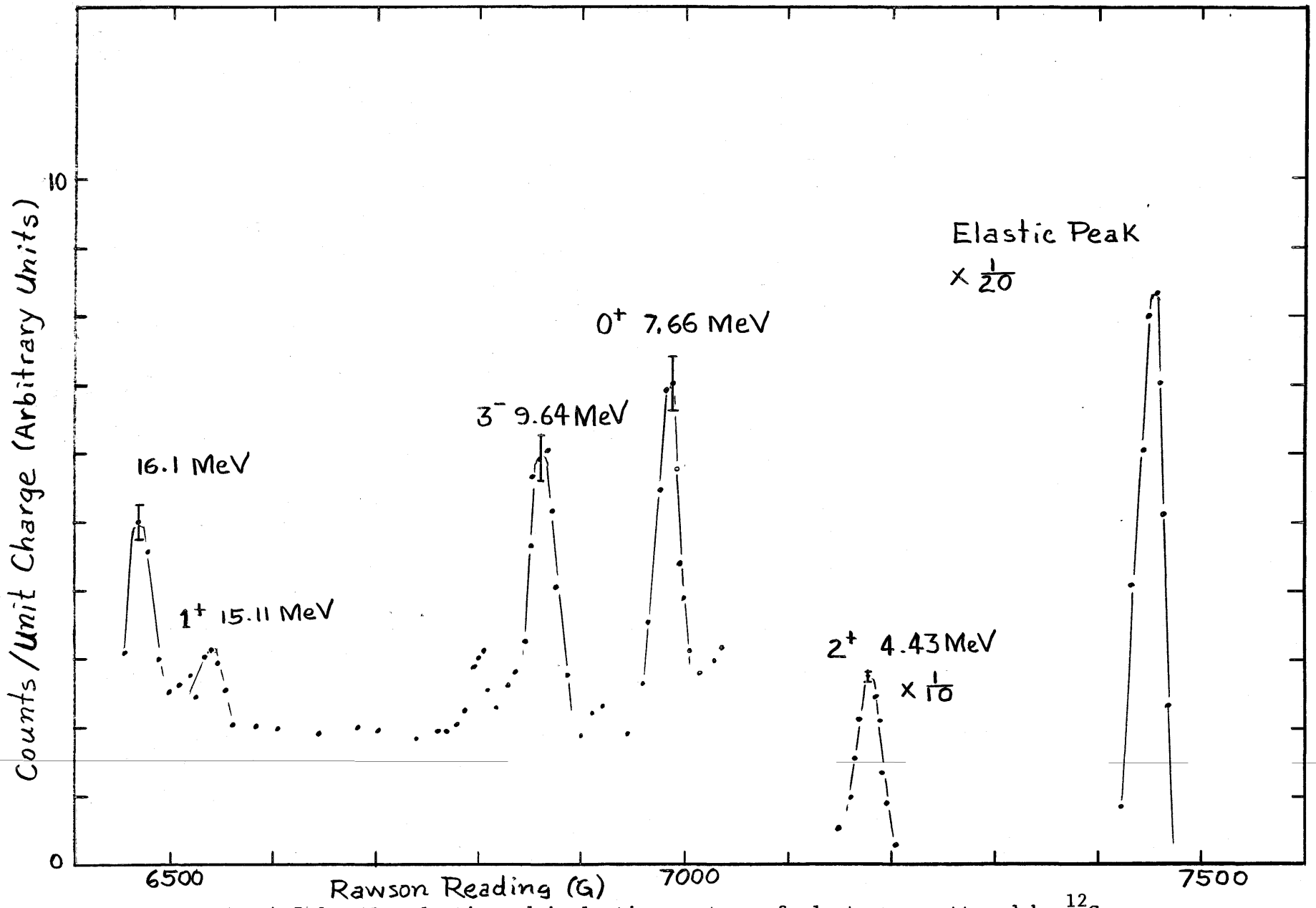

Fig. 4.7.3 The elastic and inelastic spectrum of electrons scattered by ^{12}C.

beam of the required energy and energy spread is centred on the scatter target. The shape of the beam is adjusted to a small spot with quadrupole pair Q3. The spectrometer is set to accept elastically scattered electrons and the peak count rate is maximized using the horizontal steering coil beyond magnet M2. This procedure places the beam centroid within 1 mm of the geometric centre of the scatter chamber. At this point the beam handling system requires no further adjustment and a scattered electron spectrum may be obtained by varying only the field within the spectrometer. At each field setting, a count is made of the number of electrons per unit charge scattered into the spectrometer detector. Each count is started by opening the gate circuits in the fast discriminators and starting the SEM current integrator simultaneously. It is stopped by using a pre-set charge circuit in the Elcor integrator to shut the fast gates and stop integration. The following data are then recorded:

i) The number of true and delayed coincidences,

ii) Their difference which represents "true" counts,

iii) The average Rawson reading of the spectrometer field, and

iv) The charge measured by the current integrator.

Each uncorrected spectrum consists of a plot of the true count per unit charge vs. Rawson reading for a range of spectrometer fields.

At 4 hour intervals during the measurement, the Faraday cup is placed in the beam behind the scatter chamber and an SEM efficiency measurement is made. The scatter target is removed from the beam to eliminate beam enlargement caused by multiple scattering.

While measuring a spectrum, several points are repeated on the elastic peak. Deviations beyond those expected from counting statistics or from a shift in energy > 30 keV were not observed during the experimental runs summarized in Chapter 6.

At some time when the target is out of the primary beam, a background measurement is made for a range of spectrometer settings.

4.9 Carbon target specifications

The carbon target used for the measurements described in this thesis is 1 inch high, 2 3/8 inch wide and 0.023 inches thick. It was fabricated from reactor graphite with a density of 2.27. The concentration of the dominant impurity in reactor graphite, calcium, is specified to be < 500 ppm.

To simplify the calculations in Chapter 5, the thickness may be expressed as 130 mg/cm^2.

CHAPTER 5

TECHNIQUES USED TO OBTAIN MATRIX ELEMENTS FROM ELECTRON SPECTRA

5.1 Introduction

The experimental spectra obtained following the procedures outlined in Chapter 4 require several corrections before a comparison with nuclear theory can be made. The cross sections derived in Chapter 2 were based on a single photon exchange between the scattered electron current and the nuclear transition current, whereas experimental results are complicated by other nuclear interactions. Two processes which alter the spectrum of scattered electrons have been ignored in the analysis outlined in Chapter 2. First, the electron may emit real photons or emit and re-absorb virtual photons either before or after nuclear scattering. Second, because the target is not infinitely thin, the electron loses energy both before and after nuclear scattering by ionizing the target matter.

To obtain single-photon-exchange cross sections, the peak areas in the measured electron spectra are corrected for these effects separately.

We give in this chapter the formulae which will be used in Chapter 6 for making these corrections to the ^{12}C data. It is not the intention of the author to treat them in detail since exhaustive treatments have been in the literature for many years and Bishop (1965) summarizes these in a review paper.

No justification is given for our specific choice of correction formulae. Others would also be satisfactory because, as will be

shown in Section 5.3, the analysis which is used to obtain the inelastic form factor requires a knowledge of only the ratio of corrections to elastic and inelastic peaks. This ratio is insensitive to the choice of corrections.

5.2 Energy loss and radiative corrections

5.2.1 Ionization

The ionization correction accounts for a loss of electrons from a peak in the spectrum as a result of energy degradation of electrons by ionization of the target matter. For the case of a target in transmission where the electron continues through the target after scattering, it is based entirely on the calculated energy straggling of the electrons, whereas for a target in reflection where the electron leaves the target from the side it entered, the correction is a complicated function of the energy loss as well as straggling. Both straggling and energy loss are shown to be essentially independent of electron energy, hence the ratio of elastic to inelastic ionization correction is extremely close to unity.

An expression for the average energy loss of a relativistic electron of energy $\mathcal{E}$ MeV in passing through a solid can be written in the form Beer (undated)

$$\frac{\partial \mathcal{E}}{\partial z} = 0.1537\left(\frac{Z}{A}\right)\left(\ln \mathcal{E} + \ln\left(\frac{A}{Z\rho}\right) + 20.67\right), \qquad (5.2.1)$$

where $\frac{\partial \mathcal{E}}{\partial z}$ is the energy loss in MeV-cm^2/g,

Z and A are the atomic number and mass number of the solid,

and ρ is the density in g/cm^3.

The ^{12}C spectra to be analyzed in Chapter 6 all were obtained with the target placed in reflection. For this case electrons travel through target thicknesses varying from 0 to a maximum of twice the effective target thickness t'*. If we consider a graphite target of effective thickness 130 mg/cm^2, this corresponds to a maximum energy loss in the scattered electrons of ~400 keV.

In addition to suffering energy loss in passing through matter, the energy distribution of outgoing electrons is broadened by straggling. If the electrons pass through a constant thickness of matter (such is the case for a target in the transmission mode), then a fraction of the electrons is degraded below an energy which is $\Delta\varepsilon$ MeV below the peak. A correction for this loss of electrons from a peak is given by Isabelle and Bishop (1963) in the form

$$K_I = 1 + \frac{0.178 Z t'_z}{A \Delta\varepsilon} , \qquad (5.2.2)$$

with t'_z the effective target thickness in g/cm^2. This correction amounts to 1 - 2% for a graphite target with $\Delta\varepsilon$ = 1 MeV and t'_z = 130 mg/cm^2.

5.2.2 Radiation corrections

Corrections for processes which involve the emission of photons have been calculated in first Born approximation by Schwinger (1949), Tsai (1961), Meister and Yennie (1963), Schiff

*t' = t/Sin θ/2 for a target in reflection

(1952) and others. Their results are expressed as correction factors to the experimentally measured cross section. Two types of correction are made, one, termed the bremsstrahlung correction, for the case in which the initial electron energy is degraded by an amount greater than the experimental energy resolution; the other, termed the radiative correction, for smaller degradations.

Two radiative corrections have been used in the determination of the ^{12}C inelastic form factor. The Schwinger correction was used for the elastic peak. It may be written in the form

$$K_S^{El} = \exp(+\delta_r), \tag{5.2.3}$$

with $$\delta_r = \frac{4\pi}{\alpha}\left\{K\left[\ln\left(\frac{2\varepsilon_1}{mc^2}\sin\theta/2\right) - \frac{1}{2}\right] + \frac{17}{32}\right\},$$

where $K = \ln\left(\frac{\varepsilon_1}{\Delta\varepsilon}\right) - \frac{13}{12}$.

An equivalent expression for the case of inelastic electron scattering was used to correct the inelastic peaks. This correction, derived by Meister and Griffy (1964), may be written

$$K_S^{In} = (1 - \delta_{r'}), \tag{5.2.4}$$

with $$\delta_{r'} = \frac{\alpha}{\pi}\left\{\ln\left(\frac{\Delta\varepsilon^2}{\varepsilon_1\varepsilon_2}\right)\left[\ln\left(\frac{\vec{q}^2}{0.511}\right) - 1\right] - \frac{1}{2}\ln^2\left(\frac{\varepsilon_1}{\varepsilon_2}\right) + \frac{13}{6}\ln\left(\frac{\vec{q}^2}{0.511}\right) - \frac{28}{9}\right\}.$$

The bremsstrahlung correction for elastic scattering as quoted by Hofstadter (1956) is

$$K_B^{El} = \exp(-\delta_B), \tag{5.2.5}$$

where $$\delta_B = \frac{t_z}{\ln 2}\ln\left(\frac{\Delta\varepsilon}{\varepsilon}\right).$$

For the inelastic bremsstrahlung correction, Isabelle and Bishop (1963) give an additional factor in Eq. (5.2.5). This factor, when evaluated for a 130 mg/cm^2 ^{12}C target, differs from unity by $\sim$0.02%. Thus the ratio of elastic to inelastic bremsstrahlung correction is $\sim$1, and the correction may be ignored in evaluating Eq. (5.3.8).

Electrons which have emitted hard photons either before or after a nuclear scattering form a continuous radiation tail below the scattered electron peak with the $1/\varepsilon$ shape characteristic of radiative processes. Even at large energy separation ε from the elastic peak, the tail can be a significant background for inelastic measurements hence its magnitude must be predicted.

An analytic form for the radiation tail of the elastic peak expressed as a function of the elastic form factor has been given by Bernheim (1965). This equation has been incorporated into a computer program which is used to calculate the magnitude of the radiation tail at 20 MeV excitation energy based on the measured cross section of the ^{12}C elastic peak.

5.2.3 Summary

To summarize, we present the approximations or formulae which we have used in Chapter 6 to evaluate the ratio of the elastic to the inelastic correction factor.

i) $K_I^{El} = K_I^{In}$.

ii) $K_B^{El} = K_B^{In}$.

iii) K_S^{El} given by Eq. (5.2.3).

iv) K_S^{In} given by Eq. (5.2.5).

5.3 Definition of the cross section and form factor

The electron scattering cross section differential in energy and solid angle may be obtained from the experimentally measured electron spectra. We first relate the number of electrons n striking the detector to the number n_o incident on the target.

$$n = n_o \left(\frac{d^2\sigma}{d\Omega\, d\mathcal{E}_F} \right) \Delta\mathcal{E}_F \, \Delta\Omega \, P, \qquad (5.3.1)$$

where $\Delta\mathcal{E}_F$ is the energy width of the detector,

$\Delta\Omega$ is the solid angle of acceptance of the spectrometer,

and P is the number of scattering centres per unit area within the target.

This cross section is a function both of incident energy and of scattering angle. However, both these quantities are constants for each spectrum.

To obtain an expression in terms of experimentally measured parameters, we write

$$n_o = \frac{Q}{|e|}, \qquad (5.3.2)$$

where Q is the total incident beam charge,

and e is the charge on the electron.

Also,

$$P = \frac{N_o \rho}{A} t', \qquad (5.3.3)$$

where N_o is Avogadro's number,

ρ is the target density,

A is the atomic weight of the target nuclei,

and t' is the effective target thickness.

These equations, when combined, yield an expression for the differential cross section which contains several constant factors for the case of a fixed target angle and target thickness. The constants are written in round brackets in the equation

$$\frac{d^2\sigma}{d\Omega d\varepsilon_F} = \frac{n}{Q\Delta\varepsilon_F}\left(\frac{|e|\,A}{N_0 \rho t' \Delta\Omega}\right). \qquad (5.3.4)$$

Peaks will appear in a plot of $d^2\sigma/d\Omega d\varepsilon_F$ against ε_F. The experimental differential cross section $(d\sigma/d\Omega)_{Exp}$ for a particular nuclear level is the area under the appropriate peak in the spectrum. The integration to obtain this area extends to a lower cut-off energy $\Delta\varepsilon$, and the corrections discussed in Section 5.2 are used to obtain the cross section corresponding to that derived in Chapter 2. Explicitly,

$$\frac{d\sigma}{d\Omega} = \left(\frac{d\sigma}{d\Omega}\right)_{Exp} K_S \cdot K_B \cdot K_I, \qquad (5.3.5)$$

where K_S, K_B and K_I are the correction factors given in Section 5.2.

Measured cross sections frequently are expressed as form factors or equivalently as matrix elements. We have chosen to measure the ratio of the inelastic to the elastic cross section, then to deduce the inelastic form factor from the elastic one. This technique may be used whenever the elastic form factor is well known. It has several advantages. In particular, the measurement does not require an accurate knowledge of target thickness and density, or spectrometer solid angle.

With superscripts "In" for inelastic and "El" for elastic, we may write Eq. (2.4.5) and Eq. (2.5.2) as functions of the measured differential cross section.

$$\left(\frac{d\sigma}{d\Omega}\right)^{In}_{Exp} = \frac{1}{(K_S K_B K_I)^{In}} \cdot \frac{Z^2 \sigma_M}{1+\frac{2\varepsilon_1}{M_N}\sin^2\theta/2}\left(\frac{1}{2}+\tan^2\theta/2\right) F_T^2(q_{In}), \qquad (5.3.6)$$

$$\left(\frac{d\sigma}{d\Omega}\right)^{El}_{Exp} = \frac{1}{(K_S K_B K_I)^{El}} \cdot \frac{Z^2 \sigma_M}{1+\frac{2\varepsilon_1}{M_N}\sin^2\theta/2}\left(\frac{1}{2}+\tan^2\theta/2\right) F_{El}^2(q_{El}). \qquad (5.3.7)$$

Combining these equations we obtain

$$F_T^2(q_{In}) = \frac{\left(\frac{d\sigma}{d\Omega}\right)^{In}_{Exp}(K_S K_B K_I)^{In}\ F_{El}^2(q_{El})}{\left(\frac{d\sigma}{d\Omega}\right)^{El}_{Exp}(K_S K_B K_I)^{El}\left(\frac{1}{2}+\tan^2\theta/2\right)}. \qquad (5.3.8)$$

The relationship between this form factor and the transverse matrix element is clear from Eq. (2.4.5).

These results are used in the next chapter to analyze the three experimental ^{12}C spectra.

CHAPTER 6

EXPERIMENTAL RESULTS

6.1 Calculation of the transverse matrix element and level width

6.1.1 Experimental carbon spectra

In this chapter we obtain a value for the transverse matrix element of the 19.4 MeV level in ^{12}C from each of three experimental electron spectra. These spectra, shown in Figs. 6.1.1, 6.1.2 and 6.1.3 were obtained at $\theta = 155^{o}$ with incident energies of 63.7, 94.9 and 127.2 MeV respectively. The elastic peak, the 19 MeV region, and the average target-out background are shown on the figures. The error bars shown are those derived from counting statistics.

As a first step in the analysis of these spectra the background was subtracted. This procedure is straightforward since the background was found to be constant over a wide range of spectrometer field values for a fixed incident energy. However the background count per unit charge was found to increase as the incident energy is raised.

The next step was to reduce the resulting data to quantities proportional to $d^2\sigma/d\Omega d\varepsilon_F$. This was done by modifying Eq. (5.3.4) to take account of efficiencies both in the detection of scattered electrons and in the measurement of incident beam charge. For this modification, we set

$$\frac{n}{Q} = G\left(\frac{n'}{Q'}\right), \tag{6.1.1}$$

where G is an efficiency factor, and n′ and Q′ are the measured "true" count and incident charge respectively. Thus we obtain

$$\left(\frac{d^2\sigma}{d\Omega d\varepsilon_F}\right) = \left(\frac{|e|}{P\Delta\Omega}\right)\frac{G n'}{\Delta\varepsilon_F Q'}. \tag{6.1.2}$$

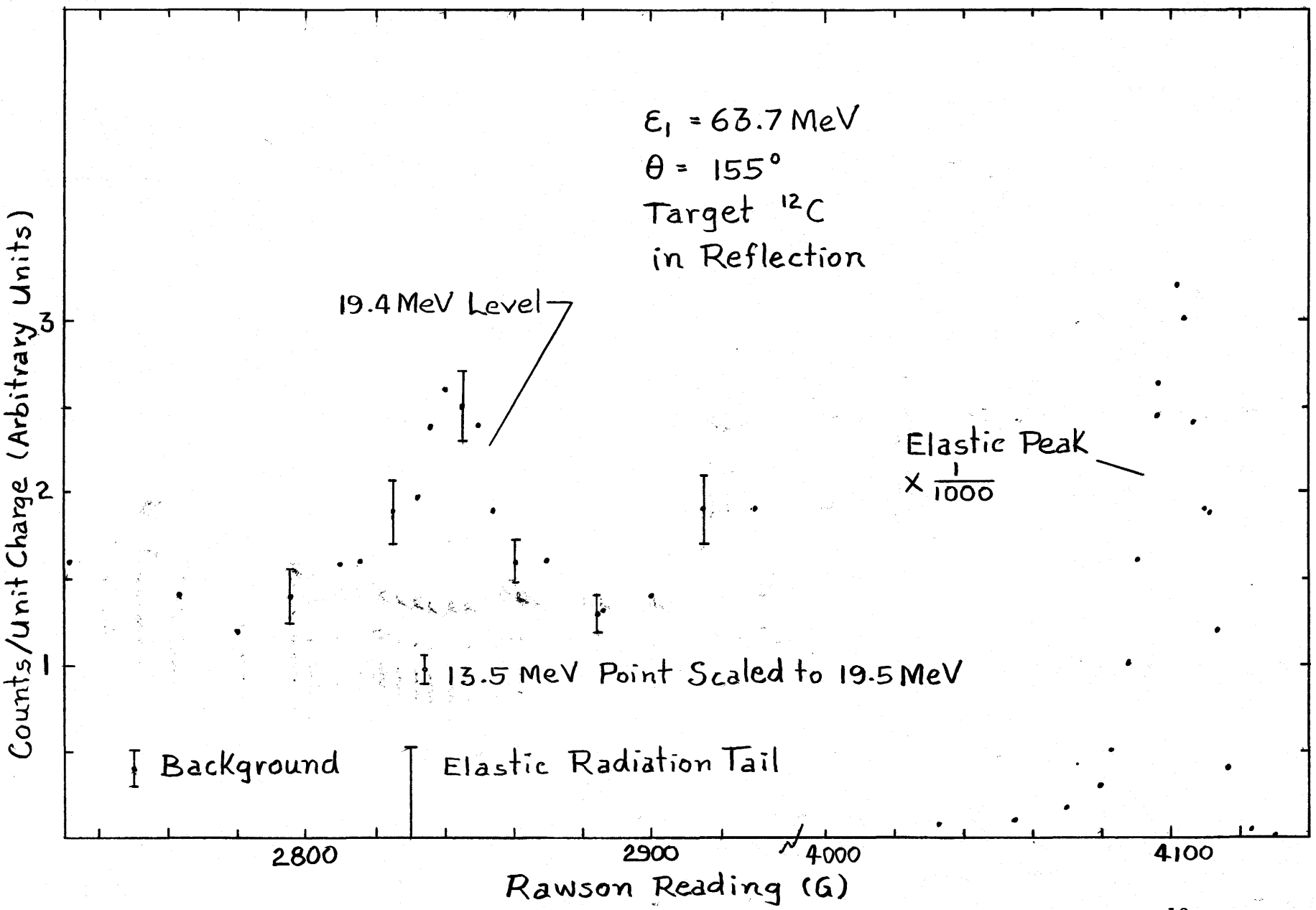

Fig. 6.1.1 Spectrum of 63.7 MeV electrons scattered elastically and inelastically from ^{12}C.

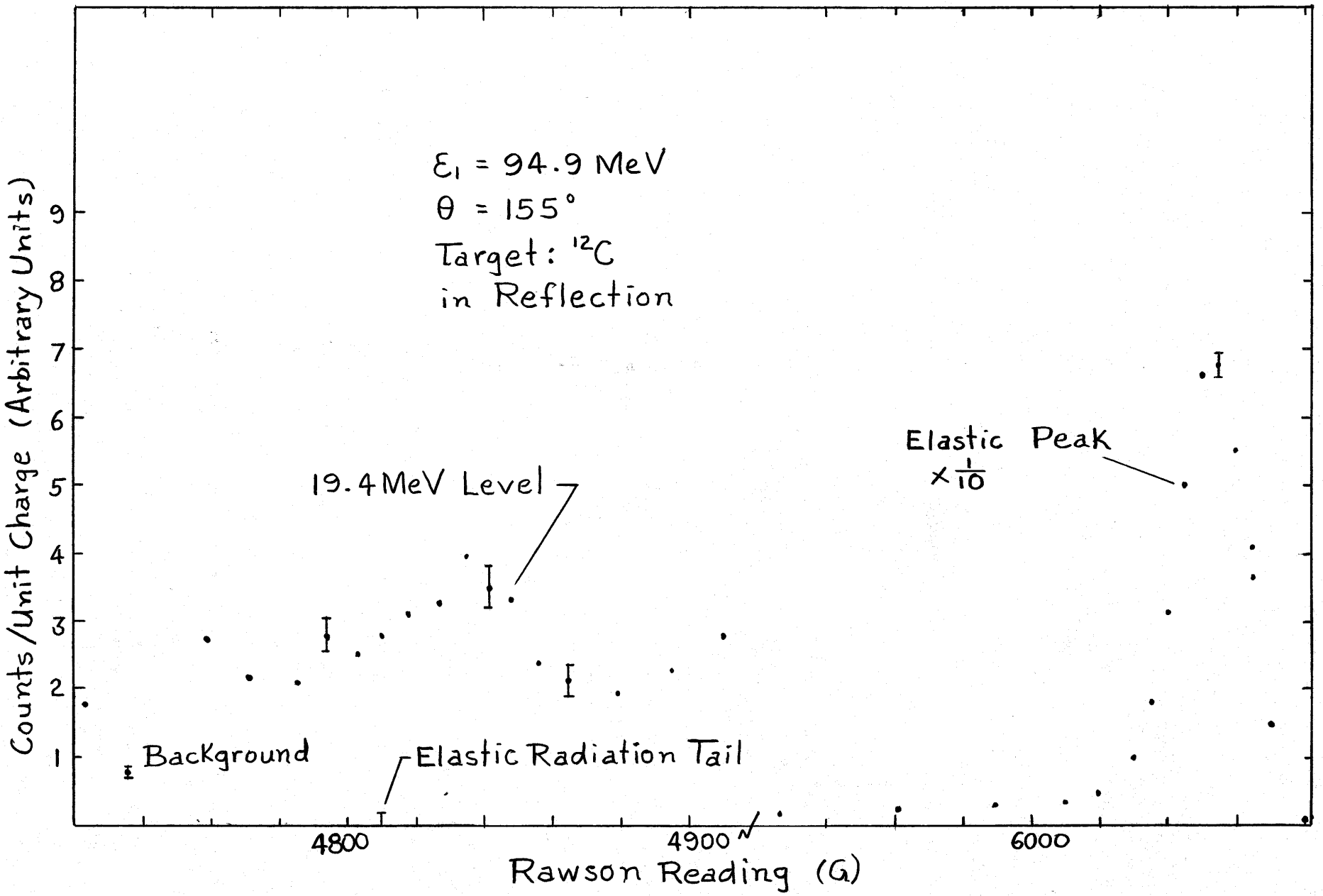

Fig. 6.1.2 Spectrum of 94.9 MeV electrons scattered elastically and inelastically from ^{12}C.

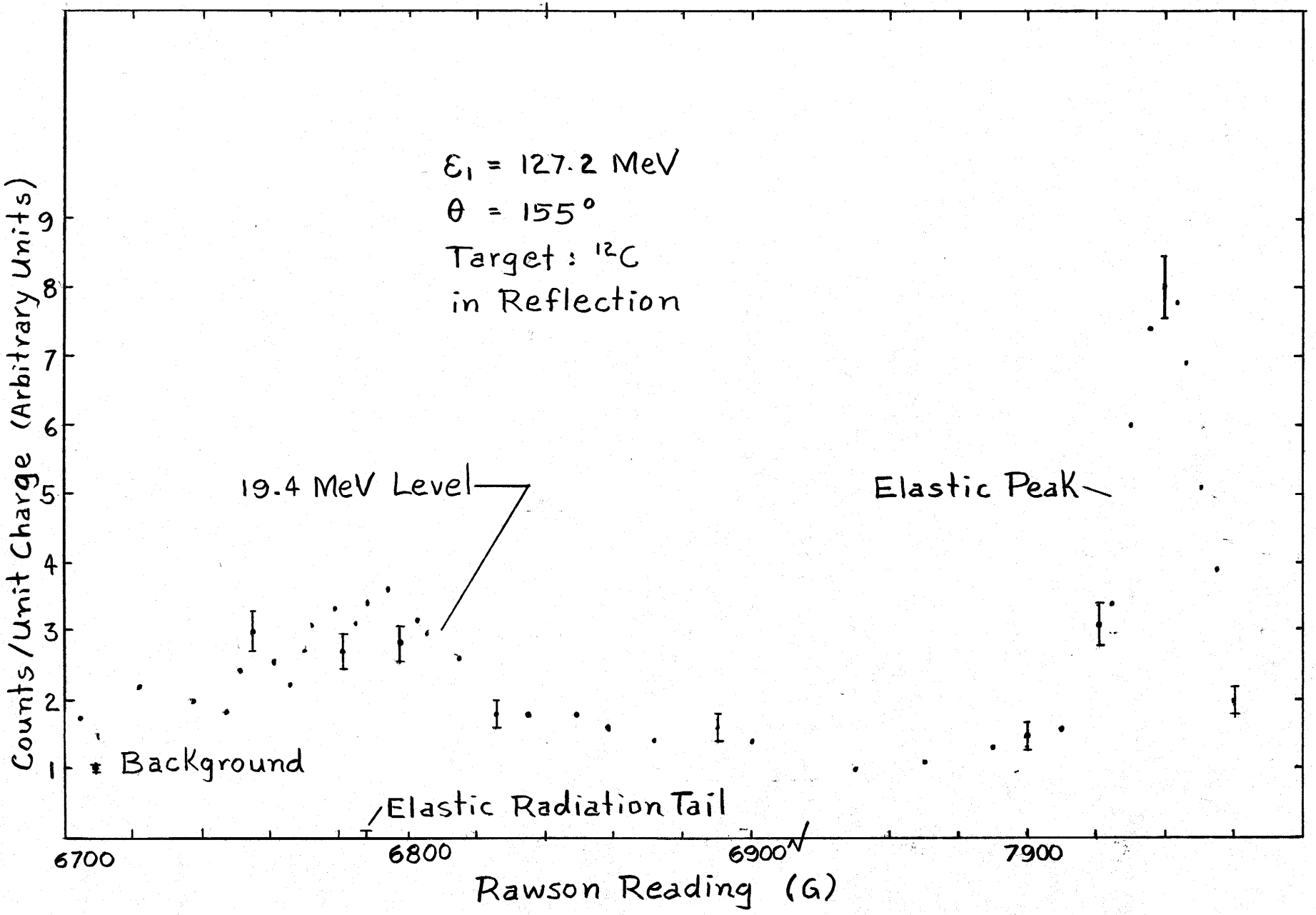

Fig. 6.1.3 Spectrum of 127.2 MeV electrons scattered elastically and inelastically from ^{12}C.

As before, the quantity in the round brackets is a function of scattering angle and target thickness for a fixed spectrometer angle and solid angle. The factor G is a constant for each measured spectrum, thus only $\Delta\varepsilon_F$ and the count per unit charge (n'/Q') are variables over a given spectrum.

Because it is the ratio of areas under the elastic and the corresponding inelastic peak which appears in the expression for $F_T^2(q_{in})$, we have chosen to reduce both elastic and inelastic data simply by dividing the reduced count rate (n'/Q') by $\Delta\varepsilon_F$. For this reduction, the energy width of the detector $\Delta\varepsilon_F$ is

$$\Delta\varepsilon_F = \eta\,\varepsilon_F, \tag{6.1.3}$$

where $\eta = 0.0028$ for the width of the present detector.

To avoid confusion in the analysis to follow, we define

$$\left(\frac{d^2\sigma}{d\Omega d\varepsilon_F}\right)' = \frac{n'}{Q'\Delta\varepsilon_F}, \tag{6.1.4}$$

and

$$\left(\frac{d\sigma}{d\Omega}\right)' = \int\left(\frac{d^2\sigma}{d\Omega d\varepsilon_F}\right)' d\varepsilon. \tag{6.1.5}$$

These expressions are, of course, proportional to their unprimed counterparts. Similar primed expressions are used for other quantities which were discussed in Chapter 5.

Eq. (6.1.4) has been incorporated into a computer program which was used in the analysis of the ^{12}C spectra. This comprehensive data reduction program is discussed further in Section 6.1.2.

Since different procedures have been followed to obtain $(d\sigma/d\Omega)'_{Exp}$ for the elastic and for the inelastic peak at 19.4 MeV in the spectra, we consider them separately for the sake of clarity.

However, in Section 6.1.4 elastic and inelastic results from the same spectrum will be substituted in Eq. (5.3.8) to obtain $F_T^2(q_{1m})$.

6.1.2 Elastic scattering

A data reduction program was written to perform the following steps in the analysis of the elastic peak. First, to obtain $(d\sigma/d\Omega)'^{El}_{Exp}$ the elastic region of the spectrum was integrated numerically over an energy region which spans the elastic peak and extends an interval $\Delta\varepsilon$ below it. Using this value of $\Delta\varepsilon$, the elastic radiative correction was calculated. Finally, to aid in the analysis of the inelastic region of the spectrum, the magnitude of the elastic radiation tail was calculated over the inelastic region of interest.

The results of these calculations for the three ^{12}C spectra are given in Table 6.1.1.

Table 6.1.1

Elastic peak parameters

ε_1 (MeV)	$\Delta\varepsilon$ (MeV)	$\left(\frac{d\sigma}{d\Omega}\right)'^{El}_{Exp}$	K_S
63.7	1.59	62.3	1.140
94.9	2.00	11.0	1.164
127.2	1.45	0.887	1.221

6.1.3 Inelastic scattering

The calculated elastic radiation tail was subtracted from all inelastic data to obtain the spectra shown in Figs. 6.1.4, 6.1.5 and 6.1.6. Because the radiation tail forms a

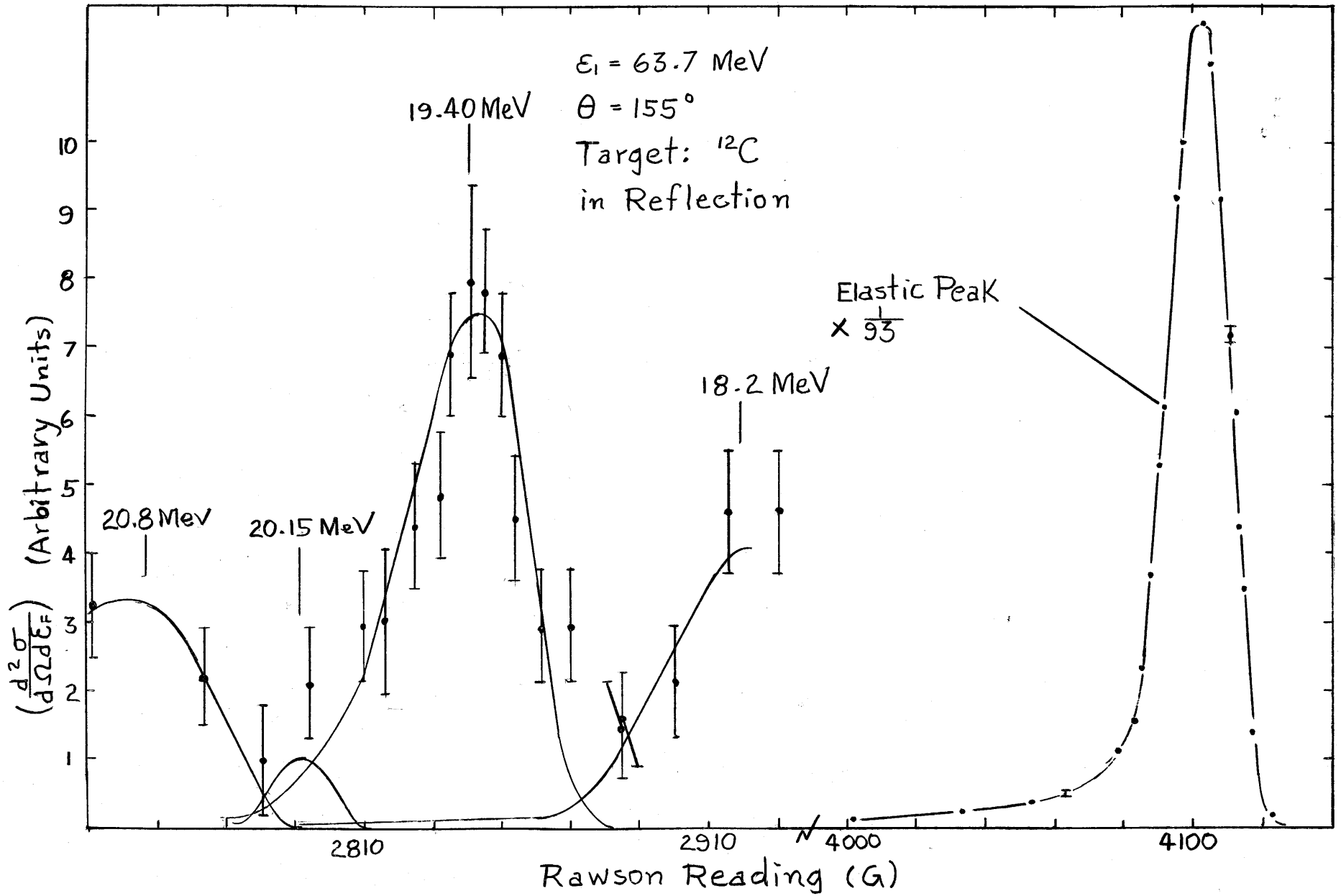

Fig. 6.1.4 Corrected spectrum of 63.7 MeV electrons scattered elastically and inelastically from ^{12}C.

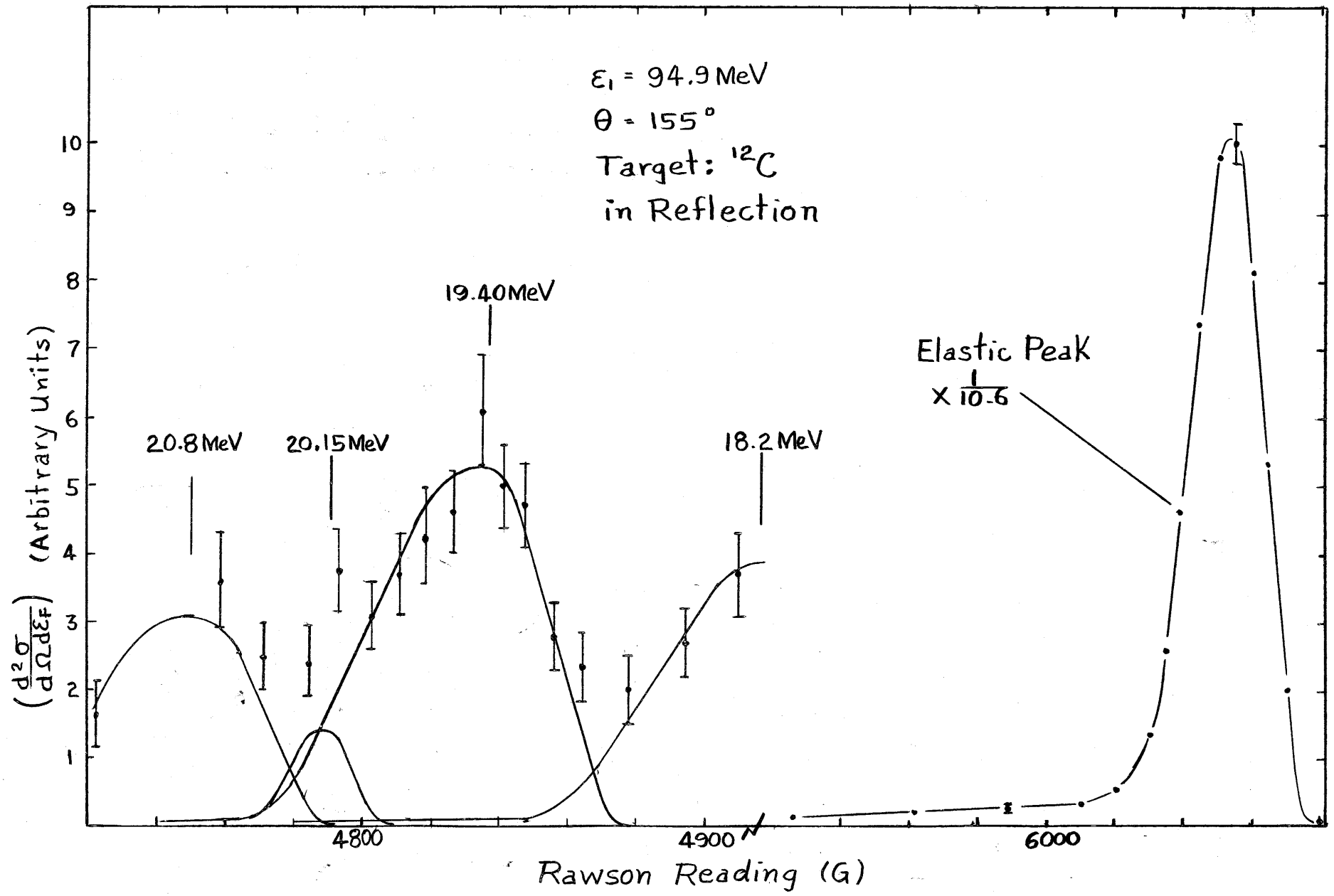

Fig. 6.1.5 Corrected spectrum of 94.9 MeV electrons scattered elastically and inelastically from ^{12}C.

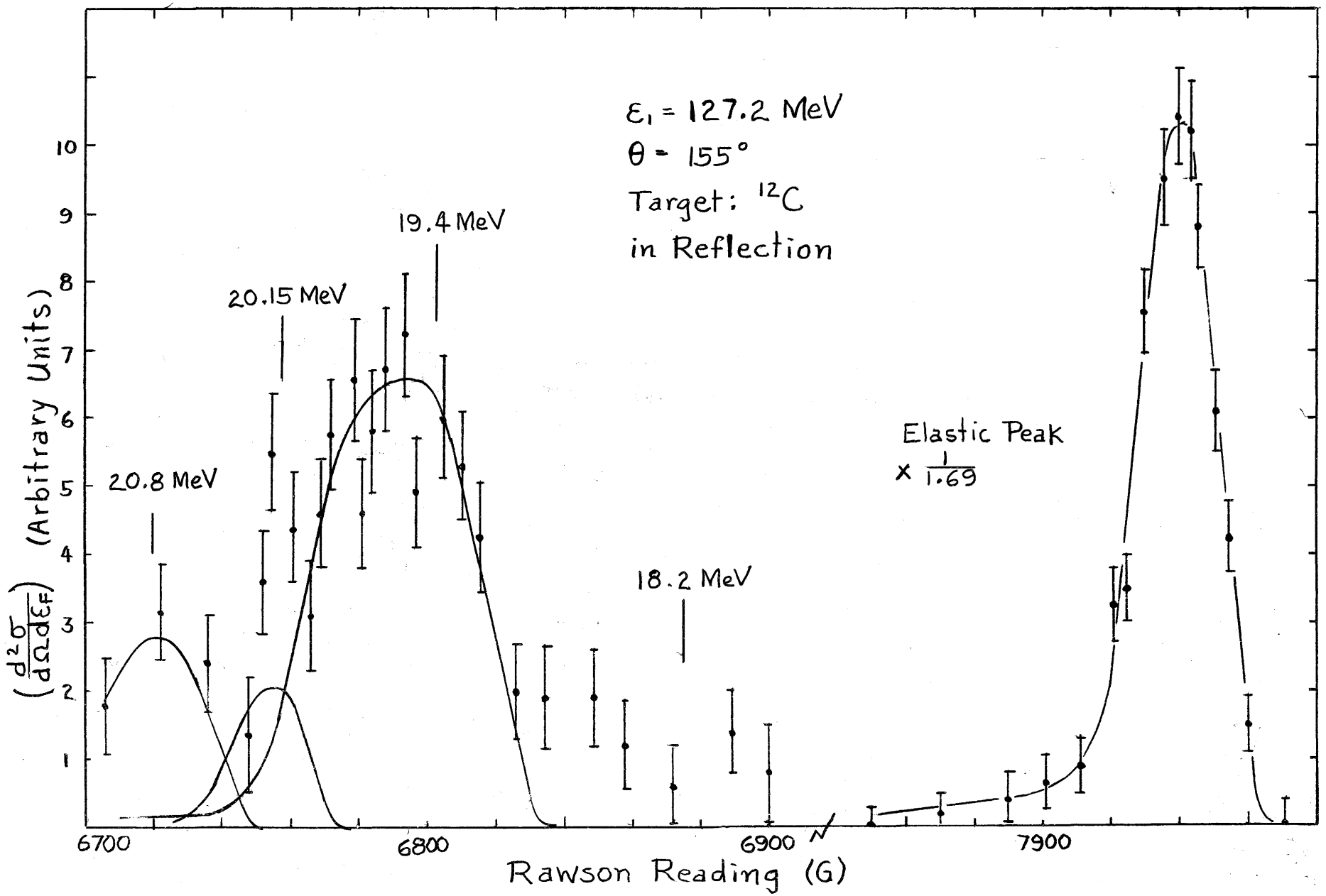

Fig. 6.1.6 Corrected spectrum of 127.2 MeV electrons scattered elastically and inelastically from ^{12}C.

significant part of the background for the 64 MeV spectrum, an experimental measurement of its magnitude was made. We show in Fig. 6.1.1 a data point obtained from a measurement at 13.5 MeV excitation energy in ^{12}C where the effects of inelastic excitation are expected to be small. It was scaled to the 19.5 MeV region of the spectrum by taking account of a decrease in the elastic tail and a change in the detector width $\Delta\varepsilon_F$. Satisfactory agreement was found between this point and the sum of target-out background and calculated radiation tail at 19.5 MeV.

The ordinates of the smooth curves shown in each of Figs. 6.1.4, 6.1.5 and 6.1.6 sum to a fit of the experimental data. The peak excitation energies of 18.2 MeV, 19.4 MeV, 20.15 MeV and 20.8 MeV were chosen on the basis of six ^{12}C experimental spectra, three of which were obtained with a different detector (MK2).

To obtain values for $(d\sigma/d\Omega)'^{lm}_{Exp}$, the curves which peak at 19.4 MeV were integrated out to a low energy cut-off $\Delta\varepsilon$. This cut-off was chosen equal to that for the corresponding elastic peak.

The values for $(d\sigma/d\Omega)'^{lm}_{Exp}$ and other parameters used for the analysis of the 19.4 MeV level are given in Table 6.1.2.

Table 6.1.2

19.4 MeV level parameters

ε_1 (MeV)	$\Delta\varepsilon$ (MeV)	q_{lm} (MeV/c)	K_S for 19.5 MeV excitation	$\left(\frac{d\sigma}{d\Omega}\right)'^{lm}_{Exp}$
63.6	1.59	104.5	1.135	0.786
94.9	2.00	164.7	1.160	1.135
127.2	1.45	226.4	1.217	0.625

6.1.4 The transverse matrix element

The results obtained in Section 6.1.2 and 6.1.3, when substituted into Eq. (5.2.8), yield experimental values for $F_T^2(q_{In})$. However, in this analysis we use previously measured values of $F_{El}^2(q_{El})$ to eliminate several experimental uncertainties. The elastic form factor of ^{12}C has been measured by several research groups. Ehrenberg et al (1959), Meyer-Berkhout et al (1959), Repellin (1963), and most recently Crannel (1966) observed that all of the ^{12}C elastic electron scattering data could be fitted by the harmonic well model of the nuclear ground state. In this model the charge distribution is given by Eq. (2.5.5) and the charge form factor by Eq. (2.5.6). Experimentally it has been found for ^{12}C that with α = 4/3, the "best-fit" value for "a" ranges from 2.41 F to 2.47 F. The data at momentum transfers of less than 1.5 F^{-1} are in good agreement with values calculated using a = 2.42 F.

The harmonic well form factor with the values a = 2.42 and α = 4/3 has been used in the analysis which results in the measured values given in Table 6.1.3.

Table 6.1.3

The experimentally measured transverse form factor and matrix element for the level at 19.4 MeV in ^{12}C

q_{In} MeV/c	$F_T^2(q_{In})$	$\lvert\langle 2^- \lVert \hat{T}_2^{mag}(q) \rVert 0^+\rangle\rvert^2$
104.5	0.275×10^{-3}	0.789×10^{-3}
164.7	0.832×10^{-3}	2.38×10^{-3}
226.4	1.18×10^{-3}	3.38×10^{-3}

The experimental values for the transverse matrix elements in Table 6.1.3 are to be compared in Section 6.3 with a theoretical calculation which predicts a 2^- level in ^{12}C. Hence we have written the caption $|\langle 2^- \| \hat{T}_2^{mag}(q) \| 0^+ \rangle|^2$.

6.1.5 Level width

An estimate of the width of the level at 19.4 MeV has been made by unfolding the experimental resolution from the measured width assuming that both are Gaussian distributions in energy. The calculated full-width-at-half-maximum of the level is given in Table 6.1.4.

Table 6.1.4

Deduced width of the 19.4 MeV level in ^{12}C

ε_1 (MeV)	Nuclear level width (keV)
63.7	500
94.9	800
127.2	800

6.2 Discussion of errors

In this section we estimate the experimental errors in the determination of the inelastic excitation energy, the elastic and inelastic momentum transfer, and the matrix elements.

The error in determining the absolute value of ε the excitation energy of a nuclear level depends on the spectrometer

calibration as well as the measured values of B_{El} and B_{In}. The calibration of the spectrometer which was used to measure $\mathcal{E}$ and the symbols and formulae used are given in Appendix B. The standard deviation of the measured values of V, a factor in the equation for $\mathcal{E}$, is 0.25%. Both B_{El} and B_{In} may be determined to an accuracy of $\pm$2 Gauss which, for 20 MeV excitation energy, corresponds to an uncertainty of $\pm$0.25%. Hence the overall uncertainty in determining an excitation energy of 20 MeV is $\pm$0.5%.

The errors in determining q_{El} and q_{In} arise from uncertainties in the incident energy $\mathcal{E}_i$, the scattering angle θ and, for the inelastic momentum transfer, the excitation energy $\mathcal{E}$. For the experiments performed at 155°, the momentum transfer is almost independent of θ. We estimate that $\mathcal{E}_i$ is known to within $\pm$1%, hence the uncertainty in q_{El} is $\pm$1% and q_{In} is $\pm$1.5%.

There are several uncertainties contributing to the error in the form factor. We consider uncertainties in

i) The measured ^{12}C elastic form factor,

ii) the number of scattered electrons per unit charge (n'/Q'),

iii) the background,

iv) the calculated radiation tail underlying the inelastic peak,

v) the ratio of the inelastic to the elastic radiative correction,

vi) the scattering angle θ, and

vii) the technique of treating close-spaced inelastic levels.

The ^{12}C cross section data were measured with respect to the experimental proton cross section. Crannell (1966) estimates that the proton data are accurate to within 5%. Experimental errors in the ^{12}C comparison measurements are estimated to result in an overall uncertainty in the ^{12}C cross section of $\pm$5%.

The uncertainty in the number of counts n' is statistical. If a Poisson distribution is assumed, the error in a count is $\sqrt{n'}$. In determining the count per unit incident charge there is an additional small uncertainty due to the SEM efficiency which we estimate to be $\pm$0.5%. These uncertainties apply both to spectrum and to background data.

There is an estimated uncertainty of $\pm$10% in the calculated value of the radiation tail underlying the 19.4 MeV peak. For the spectra taken at ϵ_1 = 95 MeV and 127 MeV this results in a small uncertainty in the measured inelastic peak area. However, for the spectrum taken at ϵ_1 = 64 MeV the elastic radiation tail is a significant fraction of the height of the 19.4 MeV peak. The resultant uncertainty in the area of the peak was reduced to $\pm$7% by measuring the elastic radiation tail to a precision of $\pm$6% in the 13.5 MeV region.

The relative uncertainty in the ratio of radiative corrections applied to elastic and inelastic peaks is estimated to be less than 1%.

An uncertainty in the scattering angle θ results from error in the position of the beam spot. For the measurements discussed in this thesis the electron beam has been positioned horizontally

on the scatter target to within $\pm$1 mm. It can be shown that this gives rise to an uncertainty of $\pm$1.7% in the term $(1/2 + \tan^2(\theta/2))$ (c.f. Eq. (5.3.8)).

It is difficult to estimate the uncertainty in a measured inelastic form factor due to the treatment of nearby inelastic levels. The radiation tails from levels at lower excitation energy such as the one at 18 MeV in ^{12}C contribute to the spectrum at 19.4 MeV. We have estimated the magnitude of the inelastic radiation tail from the 18 MeV level. It is found to contribute 5.5% to the 19.4 MeV peak area at $\mathcal{E}_i$ = 95 MeV, 4.5% at $\mathcal{E}_i$ = 64 MeV and an insignificant amount at $\mathcal{E}_i$ = 127 MeV. The estimated error in the magnitude of the 18 MeV tail contributes less than $\pm$0.5% uncertainty to the peak area.

No estimate has been made of the uncertainty in the strength of the peak found at 20.15 MeV. However, the area ascribed to it varies from 4% of the 19.4 MeV peak area at $\mathcal{E}_i$ = 64 MeV through 10% at 95 MeV to 13% at 127 MeV.

The error bars shown on the data in Fig. 6.3.1 represent a combination of these sources.

6.3 Summary of experimental results

The present measured values of the transverse matrix element are shown on Fig. 6.3.1. The results of previous measurements made at a scattering angle of both 180° and 152° are also shown. The present results are seen to be in good agreement with the measurements of Goldemberg and Barber (1964) and are not

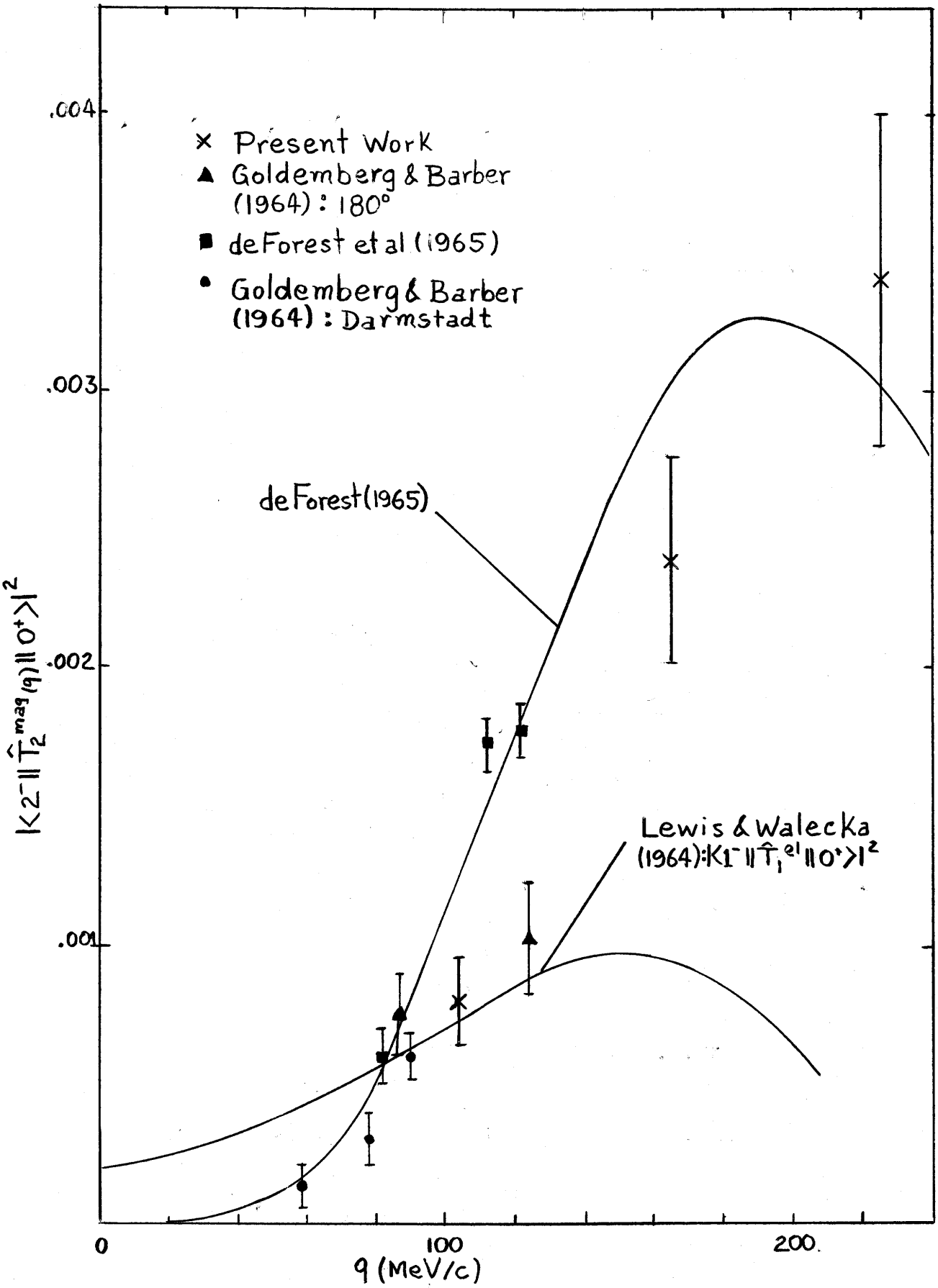

Fig. 6.3.1 The transverse matrix element for the 19.4 MeV level in ^{12}C.

in serious disagreement with the measurements of deForest et al (1965).

We compare our data with the particle-hole calculation of deForest (1965) which predicts a strong 2^- level in ^{12}C at ~21 MeV. This calculation, discussed in Chapter 1 and Chapter 3, is seen to predict both the magnitude of the matrix element and its variation with q. For comparison, we show the result of an equivalent particle-hole calculation by Lewis and Walecka (1964) which predicts a 1^- state in ^{12}C at 19.57 MeV. It is clear that our high-momentum-transfer data favour the 2^- calculation. In particular, the minimum which appears in the 1^- calculation at $q \simeq 200$ MeV is not seen. In fact, when the present results are combined with those of Crannel et al (1966) they show a maximum in an assumed transverse matrix element at ~250 MeV/c.

The q-dependence of the squared matrix element at low momentum transfer is precisely that predicted by the long-wave-length limit of the operator $\hat{T}_2^{mag}(q)$. Hence the assignment J = 2 is consistent with the data.

The matrix elements calculated on the basis of Überall's spin-isospin collective mode are not shown in the figure since, as previously stated in Chapter 3, they represent the total 2^- strength. However, satisfactory agreement both in q-dependence and in strength may be achieved if we compare experimental data for the level at 19.4 MeV with 70% of the theoretical values.

A level width of 500 $\pm$ 100 keV is quoted by Goldemberg and Barber (1964) based on a measurement made at 152^o with 56 MeV

electrons. The present low-momentum-transfer measurement of the level width is in agreement. In the measurements by deForest et al (1965) the experimental resolution was $\sim$1.4 MeV thus no value for the level width was given.

Goldemberg and Barber (1964) also quote a measured excitation energy of 19.46 $\pm$ 0.05 MeV, in excellent agreement with our result.

CHAPTER 7

CONCLUSIONS

The present experimental results extend into a region of momentum transfer not previously investigated and are in agreement with others in the region of overlap. They also extrapolate consistently with the higher-momentum-transfer data of Crannell et al to complete an overall picture of the q-dependence of the transverse matrix element for the 19.4 MeV level in ^{12}C. Although it is not possible to make a model-independent spin-parity assignment for this level on the basis of the measured q-dependence of the matrix element, satisfactory agreement with the 2^- calculation of deForest et al (1965) over the region of higher momentum transfer clearly favours the assignment 2^- rather than 1^- as reported by Goldemberg and Barber (1964) and Crannell et al (1966). The results show no experimental evidence for the diffraction minimum at $q \simeq 200$ MeV/c predicted on the basis of the 1^- assignment. Instead, the matrix element is found to be a maximum at $q \simeq 250$ MeV/c in approximate agreement with the particle-hole calculation which predicts a maximum at q = 190 MeV/c. The spin assignment J = 2 is consistent with the experimentally observed growth of the squared matrix element as q^4 in the region of low momentum transfer.

The reasonably close agreement between present data and the results obtained from the collective calculations of Überall (1966) lend credence to the rather satisfying (if oversimplified) picture of a spin-isospin resonance in nuclear matter which gives rise to a 2^- state.

The measured behaviour of the width of the 19.4 MeV level in ^{12}C does not preclude a doublet in this region. It would be worthwhile to make further extremely high resolution measurements between 19 and 20 MeV.

The agreement between present experimental results and nuclear model predictions for ^{12}C gives further impetus to extending the measurement to other nuclei. It is plausible to expect this 2^-, or magnetic quadrupole resonance to be a feature common to all light nuclei, as is the giant dipole resonance. Dipole resonance investigations have for many years been carried out using photons. More recently electron scattering techniques have been employed. Electrons have all the merits of a monochromatic photon beam with the additional advantage that the momentum transfer can be varied. Thus electron scattering provides a powerful method for studying the quadrupole resonance in other nuclei.

APPENDIX A

BREMSSTRAHLUNG PRODUCTION IN THE TRANSPORT SYSTEM

The electron beam in passing through matter produces bremsstrahlung. If this radiation is produced in the beam path from magnet M2 to the scatter target, it contaminates the electron beam incident on the target. We show in this appendix that the bremsstrahlung produced by electrons traversing the residual air in this 45 feet of beam tube is orders of magnitude less than the production within a typical electron scatter target.

To do this, we consider the well-known formula (Bethe and Ashkin, 1953) relating the radiative energy loss of an electron to the radiation length X_0 of the matter traversed,

$$-\left(\frac{\partial \mathcal{E}_0}{\partial x}\right)_{Rad} \simeq \frac{\mathcal{E}_0}{X_0} \quad , \tag{A.1}$$

where $(\partial \mathcal{E}_0/\partial x)_{Rad}$ is the energy loss per unit thickness due to radiation, and $\mathcal{E}_0$ is the incident electron energy.

Bremsstrahlung production per unit thickness is proportional to this energy loss. Hence for a fixed incident energy total production in a thickness h is proportional to h/X_0, where h/X_0 is the thickness in radiation lengths. The residual air in the 45 foot beam tube is $\sim 10^{-9}$ radiation lengths thick at a pressure of 10^{-5} Torr. In comparison, the targets used for electron scattering are $\sim 10^{-3}$ radiation lengths thick. Thus the bremsstrahlung production within the beam tube is many orders of magnitude less than production within the target.

APPENDIX B

DIFFERENTIAL ENERGY CALIBRATION OF THE ELECTRON SPECTROMETER

The spectrometer is used to measure differential energies within electron spectra. To calibrate the unit, the electron scattering techniques outlined in this thesis were employed to measure the magnetic field differential between the elastic peak and the 15.11 MeV level in ^{12}C.

However, before discussing the calibration procedure in detail we review the equation which relates electron energy to path radius for relativistic motion in a magnetic field. We consider the specific case of electrons with kinetic energy $\mathcal{E}'$ traversing the spectrometer along the optical axis of radius R. The central field B which sustains this motion is

$$B = \frac{[\mathcal{E}'(\mathcal{E}'+2mc^2)]^{1/2}}{0.03\,R}, \tag{B.1}$$

with R in meters, $\mathcal{E}'$ in MeV and B in Gauss. With the approximation $mc^2 \ll \mathcal{E}'$ and substitution of the measured spectrometer radius, we obtain the following expression for the central energy

$$\mathcal{E}' = 0.01219\ B = V_o B. \tag{B.2}$$

More generally, we write

$$\mathcal{E}' = V\ B, \tag{B.3}$$

where V is a constant to be determined by experiment.

We now combine this general result with Eq. (2.3.6) which is an expression for the excitation energy $\mathcal{E}$ in terms of quantities measured with the spectrometer. We write $\mathcal{E}_{El} = V\ B_{El}$ and $\mathcal{E}_{In} = V\ B_{In}$ in the equation to obtain

$$\mathcal{E} = \frac{V(B_{El}-B_{In})\left(1+\frac{2VB_{El}}{M_N}\sin^2\theta/2\right)}{1+\frac{V(B_{El}-B_{In})}{2M_N}}, \tag{B.4}$$

where B_{El} is the central magnetic field at the elastic peak, and B_{In} in the central magnetic field at an inelastic peak of excitation energy $\mathcal{E}$.

This equation may be solved for V if approximations are used in the small terms which contain M_N. We get

$$V = \mathcal{E}\left\{\frac{1}{B_{El}-B_{In}} + \frac{V_o}{2M_N}\right\}\left\{\frac{1}{1+\frac{2\mathcal{E}_1}{M_N}\sin^2\theta/2}\right\}. \qquad (B.5)$$

Measured spectrometer field settings corresponding to elastic scattering and inelastic scattering from the 15.11 $\pm$ 0.01 MeV level in ^{12}C were substituted in Eq. (B.5). Five experimental spectra taken at several incident energies $\mathcal{E}_1$ and scattering angles θ were analyzed to obtain values for V. All were within 0.3% of the average, $\bar{V}$ = 0.01214. This uncertainty in V is accounted for entirely by an estimated experimental error in determining the difference (B_{El} - B_{In}) in the peak field values.

As a check on this calibration, we compare the incident electron energy $\mathcal{E}_1$ measured using the spectrometer to that determined by the beam analyzing system. The spectrometer data were analyzed by setting $\bar{V}\, B_{El} = \mathcal{E}_{El}$ in Eq. (2.3.5) which relates incident energy to $\mathcal{E}_{El}$. Four values for $\mathcal{E}_1$ obtained from spectrometer measurements were 1.0 $\pm$ 0.4 percent lower than the corresponding beam analyzing system energies.

Since the analyzing magnets were calibrated using a nuclear-magnetic-resonance probe to measure the field, they are used to determine incident energy to an estimated uncertainty of $\pm$1%.

APPENDIX C

RECENT MEASUREMENT ON THE 19.5 MeV LEVEL IN ^{12}C AT HIGH MOMENTUM TRANSFER

After the preparation of the main text of the thesis was completed the author received a preprint by Crannell et al (1966). These authors have measured the matrix element for a level found at 19.5 MeV excitation energy in ^{12}C. However, the scattering angle was 40^{o} and the momentum transfer was varied from 267 MeV/c to 643 MeV/c. Their measured values of the longitudinal matrix element are shown in Fig. (C.1). Two sets of data points are plotted, one marked "experimental I", the other "experimental II". These result from two alternate ways of analyzing the data. In Method I merely the total height of the 19.5 MeV peak was used. This height was compared with the height of either the elastic peak or the peak due to excitation of the 4.43 MeV 2^{+} level, depending upon which of the comparison peaks was larger. To determine the differential cross section for scattering from the level, it was assumed that the ratio of the peak heights was the same as the ratio of the cross sections. This is a good assumption, provided that the physical widths of the peaks are less than the widths given by experimental resolution. Their measurements were made with a high incident energy, hence $\Delta\mathcal{E}_F$ is ~ 2 MeV. Thus the assumption is reasonable. However, this treatment does not take into account the contributions from other inelastic processes. In Method II, an estimated contribution from the break-up continuum was subtracted from the height of the 19.5 MeV peak before the comparison of peak heights was made. The

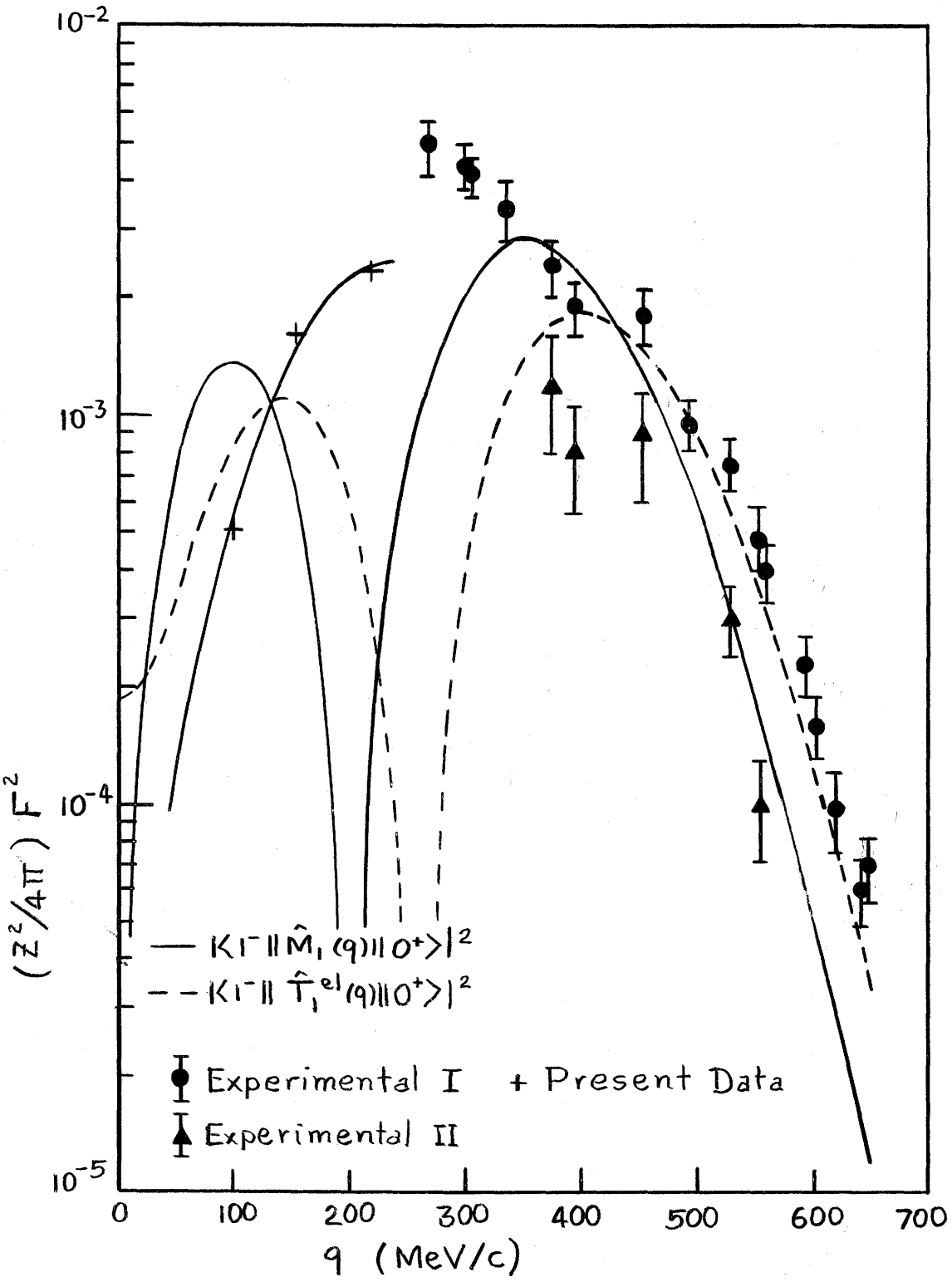

Fig. C.1 The data of Crannell et al (1966).

authors assume the truth to lie somewhere between the results obtained using these two methods of analysis.

The results are compared with matrix elements calculated by Lewis and Walecka (1964). These calculations predict a T = 1, J = 1^- state in ^{12}C at 19.6 MeV. Agreement at high momentum transfers between theory and experiment is satisfactory. However, in the region of momentum transfers below 400 MeV/c the experimental points show no evidence for the diffraction minimum predicted by theory. It is important to notice that these results were plotted on a logarithmic scale whereas the scale on Fig. 6.3.1 is linear.

We consider the cross section at 40^o to result from the transverse terms in Eq. (2.4.2) and Eq. (2.4.3) since only transverse terms contribute if the level is magnetic. From Eq. (2.4.2) or Eq. (2.4.3) it is clear that if transverse terms contribute, we should compare the quantity $\left[(Z^2/4)\ (1/2 + \tan^2\ (40^o/2))\ F_T^2\right]$ with the data of Crannell et al (1966). This comparison is made in Fig. C.1. The experimental values for F_T^2 were those in Table 6.1.3. The comparison values are smaller than Experimental I values as expected, but satisfactory agreement is achieved if we compare with values lying between those obtained by Method I and Method II.

The combined measurements of Crannell et al (1966) and those reported in this thesis show no evidence for a diffraction minimum over a range of momentum transfers up to 600 MeV/c.

BIBLIOGRAPHY

Alder, K. et al 1956. Rev. Mod. Phys. 28, 432.

Beer, G.A. (undated). Saskatchewan Accelerator Laboratory Internal Report No. 11.

Beer, G.A. 1964a. Saskatchewan Accelerator Laboratory Notebook No. 10.

Beer, G.A. 1964b. Saskatchewan Accelerator Laboratory Design Note No. 1.

Beer, G.A. 1964c. Saskatchewan Accelerator Laboratory Design Note No. 6.

Beer, G.A. 1965a. Saskatchewan Accelerator Laboratory Notebook No. 30.

Beer, G.A. 1965b. Saskatchewan Accelerator Laboratory Design Note No. 2.

Beer, G.A. 1965c. Saskatchewan Accelerator Laboratory Design Note No. 3.

Beer, G.A. 1965d. Saskatchewan Accelerator Laboratory Design Note No. 4.

Bernheim, M. and Bishop, G.R. 1963. Phys. Lett. 5, 294.

Bernheim, M. 1965. Thèse, Universite de Paris.

Bethe, H.A. and Ashkin, J. 1953 in Experimental Nuclear Physics, I, edited by E. Segre (John Wiley and Sons, Inc., New York).

Bishop, G.R. 1965 in Nuclear Structure and Electromagnetic Interactions, edited by N. MacDonald (Oliver and Boyd, Edinburgh).

Bishop, G.R. and Isabelle, D.B. 1962. Phys. Letts. 1, 324.

Brown, K.L. and Tautfest, G.W. 1956. Rev. Sci. Inst. 27, 696.

Brown, G.E. et al 1961. Nucl. Phys. 22, 1.

Carter, E.B. et al 1964. Phys. Rev. 133B, 1421.

Crannell, H. 1966. Phys. Rev. 148, 1107.

Crannell, H.L. and Griffy, T.A. 1964. Phys. Rev. 136, B1580.

Crannell, H. et al 1966. Stanford University Preprint.

deForest, T. 1965. Phys. Rev. 139, B1217.

deForest, T. et al 1965. Phys. Letts. 16, 311.

deForest, T. and Walecka, J.D. 1966. Advances in Physics 15, 1.

Dodge, W.R. and Barber, W.C. 1962. Phys. Rev. 127, 1746.

Edmonds, A.R. 1960. Angular Momentum in Quantum Mechanics (Princeton University Press, Princeton).

Ehrenberg, H.F. et al 1959. Phys. Rev. 113, 666.

Erikson, T. 1964. Nucl. Phys. 55, 497.

Gibson, W.A. 1964. Rev. Sci. Inst. 35, 1021.

Gillet. V. 1962. Thèse, Universite de Paris.

Gillet, V. and Vinh Mau, N. 1964. Nucl. Phys. 54, 321.

Goldhaber, M. and Teller, E. 1948. Phys. Rev. 74, 1046.

Goldemberg, J. et al 1963. Nucl. Phys. 43, 242.

Goldemberg, J. and Barber, W.C. 1964. Phys. Rev. 134, B963.

Herman, R. and Hofstadter, R. 1960. High-Energy Electron Scattering Tables (Stanford University Press, Stanford).

Hofstadter, R. 1956. Rev. Mod. Phys. 28, 214.

Hofstadter, R. 1957. Ann. Rev. Nucl. Sci. 7, 231.

Hutcheon, R.M. and Beer, G.A. 1965. Saskatchewan Accelerator Laboratory Design Note No. 5.

Hutcheon, D.A. and Ku, S.H. 1965. Saskatchewan Accelerator Laboratory Design Note No. 7.

Isabelle, D. and Bishop, G.R. 1963. Nucl. Phys. 45, 209.

Isabelle, D. 1962. L'Onde Electrique 421, 66.

Kantz, A. and Hofstadter, R. 1954. Phys. Rev. 89, 36.

Kretschko, J. et al 1962. Nucl. Inst. Meth. 16, 29.

Leiss, J.E. and Taylor, R.E. 1960. Karlsruhe Photonuclear Conference (unpublished).

Lewis Jr., F.H. and Walecka, J.D. 1964. Phys. Rev. 133, B849.

Lobb, D.E. 1966. Ph.D Thesis, University of Saskatchewan.

Meister, N. and Griffy, T.A. 1964. Phys. Rev. 133, B1032.

Meister, N. and Yennie, D.R. 1963. Phys. Rev. 130, 1210.

Meyer-Berkhout, U. 1959. Ann. Phys. 8, 119.

Penner, S. 1961. Rev. Sci. Inst. 32, 150.

Pohlit, W. (undated). Private communication.

Repellin, J.P. 1963. Orsay Report L.A.L. 1046.

Sanderson, E.A. 1961. Nucl. Phys. 26, 1420.

Schiff, L.I. 1952. Phys. Rev. 87, 750.

Schiff, L.I. 1954. Phys. Rev. 96, 765.

Schwinger, J. 1949. Phys. Rev. 76, 790.

Sykes, D.H. M.Sc. Thesis, University of Saskatchewan.

Talmi, I. 1952. Helv. Phys. Acta 25, 185.

Tsai, Y.S. 1961. Phys. Rev. 122, 1898.

Überall, H. 1966. Nuovo Cimento, 41, 1.

Vanpraet, G.J. and Barber, W.C. 1966. Nucl. Phys. 79, 550.

Vinh-Mau, N. and Brown, G.E. 1962. Nucl. Phys. 29, 89.

Willey, R.S. 1963. Nucl. Phys. 40, 529.